Interfacial Templating of Inorganic Nanostructures Using Rationally Designed Peptide Molecules

By

Lorraine Leon Gibbons

A Dissertation Submitted to the Graduate Faculty of Engineering in Partial Fulfillment of the Requirements for the Degree of Doctor of Philosophy
The City University of New York

2011

This manuscript has been read and accepted for the Graduate Faculty in Engineering in satisfaction of the dissertation requirement for the degree of Doctor of Philosophy.

_____	_____
Date	Prof. Raymond Tu Chair of Examining Committee
_____	_____
Date	Prof. Mumtaz Kassir Executive Officer
	Prof. Alexander Couzis _____
	Prof. Ilona Kretzschmar _____
	Prof. Charles Maldarelli _____
	Prof. Ronald Koder _____

Supervision Committee

THE CITY UNIVERSITY OF NEW YORK

Abstract

Interfacial Templating of Inorganic Nanostructures Using Rationally Designed Peptide Molecules

By

Lorraine Leon Gibbons

Advisor: Raymond Tu

In nature, biological molecules form interfaces that assemble patterns of chemical functionality with exceptional precision. The role of dynamics during the assembly of biological molecules appears to be important for mineralization processes. The work presented in this dissertation applies model sheet-forming peptides at interfaces to explore the dynamics of assembly in order to template mineral growth. The peptide molecules are rationally designed to have amphiphilic properties and a propensity for sheet-like secondary structure. These designed peptides are deposited at the air/water interface to explore the dynamics of their self-assembly and investigate their 2D order. To characterize the phase behavior, techniques such as Langmuir Blodgett and Brewster Angle Microscopy are used. In addition, we verify the hypothesized sheet-forming propensity using both Circular Dichroism and Attenuated Total Reflection Fourier Transform Infrared Spectroscopy, while the characterization of the inorganic phase is done using Transmission Electron Microscopy, Electron Diffraction, and Atomic Force Microscopy.

Thermodynamic analysis of structure formation with increasing pressure allows us to understand the nature of self-assembly with iterative changes in the peptide sequence. Additionally, we look at the dynamics of the self-assembled state, where the organic phase switches between short- and long-range order as a function of surface pressure. We use this model system to explore the influence of electrostatic interactions on self-assembly, and additionally, the influence of short- and long-range order on the nucleation and growth of inorganic material. This is in contrast to a system that starts with a well-ordered preformed template that defines the epitaxial growth of the mineral phase. Two versions of our model peptides are constructed by substituting histidine for glutamic acid in order to nucleate Au nanocrystals in both the short and long range ordered organic matrix, to show that the phase behavior of the peptide influences the crystallinity and shape of the templated nanocrystals.

Acknowledgements

First and foremost, I would like to thank my advisor, Prof. Raymond Tu, for his constant support and guidance through out the course of my PhD. His overall good nature and ability to provide guidance and simultaneously encourage independent thought, has made him an advisor and role model.

Secondly, I would like to thank my committee members Prof. Alexander Couzis, Prof. Ilona Kretzschmar, Prof. Charles Maldarelli , and Professor Ronald Koder for their support and feedback. I would especially like to thank Prof. Alexander Couzis for help troubleshooting equipment and encouraging me to take things apart and learn how they work. In addition, I would also like to personally thank Prof. Ilona Kretzschmar, for being constantly available to provide guidance in matters scientific or otherwise.

Additionally, I would like to thank our collaborators Prof. Hiroshi Matsui and Wei Su for some good discussions on the gold project.

A special thanks to my lab members: Dr. Vikas Jain, Joe Badami, and Sean O'Neill, and the CCNY friends I have picked up during the years: Dr. Kevin Song, Dr. Spyros Monastiriotis, Dr. Tieuvi Nguyen, Dr. Chi Lo, and Phil Matthews, for making lab time, lunch time and conference time, a wonderful experience.

Additionally, I would like to thank my boyfriend, Jeff Jackson, for always being there for me, and motivating me to do my best, through out the past five years.

Finally, I would like to dedicate my thesis work to my parents, Gabriel Leon and Lorraine Gibbons, who have done nothing but loved and supported me through out my entire life. Without their support, I know that none of this would be possible.

Contents

List of Figures

List of Tables

Chapter 1

Introduction

Natural systems provide elegant examples of how specifically designed molecules can be used to direct the growth of inorganic materials. There exists a wealth of inorganic materials that can be formed, and the intricate structures of these materials show us that nature controls these processes with exceptional precision. These natural systems have had more than 570 million years to perfect this process through evolution. In contrast, scientists and engineers are only in the beginning stages of being able to exert that level of control over structure. Although, much progress has been made in the last several decades, we are still inspired by these systems and attempts to mimic natural structures that use protein self-assembly to form macroscopic structures.

The ability of applying biological molecules to control the formation of inorganic material is a coveted technique for many reasons. Not only is the formation of large structures such as teeth and bone attractive for biomedical reasons, the formation of small nanostructured materials have many useful applications as diverse as electronic devices[1], photovoltaic devices[2], battery electrodes[3], biological imaging[4-8] and sensing[7-14], drug delivery[15-18], data storage platforms[19-21], and enzyme encapsulation[22, 23]. For these

reasons, the subject of this thesis is to study the ability of biomimetic molecules to template the growth of inorganic nanostructures.

In order to study the process by which biomimetic molecules template inorganic nanostructures, we have chosen peptides as the biomimetic molecules and gold as the inorganic material. Peptides were chosen because of the ability to design the molecules in a sequence specific manner, such that each amino acid incorporated in the sequence can provide unique functionality to the process. In addition, by manipulating peptide sequences the molecules can be designed to adapt to a particular secondary structure providing a specifically shaped interface for interactions with gold. Gold was chosen as the inorganic material because of the large amount of literature available and also because of its unique optical, electronic, magnetic, and catalytic properties exhibited at the nanometer length scale[5, 24-27], that could be used for the potential applications discussed earlier.

In order, to investigate the process by which peptides can template gold nanostructures, we have placed an emphasis on studying the interface between the peptides and the resultant gold. To do so, we have designed the peptide molecules in such a way that they exhibit an amphiphilic architecture, and we address these peptides confined to the air/water interface, where the gold precursor can be added to the water phase. In addition to being amphiphilic, the peptides have all been designed to form sheet structures at the air/water interface. A large effort of this work has been placed into carefully describing the behavior of the peptides at the air/water interface in order to properly ascertain the influence of the peptides on the nucleation and growth processes of gold. To do so, peptide molecules with varying degrees of electrostatic interactions, and

different charge distributions were designed in order to investigate how electrostatics can influence the self-assembly of the molecules at the air/water interface. The careful characterization of the interfacial assembly of our designed peptides led to the discovery that the peptides first self-assemble into structures exhibiting short-range order. Subsequently, the peptides transition into long-range order with increasing surface concentration. Therefore, by controlling the surface concentration we are able to explore several different inorganic nucleation conditions. The different nucleation conditions explored showcase different inorganic nanostructures.

In the following chapters, the details of our design strategy and systematic interface characterization will be discussed. Chapter 2 describes a background of biomimetic approaches to the synthesis and assembly of inorganic material and the underlying mechanisms at play. The chapter begins by describing some natural examples of the formation of inorganic materials, followed by a literature review of biomimetic molecules directing the growth of inorganic material, where the canonical scenario of a preassembled matrix is followed by organic and inorganic co-assembly. Chapter 3 describes the design of the peptides and the influence of electrostatic interactions on the self-assembly of the peptide molecules under two-dimensional confinement. This chapter thoroughly describes how the peptide sequences are characterized using interfacial techniques and how the peptides self-assemble into domains featuring different phase behavior depending on the surface concentration. Chapter 4 discusses the irreversibility of sheet-like structures and the extent to which network formation and macroscopic order leads to structural persistence. This chapter focuses on the hysteresis observed in the compression and expansion isotherms and how this hysteresis relates to

the network formation observed at the interface. Chapter 5 discusses the nucleation and growth of gold nanostructures using our designed peptides. This chapter discusses the ability of the peptide to both reduce and direct the growth of gold and the extent to which different nucleation conditions affect the growth of the gold phase. In Chapter 6, the dissertation is concluded and future directions that this work could take are discussed.

Chapter 2

Biomimetic approaches to the synthesis and assembly of inorganic material

In the past several decades, there has been a significant research effort devoted to nanostructured materials. Both organic and inorganic materials have been the subjects of this effort. Nanostructured organic materials have largely been used in medical applications such as gene delivery, tissue engineering, and drug delivery[28-30] because of the biocompatibility of the nanostructured proteins, peptides, and biopolymers. On the other hand, inorganic materials have attracted attention because of the unique optical, electronic, magnetic, and catalytic properties exhibited at this length scale[5, 24-27]. These unique properties allow these materials to be used in applications as diverse as electronic devices[1], photovoltaic devices[2], battery electrodes[3], biological imaging[4-8] and sensing[7-14], drug delivery[15-18], data storage platforms[19-21], and enzyme encapsulation[22, 23].

The methodologies used to fabricate inorganic materials in the nanometer size regime have been divided into top-down and bottom-up approaches. Top-down approaches are largely lithographic techniques in which material is prepatterned using a

mask to arrive at the final nanostructure. This approach is limited by the wavelength of lasers (photolithography) and high costs (electron beam lithography)[24]. In addition, the creation of features using top-down techniques is a layer-by-layer process[26]. In contrast, bottom-up techniques largely rely on self-assembly to form nanostructured material. Therefore the bulk of the effort lies in the design and synthesis of the molecule that then self-assembles into a supramolecular structure, not the patterning itself. Of course, to be able to successfully design a molecule that will self-assemble into a given structure a clear understanding of the forces driving this self-assembly must be acquired. Much progress has been made in understanding how electrostatic, hydrogen bonding, and hydrophobic forces work cooperatively by borrowing ideas from nature. Natural systems use self-assembly to organize phospholipids into bilayers and proteins into their quaternary structures[31]. However, to construct inorganic material adds a level of complexity because the organic scaffold not only needs to assemble correctly but also guide the growth of inorganic material. This can be done separately, where the organic matrix assembles first and then guides the nucleation and growth of inorganic material, or cooperatively, where the organic matrix and inorganic material co-assemble. In addition, the inorganic structures being formed can be discrete integrated objects or higher-order assemblies[32]. In each case, nature provides elegant examples of these processes.

2.1 Natural Composite Materials

2.1.1 Natural Nanostructured Composite Materials

One of the earliest examples of an organism guiding the synthesis and assembly of inorganic materials comes from fossils left behind by magnetic bacteria approximately 2 billion years ago. These bacteria are extremophiles and could have survived when earth's conditions were much more extreme in terms of temperature, pH, and gamma radiation, thus enabling their existence in the Precambrian era. Bacterial cells that have high surface to volume ratios rely on their cell surface for the immobilization of ions using secondary polymers and lipopolysaccarides. Regardless of the exact mechanism used to bind ions to the cell surface, the mineralization of the surface is achieved by manipulating energy barriers required for precipitation by changing pH values or redox potentials using their metabolism.[33]

Magnetic bacteria form magnetite crystals (Fe_3O_4), whose morphologies are dependent on the various unicellular species. These crystals are produced within the cell and not on the cell surface. They exist in three dominant morphologies: cuboctahedral, pseudo-hexagonal, and bullet shaped. However, regardless of their shape the crystals always have an fcc crystal structure. The bacteria produce crystals with narrow size distributions ranging from 40-120 nm depending on species. The crystals have high magnetic moments and uniform magnetic properties used to align the bacteria with the earth's magnetic field and swim along magnetic field lines.[33] The formation of magnetite in several species occurs in the magnetosome, which is a phospholipid vesicle that serves

as a type of nanoreactor created before the mineralization occurs[34]. In order to form magnetite, Fe^{III} is taken up by the bacteria and then reduced to Fe^{II} by a nitrite reductase found in the periplasm. Fe^{II} is then transported to the empty magnetosome vesicle using transport proteins (MamB and MamM) located in the magnetosome membrane. The magnetosome membrane has a different composition than the outer membrane and cytoplastic membrane, and presumably, the membrane itself is involved in the mineralization process since the majority of magnetite crystals are located near the membrane. The mineralization is guided using several proteins having acidic domains or amino acids presumably used for the immobilization of cations. An example of one of these proteins is Mms6, which has been shown to form uniform single magnetic particles in vitro. However, the exact mechanism of producing crystals of uniform size and the morphological control of the mineralization *in vivo* remains unknown[34]. The ability of this unicellular organism to synthesize and guide the growth of these highly uniform nanocrystals serves as an example of the formation of discrete integrated objects in natural systems.

Another biological example of the formation of discrete integrated objects occurs as a byproduct of a detoxification mechanism. Elevated levels of certain ions such as Cd^{2+} mimic essential metal ions such as Ca^{2+} leading to the malfunction of enzymes and at high levels denaturation of proteins and DNA leading to cell death. The detoxification of Cd^{2+} involves sequestration using small selective peptides followed by co-precipitation with inorganic sulfide to form non-toxic metal sulfide clusters. This biomineralization is documented in plants, yeasts, fungi, and bacteria and produces controlled nanoparticles. In plants and yeast, the process is intracellular and achieved via a metal-triggered

biosynthetic pathway. Sequestration is achieved using thiol-rich peptides that have an affinity for metal ions. These chelating peptides are called phytochelatins (PC_n) and have the general structure $(\gamma\text{-Glu-Cys})_n\text{-Gly}$ n=2-11 with a binding capacity for Cd^{2+} (K_{3Cd}) of approximately 10^9. PCs are also associated with homeostasis in the cell by mediating the nutrient levels. Studies preformed on tobacco leaves have identified the Cd^{2+}/PC_2 complex in vacuoles that confine the biomineralization process to a tight space resulting in restricting the size of the nanocrystal. Other studies on this complex using titration methods have identified that the formation of the complex is favorable in basic conditions, and Cd^{2+} is released under acidic conditions. Acid labile sulfide ions enter the vacuole and react with the released Cd^{2+} to form a PC capped nanocrystal. The capping of the nanocrystals is important for size control avoiding the rupture of the vacuole. Studies of the resulting nanocrystals indicate that the particles have a narrow size distribution and the particles are not prone to Ostwald ripening presumably because of the capping agent. This type of detoxification mechanisms has also been observed in bacteria and fungus[35].

The fungus *Verticillium* has been identified of forming noble metal nanoparticles. This eukaryotic organism produces 20nm gold nanoparticles, which are found on the surface of the fungus and within the cell. The highest concentration of particles is found in the cytoplasmic membrane and on the cell wall. Unlike bacteria that also produce gold nanoparticles, a large number of nanoparticles are observed for the fungus. Most of the nanoparticles are spherical with few particles having hexagonal or triangular shapes. As the Mms6 protein, the exact mechanism that Verticillium undergoes to reduce $AuCl_4^-$ is not understood. However, studies have shown that cell wall sugars are not involved in

the process, and the mechanism is not universal to all fungi. Similar to the detoxification mechanism of plants and yeast, the first step in the process is ion immobilization by enzymes or residues in the cell wall or possibly the cytoplasmic membrane. The second step is believed to be the reduction of the gold precursor with enzymes[36]. This fungus is just another example of organisms producing discrete composite nanostructures using their own proteins to guide the process that is carefully controlled by their metabolism.

2.1.2 Natural Higher-Order Composite Materials

Perhaps the more intricate examples that nature provides for guiding the formation of inorganic material is seen in higher order assemblies or hierarchical structures. A well-studied example of this process is the formation of coccoliths by unicellular algae. Coccoliths are produced by coccolithophores, a species that dates back to the Jurassic period and is covered in a shield of calcite known as a coccolithosphere. This coccolithosphere is made up of aggregated coccoliths. A distinction is made between holococcoliths that are formed as extracellular structures and have simple rhombohedral calcite morphology and heterococcoliths that are formed intracellularly and exhibit complex calcite morphology[33]. Heterococcoliths will be discussed here because the intricacies of morphological control provide a better example of the formation of higher order assemblies.

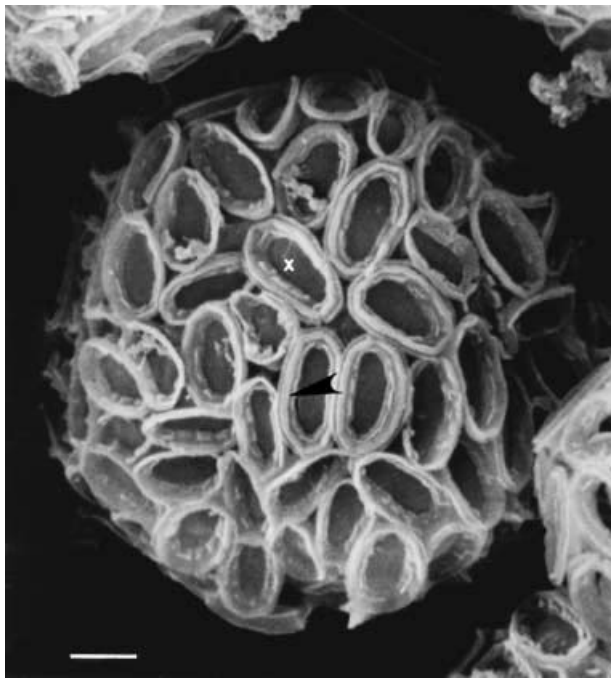

Figure 2.1: SEM image of a coccolithosphere from *Pleurochrysis Carterae*. The oval shaped features are each coccoliths[33].

Heterococcoliths, formed by *Pleurochrysis Carterae*, have an oval organic base plate that is subsequently covered in interlocking calcite crystals. The process begins with the formation of an organic vesicle that develops a complex form containing extensions that contain dense particles known as coccolithosomes. The coccolithosomes are a complex of acid polysaccharides (PS1 and PS2) and calcium ions that serve as calcium vectors during the biomineralization process. The calcite then nucleates around the base plate forming 24 small crystals of parallelepipeds that alternate between the vertical and radial direction relative to their c-axis. The maturing of the crystals begins with vertical units via their extension of the (104) surface eventually forming a plate-like surface of the outer tube and ending with parallel double discs. During the growth process, the coccolith vesicle expands to remain in contact with the developing coccolith leaving a dense organic coating around and in between the forming coccolith. The coating is achieved via the acidic polysaccharides of the coccolithosomes known as PS1

and PS2. Once the coccolith is complete, exocytosis occurs by the fusion of the vesicle and cell membrane transporting the coccolith to the upper surface of the algae[37]. The roles of the acidic polysaccharides of the coccolithosome have been investigated due to their pronounced role in the formation of these intricate structures that have features over multiple length scales. Using mutation studies, it was concluded that a lack of PS1 did not alter the coccolith mineralization process. However, a lack of PS2 resulted in reduced mineralization, leading to the conclusion that PS2 accelerates the mineralization process. A third polysaccharide PS3 that is found between the membrane of the coccolith vesicle and crystal surface was also included in the mutation studies. PS3 was found to be responsible for shaping the calcite crystals into their unique anvil like morphology because mutants without PS3 produced coccoliths with normal calcite morphology[33]. The way the organic base plate and coccolithosomes containing acidic polysaccharides (PS1, PS2, and PS3) work together to form these inorganic structures shows the delicate balance needed to guide mineral formation across multiple length scales.

Another organism that is able to exhibit an exceptional amount of control over several length scales is the diatom. The diatom is a unicellular eukaryotic algae that contains cell walls called frustules that have intricate patterns in the nanometer to micrometer regime[38]. The formation of these intricate structures is precisely reproduced by organisms of the same species alluding to the fact that the process is genetically controlled[38]. The biosilica is formed in intracellular compartments known as silica deposition vesicles. However insight into the formation of these patterns has been gained by isolating organic molecules from the frustule. The molecules that have been isolated

are long chain polyamines (LCPAs) and proteins known as silaffins. LCPAs have been found in all known species of diatoms while the silaffins are unique to *C. fusiformis*[39].

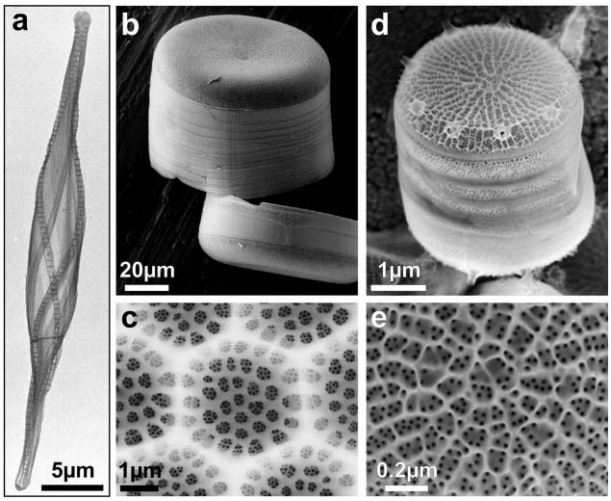

Figure 2.2: Structures of diatom cell walls exhibiting intricate patterns of silica[39].

LCPAs are the longest polyamine found naturally. The structures of these molecules vary amongst species by changing the length, degree of methylation, secondary amine functionality, and quaternary ammonium moieties[38]. LCPAs induce silica precipitation by self-assembling into aggregates that contain charged surfaces. In vitro, LCPAs can induce silica precipitation in minutes by adding multivalent anions such as phosphate[39]. It is believed that the phosphate ions can act as a crosslinker between LCPA molecules due to the hydrogen bond formation and electrostatic attraction. This process facilitates the formation of a LCPA supramolecular assembly that phase separates. This phase separation allows silicilic acid species to adsorb onto or within the aggregate forming a coacervate (liquid precipitate) that polymerizes into silica spheres[39]. The size of the resultant silica particle is controlled by the concentration of phosphate,

where higher concentrations lead to larger particles. In addition, adding an anion with a greater negative charge produced larger particles at lower concentrations[39]. The mechanism of LCPA aggregation driven silica formation has been used to explain many of the intricate patterns formed by these organisms. *Coscinodiscus* creates a honeycomb lattice with 30-50 nm pores. The formation of these pores is explained by the packing of the LCPA aggregates into a hexagonal phase surrounded by an aqueous phase that contains the silica precursor. The silica precipitates and forms a honeycomb network using a fraction of the LCPA aggregate to redisperse into smaller aggregate droplets. The process then repeats itself by surrounding the small aggregates with silica leaving behind a nanopatterned silica network[39].

The other organic molecules involved in the production of biosilica are the silaffins. Three polypeptides have been isolated by treating the diatom frustule with hydrofluoric acid, silaffin-1A, silaffin-1B, and silaffin-2[39]. All three species have a high content of hydroxyamino acids suggesting that the peptides are involved in post-translational modifications. The assumption was proved correct when peptides were isolated using gentler methods. Native silaffins, natSil-1A, natSitl-1B, and natSil-2 were shown to have increased molecular weights[39]. The peptide natSil-1A has three different modified lysine residues that introduce a high number of positive charges (protonated amino groups) and hydrophobic groups. By doing experiments comparing natSil-1A to sil-1A (lacking post-translational modifications), Kröger *et al.* found that these post-translational modifications were essential in order to precipitate silica in acidic conditions that mimic the silica deposition vesicle environment[40]. The dephosphorylation of natSil-1A allows the peptide to be positively charged not allowing it to self-assemble and act as

a template for polycondensation. The other peptide natSil-2 has modified lysines similar to natSil-1 but also has multiple anionic modifications. On its own it cannot produce silica. However, when LCPAs are added, silica precipitates indicating that it may act as an anion required for polyamine phase separation[39]. In addition, at high concentrations natSil-2 has an inhibitory effect suggesting that it may act as a regulator in the process. When combining natSil-1A with natSil-2, silica was formed as polydispersed spheres at high and low concentrations, but, interestingly, at intermediate ratios the proteins formed porous silica blocks with pore sizes between 100-1000 nm, similar to those in diatoms[39]. The same type of structure was formed when combining natSil-2 with LCPAs. Although the exact mechanism is not exactly known, it is clear that the silaffins and the LCPAs define an operating window to form intricate silica structures by using polycationic silica forming molecules that combine with polyanionic molecules whose role is to enable self-assembly and regulate the process[39]. This has been shown by proteins recently isolated from another diatom species *Thalossiosira psuedonana* that also contain a high degree of post-translational modifications. The proteins have many modified lysines, anionic modifications, and, when added to LCPAs, they exhibited the same promoting and inhibitory behavior depending on concentration as the natSil family[38]. Together, the study of both organisms highlights how organic molecules assemble together in a perfect mixture to guide the growth of biogenic silica.

Another example nature provides of directing the growth of inorganic material into several levels of hierarchical structure is in bone formation. Bone is a composite material primarily made up of collagen and hydroxyapatite. The collagen provides the tensile strength and flexibility while the mineral provides the toughness and rigidity[41]. At

the macroscopic level, bones have a variety of shapes corresponding to the numerous functions required in the organism. For example, long bones such as the femur provide stability against bending and buckling while short bones like vertebras provide stability against compression[42]. When the function of the bone is mainly compressive the structure is sponge-like (80% porous), which is called trabecular or cancellous bone found, for example, in the head of the femur or in the vertebrae. Conversely, more dense bone known as cortical bone, has only 6% porosity due mostly to the presence of blood vessels. The blood vessel surrounded by mineral material is known as an osteon. To illustrate lower levels of hierarchy, we will discuss the secondary osteon, which surrounds blood vessels traversing the outer shaft of long bones[42]. The secondary osteon is composed of lamella, which is a planar layer of bone tissue 5 microns thick, which is found in both cortical and trabecular bone. Introducing yet another level of organization, each lamella consists of a series of mineralized fibril layers oriented at different angles to the osteon axis forming a three-dimensional helicoid around the central blood vessel. Interestingly, the angles are always positive forming a non-zero average spiral with right-handed helicity that allows the structure to be compressed and extended. A similar structure has been found in the wood cell wall surrounding the water/nutrient transport system[42].

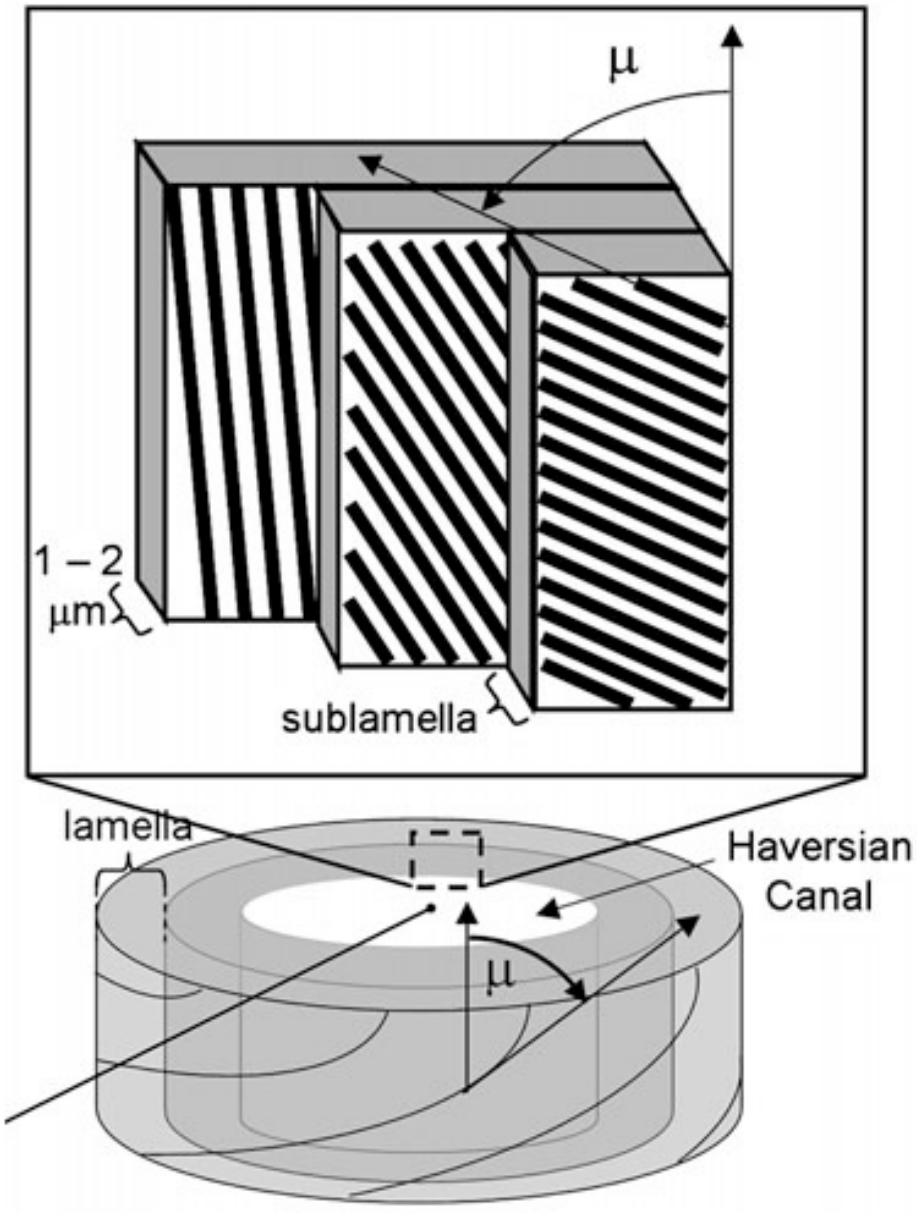

Figure 2.3: A model of fiber orientation inside the lamellae of an osteon. The fibers are arranged at different angles having on average a positive spiral angle μ[42].

As discussed above, the secondary osteon, like most bone, is composed of mineralized fibers. These mineralized fibers are made up of collagen triple helices and hydroxyapatite crystals. The collagen fibrils have a diameter of 80-100 nm[43]. The collagen fibrils make up 85-90% of the organic matrix, with the rest consisting of

proteins and lipids[42]. In collagen type 1, the individual filaments are polypeptide chains α_1 and α_2 that have similar but not identical sequences[42]. At the lowest level of order, these filaments contain primary structure consisting of a repeat of the amino acids glycine, proline, and 4-hydroxyproline. The proline and hydroxyproline residues are believed to cause the irregular twisting of the helices because these amino acids connect back to the primary amine of the polypeptide chain, which restricts the rotation between adjacent residues[42]. The triple helices assemble within the cell with a length of approximately 300nm and are covalently cross-linked with one another to increase the stability of the fibril. The fibrils are constructed from a staggered periodic array of these cross-linked filaments that contains regularly spaced voids[43]. Within these voids, the first hydroxyapatite crystals nucleate with the same periodic spacing of the collagen fibrils[42]. The shape of the crystals is plate like and they are aligned with the fibril axis and the void.

2.2 Inorganic Synthesis of Discrete Integrated Objects Using a Preformed Organic Template

As mentioned earlier, the formation of inorganic material can either happen cooperatively or the organic matrix can be preformed to guide the formation. In addition, the biomimetic molecules can form discrete integrated objects or higher order assemblies. Here, we will discuss the formation of discrete integrated objects using preformed organic matrices and a variety of biomimetic molecules. The first approach discussed has

been termed nanoscale incarceration, and it consists of self-assembled organic architectures that contain a hollow interior used as a reactor for inorganic nanoparticles[32].

2.2.1 Nanoscale Incarceration

A model molecule that demonstrates nanoscale incarceration is an iron storage protein found in eukaryotes called ferritin. It contains 24 subunits that self-assemble into a spherical cage with an outer diameter of 12 nm and an inner diameter of 8 nm. There are two types of ferritin subunits, H and L. The H subunits are responsible for iron loading and oxidizing iron, while the L subunits are responsible for nucleation making the protein bifunctional. For these reasons, Kramer *et al.* have chosen to modify the ferritin molecule and use them as reaction vessels with controlled dimensions. Using phage display, they identified a dodecapeptide that was capable of reducing Ag^{+} ions to Ag^{0} nanoparticles with polyhedral morphologies and an average diameter of 102 nm. Subsequently, they fused this peptide to the C-terminus of L chain ferritin[44]. They showed that adding the peptide to the ferritin molecule had no effect on the self-assembly and that upon addition of silver precursor solutions, the engineered protein cage formed spherical particles with an average diameter of 7 nm when the experiment was done *in vivo* and 5 nm *in vitro*[44]. Other groups have also attempted to modify ferritin to incorporate the ability to form non-native nanoparticles. Butts *et al.* used a computational modeling approach in order to locate residues to modify on both the exterior and interior of human H-ferritin. They successfully genetically modified the native protein to include more cysteine residues in the interior of the cage and less on the exterior giving it the ability to form silver and gold nanoparticles[45]. Both these

approaches for nanoparticle formation used incarceration mechanisms similar to the formation of CdS by plants, yeast, fungi and bacteria.

2.2.2 Wrapping

Other ways of forming inorganic structures that material scientists have been employing is by coating an organic structure with the inorganic material. This process is called wrapping, and it contains no surface patterning but still creates a hybrid material with unique properties. The coating of organic molecules with silica shells is an example of this process. A variety of molecules have been used that range from proteins and chimeric proteins to peptide amphiphiles and rationally designed peptides.

Shiomi *et al.* have used the abundant lysozyme protein to induce silica precipitation at a basic pH. They found that traditional stirring formed lysozyme-silica hybrid granular particles but, using sonochemical treatment, they formed lysozyme-silica hybrid hollow particles[16]. They attributed the formation of hollow particles upon sonication to the dispersion of the silica precursor within the lysozyme solution forming precursor droplets covered in a lysozyme layer, allowing precipitation on the inside and outside of the layer[16]. Using poly-L-lysine, Tomscak *et al.* showed that silica condensation could be achieved in different morphologies by varying the length of the biopolymer. They found that the short chain poly-L-lysine formed spherical silica particles and by increasing the chain length hexagonal silica platelets formed[46]. They attributed this change in morphology to the poly-L-lysine molecule forming helical chains in the presence of the silica precursor and phosphate ions. These chains

subsequently formed a hexagonal lattice, which served as the template to the formation of hexagonal silica platelets[46].

Another approach taken has been to use chimeric proteins to from new silica composites. Wong Po Foo *et al.* combined properties from a silaffin protein and a spider silk protein to form a novel fusion protein containing both silica precipitation activity and a highly stable β -sheet structure with impressive mechanical properties[47]. The inclusion of the R5 peptide, which was derived from the silaffin protein, contributed the silica precipitation activity at neutral pH, whilst the domains from the major ampulate spidroin 1, a spider silk protein, provided the highly stable β-sheet structure and mechanical strength. In addition to precipitating silica at neutral conditions, using this chimeric protein allowed for the formation of films and fibers attributed to the unique processing ability of the spider silk protein domain[47]. A similar approach using a chimera consisting of a spider silk protein with a hydroxyapatite nucleating domain from a dentin matrix protein produced a silk hydroxyapatite composite with potential applications in bone tissue engineering[48].

The Hartgerink lab also attempted to form composites using a rationally designed molecule. Yuwono *et al.* designed a peptide amphiphile that would self-assemble into nanofibers and serve as a template for silica precipitation[49]. They designed several variations of their peptide amphiphiles to verify the effect of single amino acid modifications on both the self-assembly and mineralization. They concluded that all the molecules self-assembled into fibers containing β -sheet secondary structure, but they each had their unique conditions for nanofiber formation based on the pIs of the single amino acid modification[49]. In addition, they discovered that amino acids containing

amine groups were required to catalyze silica precipitation and that molecules containing a longer peptide sequence (all tail lengths were kept constant) formed nanotubes with a larger diameter. An image of the silica-coated nanotubes can be seen in figure 2.4. As a final step, they calcinated their composite structures to form hollow nanotubes[49]. Other groups have also used a similar approach to form hollow nanostructured silica fibers. Meegan *et al.* used a rationally designed peptide molecule that was designed to self-assemble in one dimension into antiparallel β -sheets. They showed that their molecules formed amphiphilic tapes that stacked into ribbons and later fibrils that acted as a template for silica precipitation only when the hydrophilic portion of the molecule contained a net positive charge[50]. Using a similar approach, Atunbas *et al.* designed peptides (MAX 1 and MAX 8) to form β-hairpin molecules upon stimulus. These β-hairpin molecules assembled into intermolecular β -sheet bilayers that hydrogen bonded laterally to form fibrils with a high density of lysine groups on the exterior surface for silica precipitation[51]. The entanglements and branching of these molecules yielded a hydrogel containing a shear modulus that could be tuned by varying the peptide to silica precursor ratio[51]. Also using rational design the Woolfson lab designed two α-helical molecules that co-assemble into a staggered α -helical heterodimer. The ends of these molecules were designed to be complimentary in order to induce fibril formation[52]. The fibrils formed had a net positive charge and induced silica deposition. The novelty of their design was that unlike other templates they used an α-helical based molecule and they engineered kinks and branches into their silica fibers by modifying their assemblies to include orthogonal conjugates in which dimers were formed using two copies of the N-

terminal half of one of the peptides[52]. In addition, they showed that the removal of the peptide portion also resulted in hollow nanotubes[52].

The examples just mentioned formed silica coats on a variety of different molecules forming silica particles, hollow particles, nanotubes, hollow nanotubes, films, kinked nanotubes, and silica-hydrogel networks with tunable shear moduli. The variety of structures and organic molecules could be used for various applications ranging from controlled release drug delivery to the encapsulation of enzymes to retain their stability under harsh conditions. Many of the principles used in the design of the molecules discussed borrow functionalities and assembly mechanisms from diatoms.

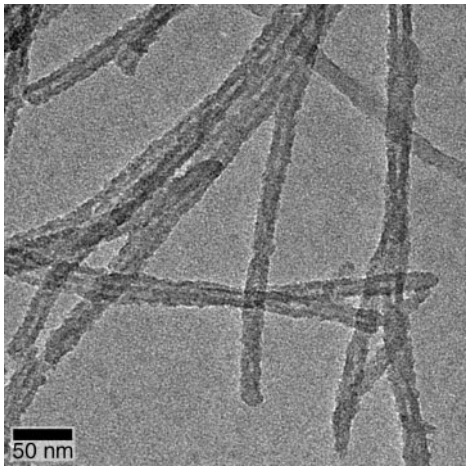

Figure 2.4: Silica coated peptide-amphiphiles[49].

2.2.3 Templating

The first approach discussed here was chosen because it illustrates the difference between uniformly coating a material and templating. The Stupp laboratory provided another elegant example of using biomimetic molecules to template inorganic material in 2001. They designed a peptide amphiphile that incorporated five different features: an alkyl tail responsible for making the peptide amphiphilic and prone to self assembly, four

cysteine residues that would impart cross-linking capability to the molecule, three glycine residues that would give the head group of the surfactant flexibility, a single phosphoserine residue that would coordinate Ca^{2+} ions, and the RGD peptide sequence known to promote cell adhesion[53]. The self-assembly of this molecule formed a cylindrical micelle or nanofiber with the alkyl tails in the interior and the peptide domain on the exterior. After oxidation of the cysteine groups and addition of $CaCl_2$ and Na_2HPO_4, the fibers were coated in hydroxyapatite crystals that aligned with the c-axis of the peptide amphiphile. As a control they also synthesized a peptide with out phosphoserine, which resulted in amorphous coverage of hydroxyapatite, suggesting that the coordination of the Ca^{2+} ions with the phosphoserine are crucial in the alignment of the crystals with the c-axis of the peptide amphiphile[53]. Also, using a peptide amphiphile, Cavalli *et al.* formed habit modified crystals of calcium carbonate by forming monolayers of their peptide amphiphile at the air/water interface. By allowing them to incubate with calcium bicarbonate solutions they formed indented calcium carbonate crystals because the peptides rearranged due to the growing inorganic phase, which caused a reorientation of the molecule, exposing functional groups that stabilize different crystal planes[54]. Another study using peptide amphiphiles also showed how different functional groups can influence a preference for different crystal facets. Mitra *et al.* used four different peptide amphiphiles that formed into hydrogels to form gold nanoparticles *in situ*. All four varieties incorporated tryptophan in their sequence as a weak reductant, but contained modified head groups and hydrogel porosity. The different head groups attributed to a preference for different facets led to particles of varying shapes: triangular platelets, wires, and octahedral particles. The differing porosity of the

hydrogels caused the formation of larger decahedral particles in the hydrogels with greater porosity and smaller octahedral particles in the hydrogels with lesser porosity[55]. As can be seen in each of these examples, templating involves growing inorganic material where the crystals are oriented in a particular direction or have a particular facet due to the nature of the organic templating molecule.

Other examples of templating use rational peptide design via determination of secondary structure as a tool to control inorganic crystallization. DeOliviera and Laursen controlled the morphology of calcite crystals by using a peptide designed to be α-helical, where the peptide contains spatially coordinated aspartic acid residues designed to bind to the $\{10\bar{1}\}$ face of calcite. Interestingly, they found that at lower temperatures the peptide was 89% helical and produced crystals with growth along the c-axis, suggesting that the peptide recognizes the specific crystal surface, whilst the unfolded peptide produced crystals with growth along all six rhombohedral surfaces[56]. Similarly, Ajikumar *et al.* designed peptides to mimic eggshell matrix proteins and formed polycrystalline calcium carbonate aggregates (similar to the parent protein) only when the peptides formed a β-sheet secondary structure[57]. Other peptide-based approaches have focused on using phage display to identify peptide sequences with affinity for the particular material. Dickerson *et al.* used this method with titania single crystals. They found that the sequences with high affinity had strong enrichments in arginine, lysine, and histidine and used this knowledge to design a series of 16 amino acid long sequences with a minimum charge of +2. Upon mineralization, they found that they produced nanoparticles with less than 10 nm anatase and monoclinic β titania domains. The concentration of nanoparticles was shown to increase in concentration with increasing

positive charge, allowing them to combine their observations and design a peptide with high precipitation activity[58]. Also using phage display, Umetsu *et al.* identified sequences with affinity to ZnO and added a GGGSC linker to the highest affinity peptide for flexibility, and the mineralization activity of cysteine, resulting in the room temperature synthesis of novel flower type morphology of ZnO nanoparticles[59]. An image of the flower morphology ZnO nanoparticles can be seen in Figure 2.5.

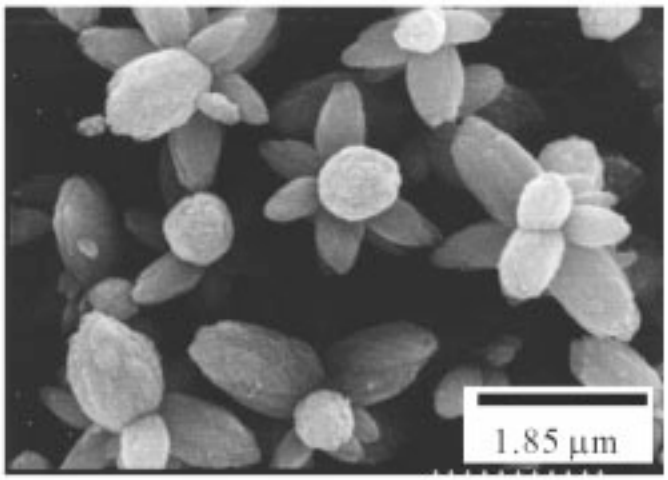

Figure 2.5: SEM image of ZnO nanoparticles exhibiting a flower morphology[59].

Block co-polypeptides, having similar characteristics as peptides, can also be used in templating of inorganic material using similar strategies. For example, Euliss *et al.* designed a block co-polypeptide comprised of a hydrophilic anionic block and a α-helical hydrophobic segment to make calcium carbonate spheres. Several block co-polypeptide designs were constructed to investigate the nature of the process, and the authors concluded that polyglutamic or polyaspartic blocks were responsible for the affinity for Ca^{2+}, whilst the α -helical segment kept the growing crystal nuclei in solution eventually producing crystals with a size limited spherical morphology[60]. The absence of the α-

helix secondary structure (using randomly ordered blocks instead of a sequence adopting an α-helix), the peptides produced calcium carbonate crystals with irregular morphologies, as did homopolymers of glutamate and aspartate[60]. Similarly, Jan *et al.* used block co-polypeptides to form inorganic metal oxide, metal halide, and composite spheres. They designed amphiphilic block co-polypeptides using lysine and phenylalanine blocks that self-assembled to form vesicles of varying size depending on the length of the block[61]. Using these vesicles as a template, they used silica precursors to make silica hollow spheres or silica spheres by manipulating the lysine to phenyalanine ratio. Additionally, they formed silver bromide spheres of varying sizes by manipulating the concentration of silver nitrate. Combining those two approaches, they formed silver bromide/silica core shell particles that varied in size and composition. The two tuning protocols in a single biomolecular design allowed for control over the self assembly of the organic phase as well as control over the final silver/silica state by incorporating a reducing agent[61].

2.3 Higher Order Self-Assembly Using a Preformed Organic Matrix

Instead of the formation of a single hybrid object, biomimetic molecules can also be used to form higher order assemblies. This entails going beyond the formation of a hybrid material to find ways to assemble the hybrid material in an orderly fashion. The natural examples discussed earlier provide great examples of hierarchical levels of control. Here, we will discuss the formation of unitary discrete nano-objects and extended nanostructures using a preformed organic matrix.

2.3.1 Unitary Discrete Nano-objects

In the example of templating with block co-polypeptides, we discussed the formation of composite particles of silver bromide/silica and silver/silica. These particles are an example of unitary nano-objects because they involve the co-organization of two types of materials to form a uniform composite nanostructure. An additional example of the formation of unitary nano-objects is the formation of bimetallic particles by Slocik and Naik. Using a multifunctional peptide ligand, they were able to form a 15 nm particle that was comprised of a larger gold particle that had smaller palladium particles on its surface[62]. This was achieved by synthesizing a peptide containing two separate domains, one for synthesizing and stabilizing gold nanoparticles, and the other designed to recognize antibodies and bind palladium and platinum. The gold nanoparticle was first formed and stabilized using the peptide that was subsequently exposed to Pd^{+} ions and reduced to form the smaller palladium particles on the gold surface[62].

2.3.2 Extended Nanostructures

The formation of extended nanostructures is another type of higher order assembly that can be achieved with the aid of biomolecules. Several examples of these higher order assemblies exist that apply similar techniques used to form discrete integrated objects, but, in order to form extended nanostructures, one needs to incorporate additional directing elements to arrange these discrete objects in a particular extended architecture. An example of how nanoscale incarceration can be taken a step further to incorporate an additional dimension of complexity is demonstrated by redesigning a heat

shock protein that forms an octadecanoic double ring cage structure called chaperonin. McMillan *et al.* removed the central loop of the protein in order to allow access to its central core and added several histidine residues to the amino terminus to increase affinity for metal ions. In doing so, they were able to form either Ni-Pd or Co-Pd in the core of chaperonin, which self-assembled into two-dimensional arrays forming regularly spaced nanoparticles[19]. Also using an incarceration molecule, Sano *et al.* added a titanium binding peptide with silification activity that would display itself on the surface of ferritin. They then used layer-by-layer assembly to create heterogeneous multilayer nanostructures by alternating monolayers of different metallic nanoparticles within ferritin with layers of silica precipitated using the ferritin surface[63]. Another clever redesign of a protein that created higher-level structures was accomplished by combining a copper oxide binding peptide with a DNA binding protein. Dai *et al.* formed copper oxide nanoparticles that were surrounded by the engineered protein shell. By adding DNA that forms circular confirmations they were able to form DNA loops with regularly spaced copper oxide particles[64].

Several examples of extended nanostructures focus on the formation of nanoparticle linear arrays. The Stupp laboratory used a tripeptide amphiphilic molecule and an amphiphilic molecule containing a thymine moiety to assemble into nanofibers. They then introduced gold nanoparticle functionalized with diamniopyridine to form linear arrays of nanoparticles[65]. The Matsui lab has also formed linear arrays of nanoparticles using nanotubes formed using bolaamphiphile molecules as templates. They incubated the previously formed nanotubes with various different peptides and metal precursors resulting in linear arrays of gold[18, 66], zinc selenide[67], nickel[27],

platinum[68], and copper[69]. They showed that by changing the pH of the solution they could change the conformation of the peptide resulting in larger particles when the peptide was in an aggregated state since the nanoparticle had more space to grow[27, 69]. Additionally, using peptides that did not change conformation, they showed that they could increase the packing density of nanocrystals on the nanotubes by varying pH thus affecting the ionization state of the amino acids and increasing the number of nucleation sites[66, 68]. In the case of ZnS, they could vary between monodisperse particles, a wurzite crystalline structure, and no crystallinity by changing the pH, which affected the folding of the peptide[67]. Another example of producing linear arrays of particles was the templating of nanostructures using larger more complex pre-assemblies such as tobacco mosaic virus. The tobacco mosaic virus consists of 2130 protein subunits arranged in a helical configuration around single stranded RNA that has internal and external repeated patterns of charged amino acids[70]. By addition of several metallic precursors, Shenton *et al.* demonstrated that this viral template produced CdS, PbS, iron oxide, and silica coated viral particles, and, in the case of iron oxide and silica, these particles had lengths greater than that of the template suggesting end to end assembly[70]. In an extension of that work, Dujardin *et al.* used the same cylindrical template but manipulated the ability of the particles to form on the interior or exterior of the viral template by adjusting the pH, leading to changes in the ionization state of the charged amino acids[71]. Similarly using a different virus, Nam *et al.* reengineered the coat protein of the virus to contain tetraglutamate to enable interaction with metal ions. They successfully coated the protein with cobalt oxide particles using a cobalt precursor and a reductant. In addition, they added a gold binding motif to the coat protein and bound a layer of previously formed

gold nanoparticles followed by a layer of cobalt oxide[3]. Similarly Slocik *et al.* have used a cowpea chlorotic mottle virus that was modified to include a gold binding peptide to produce linear arrays of gold nanoparticles without the aid of a reductant. The surface of the virus contained various tyrosine residues responsible for the reduction of the gold precursor, while the gold binding peptide coordinated the gold nanoparticles in their specific location[72]. However, using a different gold precursor and a reductant, they formed more regularly spaced nanoparticles in 3D arrangements[72]. Lamm *et al.* used rational peptide design to form regularly spaced gold nanoparticles using a peptide designed to adopt a β-strand confirmation and self-assemble into β-sheet fibrils. They cleverly used two L-Proline residues in their sequence to interrupt the natural left handed twist of the β -strand, forming non twisted β -sheet fibrils that had positively charged lysine molecules spaced every 2.5 nm[73]. By adding negatively charged gold nanoparticles to a solution containing their designed peptide, they formed arrays of regularly spaced particles[73]. An image of the gold nanoparticle linear arrays can be seen in figure 2.6. Work in the same laboratory produced nanoparticle arrays using a peptide that adopted a β-hairpin structure containing regularly placed histidine segments forming arrays with nanoparticle spacings of approximately the same size as the histidine segment spacing[74].

In addition to one-dimensional arrays, attempts have been made to form two-dimensional arrays. Carter *et al.* have combined two DNA types composed of 9 oligonucleotides to form a two-dimensional nanogrid. They covalently added a gold binding peptide sequenced using phage display to one of the DNA types eventually forming two dimensional arrays of gold nanoparticles[75].

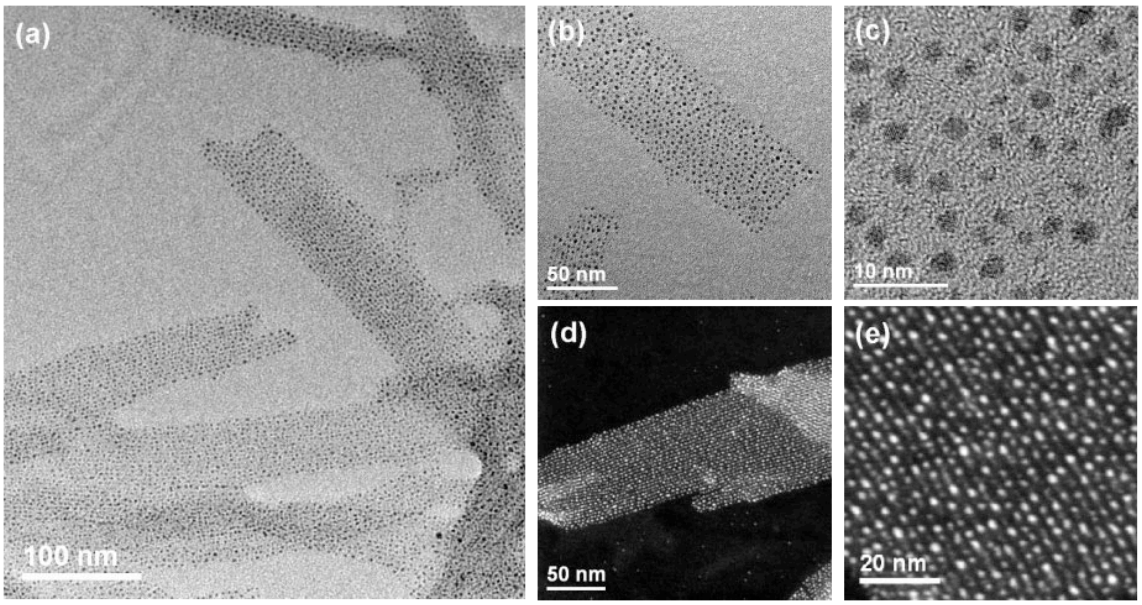

Figure 2.6: (a) and (b) Bright field TEM images showing peptide-fibril gold nanoparticle assemblies at different magnifications. (c) High resolution TEM showing particles immobilized on the peptide fibril. (d) and (e) High angle annular dark field STEM showing the high degree of particle alignment[73].

Other interesting examples of extended nanostructures use non-linear template architectures. Euliss et. al used block co-polypeptides to form a stable cluster of 20 nanoparticles. They designed a block co-polypeptide containing an aspartic acid block to bind to the surface of previously synthesized maghemite particles[17]. Since the nanoparticle bound with more than one strand of block copolypeptide and vice versa, this resulted in a bridged aggregation. By doing experiments with a homopolymer of just the aspartic acid block, they concluded that the non-binding block of the molecule formed the outer shell of the assembly limiting the size of the cluster[17]. Slocik and Naik developed another unique assembly, where the authors used previously formed gold nanoshells functionalized with thiol moieties, attaching the shells to matching anti-parallel coil motifs[76]. When the two separate functionalized nanoparticles were mixed they formed a coil-coil interaction binding the nanoparticles together. Using the infrared-absorbing

properties of the gold nanoshells, they were able to disassemble the particles using near infrared light and reassemble them upon cooling[76]. In addition, they conjugated cysteine modified quantum dots to one of the peptide motifs forming gold nanoshells with multiple quantum dots on the surface. The proximity of the nanoshells to the quantum dots in the assembly resulted in a quenching of the fluorescence. However, upon irradiation, the quantum dots retained their fluorescence because of the change in the nanoshell to quantum dot distance[76].

2.4 Co-Assembly of Hybrid Materials

All of the previous examples described contained approaches of forming inorganic structures using a preformed organic matrix. This section discusses the co-assembly or co-formation of hybrid organic/inorganic structures.

Pouget *et al* discuss an elegant example of this cooperative process, where the authors use a dicationic octapeptide called lanreotide and the silica precursor tetraethylorthosilicate to form co-assembled double-walled silica peptide nanotubes that self-assembles into centimeter sized fibers[77]. The assembly was mediated by a delicate balance achieved between the positively charged peptide surface and the negatively charged silica precursor. As the peptides assemble, silica polymerization is activated by the slight excess of peptides. Conversely, the peptide assembly/disassembly is shifted towards longer structures by the continuous neutralization provided by the association of the negatively charged silica[77]. Although the lanreotide molecule self-assembles into nanotubes in water via hydrophobic interactions, the self-assembly is limited because of the electrostatic repulsion of the molecules, which is why the addition of the silica precursor mediates this repulsion allowing for the formation of long structures that span

six orders of magnitude, from the single fiber with an inner diameter of approximately 15nm and outer diameter of approximately 29 nm and a length between 1-3 μm to bundles of these fibers aligned in a common direction up to centimeters in length[77]. The combination of the self-assembly of the organic phase and the polymerization of silica allowed the resultant structure to have dimensions that were not limited by the size of the assembled organic matrix[77]. A schematic of the proposed co-organization is shown in figure 2.7. Lee *et al.* also co-organized organic and inorganic components using a genetically altered virus. By adding a peptide with affinity for cobalt to the coat protein, they successfully arranged the viral cylinders into bundles with the addition of cobalt ions to the system[78]. Although the virus structure was not assembled, the addition of the cobalt binding domain and cobalt ions allowed the viral structures to assemble into bundles that could not be accomplished without the incorporation of the cobalt-binding domain. In addition, they added platinum precursor and reductant to form bundles of viruses with Co-Pt on the surface[78]. Another example of co-assembly was discovered by Djali *et al.* using bolaamphiphile peptide monomers and trimethylphosphine gold. Without the gold precursor, the bolaamphiphile peptide assembles into nanotubes[18], but, in the presence of trimethylphosphine gold, the peptide self-assembles into a nanodonut, where UV radiation serves as a nanoreactor for the constrained synthesis of the gold nanoparticles[18].

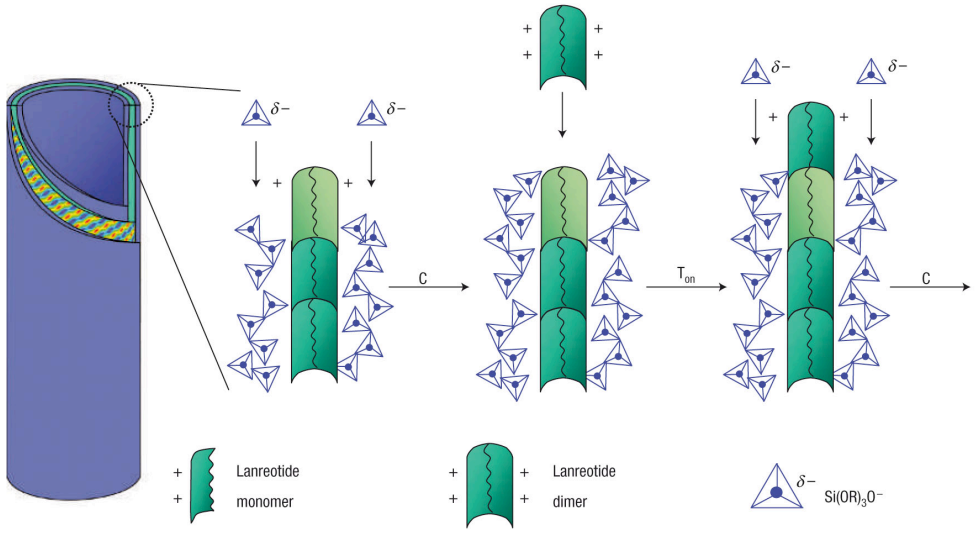

Figure 2.7: Dynamic template model proposed as the mechanism for the co-assembly of lanreotide and silica. The cationic nanotube surface catalyzes the silica condensation by electrostatics (step C), and the anionic silica deposit promotes lanreotide assembly (step T_{on})[77].

Many of the more impressive examples of co-assembly occur when self-assembly, nucleation, and growth processes occur simultaneously. The Rosi lab has provided an elegant example of this using a peptide evolved and isolated using phage display attached to an aliphatic carbon tail. The combination of the designed molecule, HEPES buffer, and chloroauric acid co-assembles to form double helical gold nanoparticle assemblies without the use of an external reducing agent[79].

In the previous sections, a variety of biomimetic molecules were used to form either discrete hybrid entities or hybrid entities assembled into a higher level of organization. In addition, the processes leading to these nanostructured materials were the result of either a preformed organic template or a simultaneously co-assembled composite. The next section will discuss the underlying principles that guide the formation of intricate hybrid materials.

2.5 Governing Principles

The principles that allow biomimetic molecules to direct the growth of inorganic material can be divided into self-assembly of the organic phase and nucleation and growth of the inorganic phase. Of course, as mentioned previously these processes may occur simultaneously. In addition, when these processes occur within organisms as described in the natural examples section, additional levels of complexity are introduced by genetic and environmental factors that are unique to each particular organism.

2.5.1 Self-Assembly

In general, self-assembly is a process that allows disordered molecules to form an ordered structure as a consequence of the specific non-covalent interactions between the molecules. The self-assembly of amphiphilic molecules is largely an entropically driven process in which hydrophobic interactions cause molecules to self-assemble. The process is driven by the free energy decrease obtained when the hydrophobic parts of the molecule rearrange to avoid water, increasing the entropy of the associated water molecules. Although hydrophobic effects are the major driving force for amphiphilic systems, other interactions such as electrostatics, hydrogen bonding, dipole-dipole, and van der Waals, contribute to self-assembly as well. Electrostatic, hydrogen bonding, dipole-dipole, and van der Waals scale as $1/r$, $1/r^2$, $1/r^3$, and $1/r^6$, respectively[32]. Of these, the electrostatic and hydrogen bonding contributions are often of greater importance because of the magnitude of their interactions. Electrostatic interactions can either favor or disfavor self-assembly depending on whether the interaction is attractive

or repulsive, respectively. Hydrogen bonding between adjacent molecules favors self-assembly by forming hydrogen bonds between neighboring molecules.

Thermodynamically, the force driving aggregation between molecules can be expressed as a chemical potential, μ. It can be stated that:

$$\mu_N = \mu_N^o + \frac{kT}{N}\log\left(\frac{X_N}{N}\right) \text{ and,} \tag{2.1}$$

$$X_N = N\left[X_1 \exp\left(\frac{\mu_1^o - \mu_N^o}{kT}\right)\right]^N \tag{2.2}$$

where, μ^o_N is the standard chemical potential, X_N is the concentration of aggregates, and N is the number of monomers in an aggregate. To drive aggregation, the chemical potential of the aggregate must be less than the chemical potential of the monomer[31].

In general, the concentration at which monomers aggregate to form structures is commonly called the critical micelle concentration (CMC), where the free energy can be expressed by:

$$\Delta G^o = \mu^o_{micelle} - \mu^o_{water} = RT\ln[CMC] \tag{2.3}$$

If we treat the transition between monomers and aggregates as a chemical reaction in equilibrium then:

$$NS \Leftrightarrow S_N \text{ and,} \tag{2.4}$$

$$K_N = [S_N]/[S]^N, \tag{2.5}$$

where S is the monomer concentration, S_N is the concentration of aggregates of N amphiphiles, and K_N is the equilibrium constant. Thus, the CMC is the total concentration, $[S]_T$, in which molecules entering the system start to enter aggregated structures preferentially[31].

$$[S]_T = N[S_N] + [S] = NK_N[S]^N + [S] \text{ and,} \tag{2.6}$$

$$\frac{\partial\{N[S_N]\}}{\partial[S]_T}\Big|_{CMC} = \frac{\partial[S]}{\partial[S]_T}\Big|_{CMC} = 0.5 \tag{2.7}$$

By solving these equations one obtains:

$$\{[S]_{CMC}\}^{N-1} = \left(N^2 K_N\right)^{-1} \text{ and,} \tag{2.8}$$

$$CMC = [S]_{CMC}\left(1 + N^{-1}\right) = \left(N^2 K_N\right)^{-1/(N-1)}\left(1 + N^{-1}\right) \tag{2.9}$$

Assuming that N>>1, then ln N/N $\rightarrow$ 0 and,

$$\Delta G^o = RT\left[\frac{-1}{N-1}\left(2\ln N + \ln K_N\right) + \ln\left(1 + \frac{1}{N}\right)\right] \text{ or,} \tag{2.10}$$

$$\Delta G^o = RT \ln K_N \tag{2.11}$$

Therefore, the free energy driving the formation of aggregates is directly related to the equilibrium constant between molecules in a monomeric state and molecules within an aggregate. This equilibrium constant can be shifted in either direction by utilizing hydrophobic, electrostatic, and hydrogen bonding interactions.

2.5.2 Nucleation and Growth

In order for the molecules that were self-assembled in the previous section to direct the growth of an inorganic phase, the constituents of this inorganic phase must first be nucleated on the interface between ions in solution and the organic phase. The ion belonging to the specific crystal being formed will bind at the interface if the conditions are favorable. Those conditions include: spatial charge distribution, lattice geometry,

hydration, and stereochemical requirements. All of these parameters contribute to crystal nucleation.

In classical homogeneous nucleation theory, the free energy of nucleation that drives the formation of a nucleus contains contributions from both the interfacial (ΔG_I) and bulk (ΔG_B) free energies. The interfacial free energy is positive and the bulk free energy is negative. If one assumes that the cluster of particles that assemble a nucleus is spherical, then the interfacial energy is proportional to the surface area ($4\pi r^2$) while the bulk free energy is proportional to the volume ($4\pi r^3/3$). A schematic of these energies can be seen in the figure below.

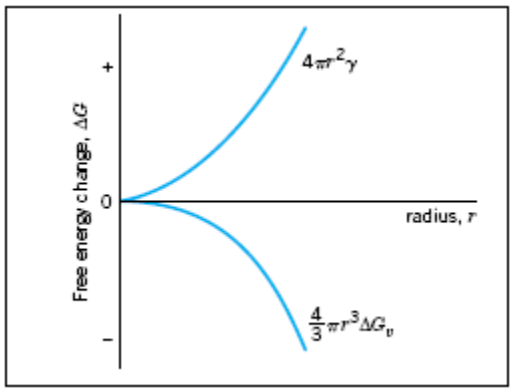

Figure 2.8: The interfacial and bulk free energies as a function of radius[80].

Combining the bulk and interfacial free energies yields the free energy of nucleation, which is described by the following equation[80]:

$$\Delta G_N = \Delta G_I - \Delta G_B = 4\pi r^2 \sigma - \frac{4\pi r^3 \Delta G_V}{3V_m} \qquad (2.12)$$

In this equation, σ is the interfacial free energy per unit surface area, V_m is the molar volume, and ΔG_v is the free energy per mole associated with the solid liquid phase change. Combining all the free energy contributions leads to the schematic below, in

which the maximum of the free energy of nucleation is termed the critical free energy, and it is located at a critical radius, r*.

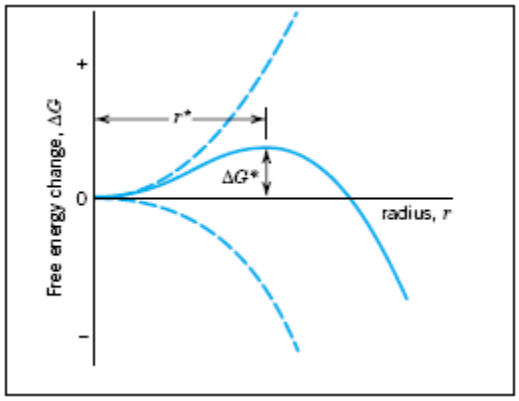

Figure 2.9: Free energy change versus radius, the free energy maximum is termed ΔG^* and is located at the critical radius (r^*)[80].

This critical free energy is the energy barrier that needs to be overcome to form a stable nucleus. The thermodynamics also defines the critical radius that needs to be overcome to form a stable nucleus. If this critical energy barrier is not overcome (or the critical nucleus size is not reached), then the cluster of particles will dissolve back into solution. Once the barrier has been crossed nucleation is favored. By solving for the maximum of the free energy curve, one can obtain the critical free energy of nucleation described by the equation below[80]:

$$\Delta G^* = \frac{16\pi\sigma^3 V_M^2}{3\left(kT\ln S\right)^2} \tag{2.13}$$

In this equation, k is Boltzmann's constant, S is the degree of supersaturation, and T is the temperature. The remaining variables are the same as those previously defined.

In general, organic molecules help induce nucleation by lowering the interfacial energy, which, in turn, lowers the free energy resulting in the formation of a stable

nucleus. In addition, the depths and shapes of energy minima control equilibrium crystal phase and habit. Using additives or organic matrices can vary the heights of energy barriers leading to control over the growth kinetics resulting in the stabilization of non-equilibrium or intermediate states[81].

Once stable nuclei have formed, the next step is crystal growth. The growth of a crystal takes place by the deposition and incorporation of solute molecules from the bulk solution onto the steps of crystal surfaces allowing the crystal to advance quickly along the surface, perpendicular to the step[81]. The steps formed are incomplete containing kinks that are the most active sites for growth. The growth of crystal facets occurs in a spiral pattern using screw dislocations that provide an unending source of steps. Therefore, the parameters controlling growth rate are (1) the energy required to create a step at the crystal interface and (2) the free energy barrier for an adsorbed solute molecule to be incorporated into the crystal. This can be described by the following equation:

$$\Delta G = -n\Delta\mu + 2a\gamma_{step} \tag{2.14}$$

Where, n is the number of growth units absorbing to the surface, $\Delta\mu$ is the change in chemical potential per growth unit during this phase transformation ($\Delta\mu \propto \ln S$), a is the diameter of a newly added growth unit and γ_{step} is the free energy of the step edge[82]. Using this equation and calculating n = L/a, where L is the length of step, one can solve for the critical length L_c. This critical length describes the length where the step will begin growing outward and where the following step will develop[82].

The delivery of molecules to the step is governed by diffusion of solute molecules from solution to the kink. Therefore at low supersaturation conditions the incorporation

of growth units into kinks is the rate limiting step, which is not the case for high supersaturation conditions in which two-dimensional nucleation occurs on existing surfaces. This spiral growth model was first developed by Burton, Cabrera, and Frank[83].

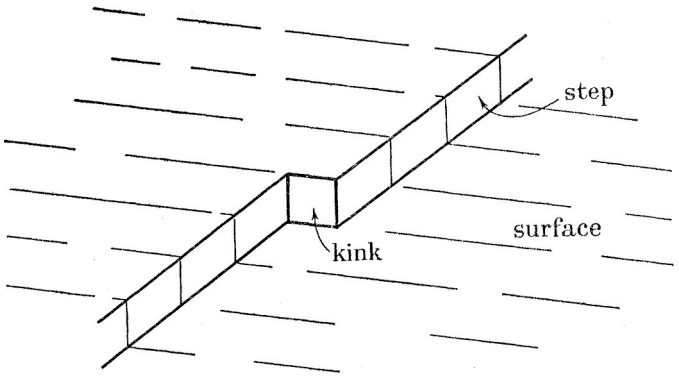

Figure 2.10: The presence of a kink in a step on a crystal surface[83].

To investigate the kinetics of crystal growth and learn more about the mechanisms of this phenomenon, two experimental techniques have been particularly useful. The first technique is a bulk method used to measure growth rates called constant composition kinetics. This technique uses quantitative control over parameters affecting crystallization[81]. During crystallization, as crystal precursors are removed from solution, the growth rates are measured by using the titrant addition rates required to keep the solution at a constant composition[81]. The other method uses scanning probe microscopy to directly observe the dynamics of crystal growth in real-time, enabling the measurement of the growth velocities of steps. In order to use scanning probe microscopy, the solution must be in a metastable region in which the solution is supersaturated but not enough to promote crystals to spontaneously precipitate from solution[84]. This state of the solution allows growth on existing crystal surfaces only, therefore the location of the probe can be positioned on the existing crystal surface. This limits the kinetic information obtained

using this technique to conditions of moderate supersaturation in which two-dimensional nucleation does not take place[84]. The growth velocities of steps are described by the following equation:

$$v = \beta(a - a_e) \tag{2.15}$$

where, β is the kinetic coefficient and a and a_e are the actual and equilibrium solute activities[85]. The kinetic coefficient can be described by:

$$\beta \propto n_k e^{\left(-\frac{E_k}{kT}\right)} \tag{2.16}$$

where, n_k is the density of kink sites and E_k is the effective barrier of attachment to a kink[85]. These kinetic equations are useful in evaluating the data obtained from scanning probe microscopy.

The recent development of the two experimental techniques described above has led to novel insight in the ways biological molecules can affect crystal growth. Many of the studies have focused on the formation of biominerals (biomineralization); nonetheless, they reveal insights into the growth mechanisms of a wide variety of inorganic materials. Using the Burton, Cabrera, and Frank model for spiral crystal growth, the addition of additives to the solution can succeed in controlling rate or shape by altering the kink or step density, changing the kinetic barriers associated with moving ions between the solution and the solid by pinning or blocking step motion and chelating solution ions by reducing supersaturation or incorporation into a solid[84]. Subsequently, the shape of the crystal is modified altering specific steps or facets[84]. We will discuss examples of the specific mechanisms used to alter steps or facets below.

By studying the growth of calcite in the presence of amino acids, Orme *et al.* were able to conclude that the addition of the amino acids to the growth medium changed step-edge free energy (γ_{step}), resulting in macroscopic crystal shape modifications. In addition, by using both enantiomers of glutamic acid, they showed that the amino acid must interact with at least two sites on the calcite face, otherwise, no variations would be observed between the enantiomers[86]. This study showed that although stereochemical factors contributed to the interaction with a particular edge of calcite, the stereochemical complementarity between an entire facet and the templating molecule was not necessary[86].

Previous biomineralization literature has focused on direct stereochemical matching between a templating molecule and the resultant crystal, as has been illustrated by the complementarities in the spacing of the β-sheet in silk fibroin and aragonite[87]. Similarly, Fu *et al.* studied the kinetics of calcite formation and also concluded that lowering the step free energy resulted in the accelerated kinetics they were observing. They performed experiments with two proteins isolated from abalone shell nacre, and the authors were able to attribute the accelerated kinetics of specific atomic steps on the (104) face to the proteins acting as surfactants promoting ion attachment[88].

An example of how changing the kinetic barriers associated with moving ions between the solution and the solid was provided by Elhadj *et al.* They studied the effect of a variety of small peptides and proteins on the kinetics of calcite formation. They specifically studied a region of growth acceleration induced by relatively low concentrations of their molecules in which the velocity as function of supersaturation remains linear. Therefore, using the equation for growth velocity (2.15), increasing the

velocity relative to the base case with no additive present, must be caused by either a decrease in a_e or an increase in β. Since a_e is more likely to shift to higher values, it was concluded that an increase of β caused the enhanced kinetics[85]. For β to increase, there has to be either an increase in kink density n_k, or there has to be a decrease in the effective barrier of attachment to a kink, E_k. The former was ruled out because the velocity would become non-linear if n_k depended on supersaturation. Using this analysis, they evaluated the hydrophilicity of each of their molecules and concluded that molecules with greater hydrophilicity had a more pronounced effect on reducing the effective barrier of attachment to a kink and therefore increased the velocity[85]. The entropic and enthalpic components of the free energy change during crystallization reflect the water structuring at the crystal interface and also around the solute molecules in solution. Therefore, they concluded that the more hydrophilic molecules perturb the local water structure to a greater extent by facilitating the release of water molecules around the solutes and therefore their incorporation into the crystal surface[85].

The method by which step pinning affects the growth rate of specific crystal steps is by adsorption of additives to kink, edges, and terraces of a growing surface thereby hindering the movement of the growing steps. This phenomenon was described in a classic model of Cabrera and Vermilyea[89]. The basis of this model is the Gibbs-Thomson effect that relates differences in the free energy between step and solution to the curvature of the step, therefore greater curvature leads to a decreased number of nearest neighbors along a step edge, reducing the thermodynamic stability and increasing the excess step free energy[90]. This effect predicts a critical curvature r_c^{-1} that must be met in order for the excess step free energy to exceed the chemical potential difference between crystal

and solution ($\Delta\mu$). The steps cannot exceed this curvature set by the critical step radius r_c:

$$r_c = \frac{\alpha\omega}{k_B TS} \tag{2.17}$$

where, α is the step free energy per step height and ω is the molecular volume.

The Cabrera and Vermilyea model describes impurities adsorbing onto terraces between steps thereby pinning the step edge as it moves. When the average space between impurity molecules L_i is less than $2r_c$ the steps cannot advance creating a "dead zone" or region of positive supersaturation with out growth[90]. Since r_c depends on supersaturation, increasing supersaturation can result in the value of $2r_c$ being less than L_i and growth can resume. Weaver *et al.* used the Cabrera and Vermilyea model and updated the model to include an exact expression of the Gibbs-Thomson effect for all supersaturation values, a Langmuir model of adsorption dynamics, and an expression for the kink density (n_k) that considers poisoning of kinks[90]. In doing so, they were able to fit their experimental data of growth velocities of calcium oxalate monohydrate to their modified Cabrera and Vermilyea model, showing that step pinning is the dominant effect in this biomineral system.

By studying the effect of citrate on the formation of brushite, Tang *et al.* were able to conclude that the presence of citrate modified the step density of the brushite formation, not the step velocity as has been described before. Citrate was found to decrease the growth rate at moderate concentrations and inhibit crystal growth of brushite at higher concentrations[82]. The presence of citrate was found to increase the critical length needed for a dislocation to form a new step edge. Therefore, because the step

velocity was not altered, the terrace width became larger by decreasing the step density[82]. The only parameter that influences the critical step length was found to be the free energy of the step edge, γ_{step}. Therefore, addition of citrate increased the free energy of the step edge leading to longer induction times and a decrease in growth rate[82].

Peytcheva *et al.* were able to investigate the effects of various molecules on calcium phosphate by observing the dissolution instead of crystallization. The authors described this strategy as monitoring the "structural inversion of kinetics"[91]. Using poly (sodium) aspartate, bovine serum albumin, and poly-L-lysine, they showed that none of the polymers adsorbed onto the crystal surface. Therefore, they concluded via careful monitoring of the distinction between the molecules they observed (poly-L-Lysine is basic, poly (sodium) aspartate is acidic, and bovine serum albumin is both basic and acidic) that the observed acceleration of dissolution of specific crystal faces was due to accumulation close to the crystal surface. The surface accumulation controlled the dissolution of different sites with different selectivity effectively lowering the interfacial energy of specific crystal surfaces[91].

Another example of how incorporation of an impurity can effect the growth of a crystal was shown in an elegant study of Mg^{2+} and calcite growth. Davis *et al.* measured the velocities of step growth of calcite at different supersaturation levels and also in the presence of different concentrations of Mg^{2+}. They concluded that adding Mg^{2+} had the same effect as reducing the supersaturation of the solution. Therefore, they could identify incorporation as the cause of the crystal modification because as impurities become part of the crystal, strain is introduced in the solid lattice increasing the internal

free energy of the crystal, which then increases the crystal solubility decreasing the effective supersaturation of the growth solution[92].

Overall, there are many methods by which the growth of inorganic crystals can be affected by additives. These particular examples were selected to emphasize the methods used to characterize mechanism and also to highlight the limited number of mechanistic studies. The concepts presented can elucidate mechanisms for understanding the synthesis of inorganic material even when such detailed mechanisms are investigated indirectly, as is the case for many of the examples described in the templating section.

This chapter presents a summary of the different types of approaches that can be used to direct the growth of inorganic material using biomimetic molecules. In some cases, the biomimetic molecule serves as an organic matrix that can guide the growth of the inorganic material. In these cases the organic matrix can serve as an incarceration molecule, a framework that is then coated by the material, or a template molecule that guides the growth of inorganic material via specific interactions. In addition, the organic matrix can also promote the formation of higher order assemblies such as unitary nano-objects and extended nanostructures. In other cases, the organic molecules and the inorganic molecules co-organize to form hybrid materials via a dynamic process.

To form these hybrid materials and assemblies, the plethora of biomimetic molecules are discussed that use principles of self-assembly to organize and principles from crystal nucleation and growth to guide the formation of inorganic material. Understanding these processes and borrowing concepts from natural systems leads to the rational selection or design of biomimetic molecules that can guide the growth of a wide array of inorganic materials. The following chapters explore the use of a rationally

designed set of amphiphilic peptide molecules where the manipulation of molecular architecture allows us to understand both the organic assembly process and the synthesis of inorganic gold to form complex nanostructures.

Chapter 3

Self-Assembly of Rationally Designed Peptides Under Two-Dimensional Confinement

In this chapter we will discuss the self-assembly of rationally designed peptides at two-dimensional interfaces. This chapter highlights the role of electrostatics in the self-assembly of β-sheet forming peptides at the air-water interface. We characterize the phase behavior of a periodically sequenced sheet forming peptide by using Langmuir techniques, Brewster Angle Microscopy, Attenuated Total Reflection Fourier Transform Infrared Spectroscopy, and circular dichroism spectroscopy. We find that peptides with an alternating binary sequence transition at high pressures from discrete circular domains to fibrous domains. The qualitative behavior is independent of surface pressure but dependent on molecular areas. In addition, thermodynamic models are employed to specifically quantify differences in electrostatics by obtaining parameters for the critical aggregation area, limiting molecular area, and the dimensionless ratio of line tension to dipole density. Using these parameters, we are able to relate localized charge distribution to phase transitions, which will allow us to apply these molecules to examine how the dynamics of self-assembly can be directly coupled to the formation of composite nanostructures in biology.

3.1 Self-Assembly of Rationally Designed Peptides

Rationally designed biomimetic molecules that are capable of self-assembly into nanoscale morphologies have potential use in elucidating nature's capability to process materials with exquisite precision[30, 54, 93-96]. Peptide molecules that have the capability to self-organize at the air-water interface are particularly suited for mineralization studies because of their similarities to insoluble proteins used by nature[87] and their addressability in two dimensions. Peptides are also attractive because of the ability to iteratively control the nanoscale spatial distribution of chemical functionalities at the interface by manipulating amino acid sequences in a rational manner[31]. In contrast to previous work using polymers[97] and lipids[98] as the organic template in mineralization, peptides can be designed to assemble in particular secondary structures, namely, α-helices[99], parallel[100] or antiparallel[101] β-sheets[102], and β-hairpins [103]. Formation of secondary structures introduces additional levels of control in self-assembly processes via precisely positioned hydrophobic, electrostatic, and hydrogen-bonding interactions.

Several authors have applied rationally designed peptide sequences to interfaces to control the self-assembly of well-defined secondary structures in two dimensions. The Degrado lab has worked with simple peptides consisting of a 'binary code'. By applying a periodic sequence of only two amino acids (leucines and lysines), one can promote the formation of α-helices, β-sheets, or random coils[104]. With regards to β-sheet structures specifically, recent studies have adopted the importance of sequence by designing β-strands using alternating hydrophobic and hydrophilic amino acids, which can then

hydrogen bond with each other to from β-sheets. In addition, the Tirrell group has assembled β-sheets at the air-water interface and even induced long-range order in two-dimensions. This has been achieved by adding Proline residues at the termini of their sequences, which disrupts hydrogen-bonding interactions leading to order in the direction perpendicular to the peptide backbone[101]. Without these Proline residues long-range order is only achieved via hydrogen bonding in the direction of the peptide backbone[101]. Electrostatics has been shown to be a fundamental property of self-assembly in the bulk and at the air-water interface. Studies have shown that six residue peptides can form amyloid-like fibrils in bulk only when the net charge of the molecule is ± 1[105]. Other bulk studies have focused on electrostatics by using the same amino acids (E, A, and K) with different charge multiplets to show how a periodic β-sheet can adopt a β-hairpin structure depending on the charge distribution[106]. In two-dimensions, phospholipid tails have been attached to β-sheet forming peptides showing that the non-peptide tail increases the stability of the peptide at the interface and can even facilitate the creation of multilayers[102].

The advantage of using peptidic assemblies is apparent when applied to materials processing techniques such as templated nucleation of inorganic material. Previous work using polymer matrices, allowed for control over the nascent crystal properties to be achieved by varying concentration (which determines crystal size), varying ligands that attach to the polymer matrix (which determines crystal morphology), or varying the polymer matrix itself (which also controls crystal morphology)[97]. Similar work using fatty acids as the organic matrix determined that the chain length of a fatty acid also had an effect on the crystal morphology[98]. In addition, work with stearic acid as the template

determined that the degree of compression of the monolayer induced homogeneity of one polymorph of the resulting calcium carbonate crystals. Mann *et al.* attributed this preference for vaterite upon compression to the decreased mobility of the organic-template[107]. Using lipopeptide molecules Cavalli *et al.* were able to template indented calcium carbonate crystals because of the ability of the lipopeptide to deform at the interface. They also attributed the nucleation of different faces of the crystal to the alignment of the lipopeptides in one direction, reorganizing the functional groups along the crystalline axis[54]. Thus the advantage of rationally designed peptide-based assemblies lies in the diversity of functional groups that can be introduced to the air-water interface without using entirely different materials, as is the case for polymers and fatty acids. In addition peptide monolayers can also be compressed to achieve limited mobility and rearrangement of these diverse functional groups.

This work involves four peptide molecules that are rationally designed to form β-sheets at the air-water interface. The molecules are designed using two simple heuristics for the rational design of sheet forming amphiphilic peptides.

3.1.1 Peptide Design

First, we select amino acids that have the greatest propensity to form β-sheets, according to the particular ϕ and ψ angles preferred for each side group[108]. The value ϕ is a torsional angle between the α-carbon and the amine, while ψ is between the α-carbon and the carbonyl group in a peptide or protein molecule. Different amino acids have different preferred ϕ and ψ angles because of steric hindrance and therefore have a preference towards a particular secondary structure.

Second, we apply the binary sequence periodicity associated with β-sheets, using sequences with alternating hydrophobic and hydrophilic residues[104, 109].

All four sequences contain 17 amino acids and are composed of valines, glutamines, glutamic acids, histidines and tryptophans, figure 1. Beta 9 and Beta 3, have the same type and number of each amino acid. They also have the same overall charge but a different charge distribution. Beta 3 has two glutamic acids separated by three amino acids (~ 1.4 nm), while Beta 9 has two glutamic acids separated by 9 amino acids (~ 3.5 nm). Beta 3H and Beta 9H are identical to Beta 3 and Beta 9, except the negatively charged glutamic acids are replaced with histidines, which have pH dependent charges. By designing peptides to have a different charge distribution, we attempt to illustrate the effect that electrostatics has on the cooperative assembly process. On the other hand, all four molecules have similar hydrogen bonding capabilities that would favor self-assembly in the plane of the air-water interface. A schematic of the peptides is shown in figure 3.1.

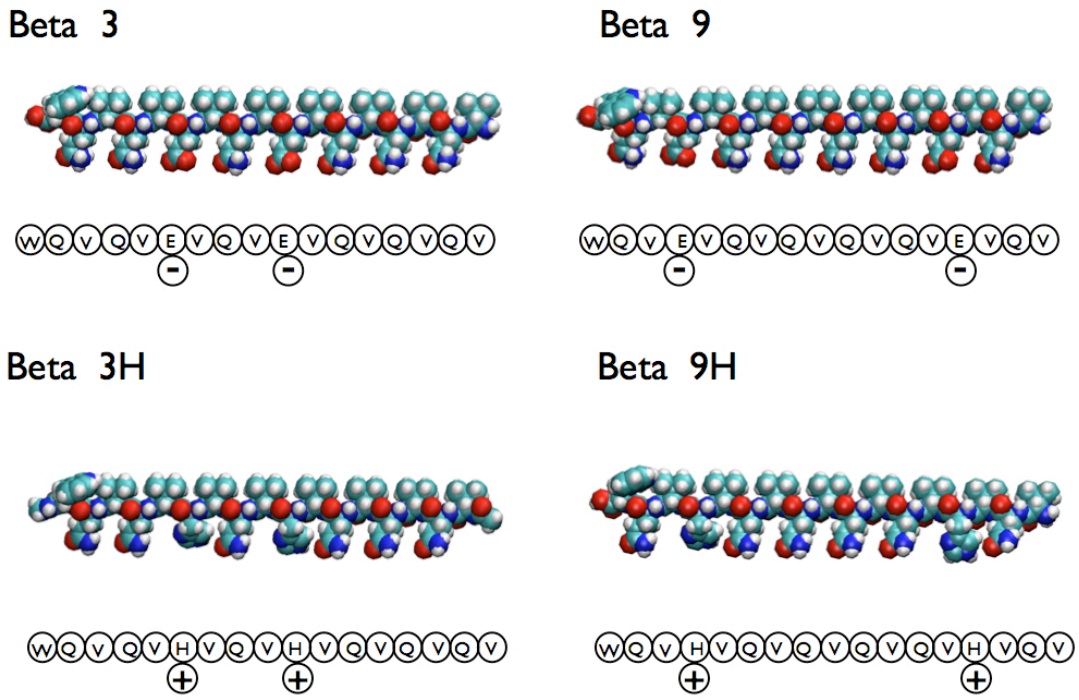

Figure 3.1- Rationally Designed Peptide Molecules. The four peptide molecules rendered using Van der Waals representation: (a) Beta 3 (b) Beta 9 (c) Beta 3H and (d) Beta 9H.

3.1.2 Peptide Synthesis

The peptides designed above are synthesized using (F)luorenyl-(m)eth(o)xy-(c)arbonyl chemistry, more commonly known as "FMOC"chemistry. This precise technique allows the peptide to be formed by adding one amino acid at a time. The synthesis is perfromed on small solid (~10 μm) polystyrene beads that are insoluble yet porous. The technique involves using protecting groups on the amine terminus to ensure that the amino acids are not polymerized during the reaction. To begin the synthesis a protected amino acid containing an Fmoc group is reacted with the polystyrene resin.

The Fmoc group is then removed from the amine-(N)-terminus in order to allow it to react with another amino acid that is protected by another Fmoc group, allowing for only one condensation reaction to occur. This deprotection and coupling is repeated until the exact amino acid sequence desired is obtained. At this stage the final deprotection is performed and then the peptide is cleaved from the resin using trifluoroacetic acid. An illustration of this mechanism is show in the figure below.

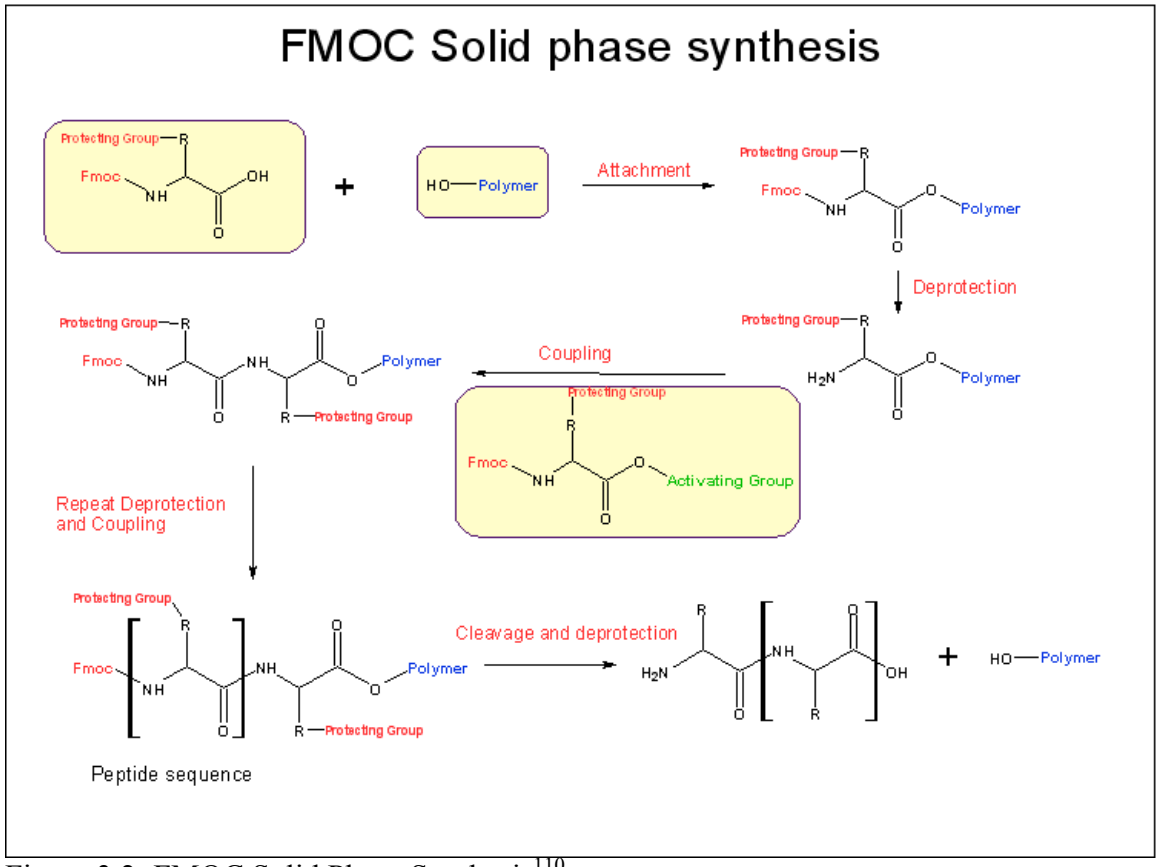

Figure 3.2: FMOC Solid Phase Synthesis[110]

The peptide molecules are characterized using Langmuir monolayer experiments, Brewster Angle Microscopy, circular dichroism and Attenuated Total Reflectance Fourier Transform Infrared (ATR-FTIR) spectroscopy. The Langmuir trough confirms the surface activity of the molecules and shows their phase behavior by forcing them from a two-dimensional gaseous to solid phase. Using Brewster Angle Microscopy in

conjunction with the Langmuir trough we are able to visualize phase behavior as a function of surface pressure. Using circular dichroism and ATR-FTIR spectroscopy, we probe β-sheet formation at the air/water interface. These techniques together with a careful thermodynamic analysis allow us to quantify the role that electrostatics play during the self-assembly process in two dimensions. The molecules used in this work are selected as simplistic model molecules that can couple two known pathways for materials synthesis, self-assembly and nucleation and growth, leading to new methods for processing of hybrid materials that possess tailored architectures at hierarchical length scales[32, 54, 111].

3.2 Experimental Details

3.2.1 Materials

Peptide molecules are synthesized by AnaSpec (San Jose, CA), and all have a purity of over 80%. The peptides are stored at -20 ºC. Monolayers of the peptide molecules are prepared by spreading a fresh solution of the peptide in trifluoroacetic acid/chloroform (1:9 v/v) at a concentration of 1mg/mL. Both trifluoroacetic acid, Nochromix crystals (GODAX Labs), sulfuric acid (95-98%), and chloroform are obtained from Fisher Scientific (Pittsburgh, PA), and water is purified using a Millipore apparatus. Octadecyltrichlorosilane is obtained from Acros Organics a division of Thermo Fisher Scientific.

3.2.2 Langmuir Trough

Surface Pressure-Area isotherms are obtained using a KSV minimicro trough (KSV instruments, Helsinki, Finland). The molecules are deposited on a subphase of

deionized water and are all compressed at the same speed of 5mm/min. Monolayers of the films are transferred using vertical deposition on a KSV 5000 trough (KSV instruments, Helsinki, Finland) to substrates that are hydrophobically modified using Octadecyltrichlorosilane. We believe that the peptides were successfully transferred to the substrates because we obtained transfer ratios of approximately 1. The hydrophobic modification of the substrates with Octadecyltrichlorosilane was also performed using vertical deposition on a KSV 5000 trough. The procedure is discussed in detail by Kumar *et al.*[112] Substrates were cleaned before use by sonication in Nochromix solution for 30 min followed by sonication in deionized water for another 30 min.[112] The Nochromix solution was prepared by dissolving the Nochromix crystals in sulfuric acid until the solution becomes transparent. [112]

3.2.3 Brewster Angle Microscopy

Brewster Angle Microscopy images are obtained simultaneously with the surface pressure-area isotherms using an I-Elli 2000 ellipsometer/ Brewster Angle microscope from Nanofilm a division of Halcyonics Gmbh (Goettingen, Germany). The resolution of the I-Elli 2000 is 1 micron in all images shown.

3.2.4 ATR-FTIR Spectroscopy

For ATR-FTIR spectroscopy experiments, monolayers are deposited on 45° ATR Si prisms that have dimensions 50mm x 10mm x 3mm, which are hydrophobically modified using Octadecyltrichlorosilane (OTS). All substrates have contact angles greater than 90° before deposition of the peptide monolayer. The FTIR spectra are collected using a BioRad FTS 175 FTIR spectrometer, configured with a horizontal ATR apparatus

using a liquid nitrogen cooled mercury-cadmium-telluride (MCT) detector. The dark count for the detector is 1 x 10^{-5} a.u., which is well below the integrated absorbance of the smallest peak we are considering at the lowest peptide concentration (8.775 x 10-4 a.u. for the 1701 wavenumber peak of the 5mN/m spectra in figure 4). Before obtaining the FTIR spectra of the peptide molecules, a spectra of OTS on the ATR crystal is obtained to be used as a background during the peptide spectra measurements. To verify the integrity of the peptide layer transferred to the ATR crystal, images were obtained of the peptide on a silicon substrate that was hydrophobically modified with OTS using the Brewster Angle Microscope. The images show similar features as the images taken at the air/water interface. (data not shown)

3.2.5 Circular Dichroism Spectroscopy

For circular dichroism experiments, monolayers are deposited on quartz disks that are hydrophobically modified using OTS. All substrates have a contact angles greater than 90° before deposition of the peptide monolayer. The circular dichroism spectra are collected using an Olis DSM 20 Spectrophotometer. This signal to noise ratio of the data obtained was 4 at the lowest peptide concentration and 5 at the highest peptide concentration. To verify the integrity of the peptide layer transferred to the quartz disk, images were obtained of the peptide on a quartz disk that was hydrophobically modified with OTS using the Brewster Angle Microscope. The images show similar features as the images taken at the air/water interface. (data not shown)

3.3 Results & Discussion

3.3.1 Critical Aggregation Area

Figure 3.3 shows the Langmuir isotherms for Beta 3, Beta 3H, Beta 9, and Beta 9H. Qualitatively, a steep liquid condensed region and a liquid expanded to liquid condensed transition occurs at very low surface pressures for all four molecules. In deionized water, both Beta 3 and Beta 9 are negatively charged, while Beta 3H and Beta 9H are neutral. This influence of charge can be seen clearly in figure 3.3 where the pressure for both the Beta 3 and the Beta 9 peptides begins to increase at much higher areas compared to Beta 3H and Beta 9H.

It is also interesting to note the difference between Beta 3 and Beta 9. Beta 9 experiences intermolecular interactions at larger areas then the Beta 3 analogue. We attribute this phenomenon to the charge spacing, where more localized charges in the Beta 3 molecules allow them to arrange more compactly in a staggered fashion compared to the Beta 9 molecule where the charges are more evenly distributed. The equivalent phenomenon exists in the histidine peptides, suggesting a similar repulsion with a weaker positive charge. The outcome of these differences is quantified and visualized in subsequent sections.

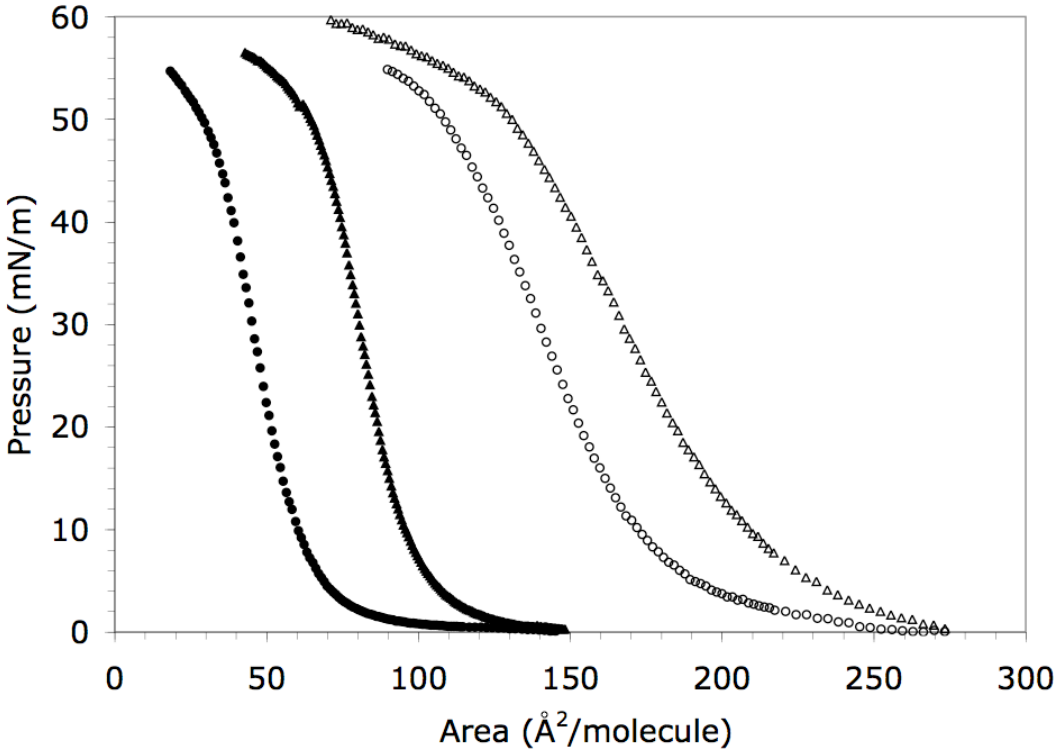

Figure 3.3: Pressure/Area Isotherms of the Peptide Molecules. The isotherms were collected at 25°C on a deionized water subphase (pH~ 5.5) for each of the peptide molecules: Beta 9 open triangle, Beta 3 open circle, Beta 9H filled triangle, and Beta 3H filled circle.

In addition to single compressions, experiments have been performed using the Langmuir trough for compression and expansion cycles. The peptides exhibit a large degree of hysteresis when comparing the compression isotherm to the expansion isotherm. We believe this hysteresis is due to the irreversible nature of assemblies that are hydrogen bonded as observed by groups studying β-sheet assemblies at the air/water interface[113-115]. We will discuss this behavior in the subsequent chapter.

To evaluate the behavior of all four peptide molecules, their pressure/area isotherms have been quantified in terms of an equation of state. Fainerman and coworkers

have developed an equation that includes aggregation in two-dimensions at moderate surface pressures[116] and extends this analysis to include interactions between molecules within an aggregate[117, 118]. Fainerman's analysis is derived by extending two-dimensional equations of state of gaseous monolayers, known as the Volmer equation, and includes aggregation using the chemical potential for monomers and aggregates, Butler's equation [116]. We apply Colfer and Power's equation, which is an extension of Fainerman's analysis that uses relative instead of absolute surface pressure, in the analysis of our molecules[103]. For example, the relative equation of state for the Beta 9H molecule is:

$$\Pi - \Pi_{A=197} = \Pi_{rel} = \left\{ \frac{RT}{\left[(A - A_0)(A_C / A) \right]} \right\} - \left\{ \frac{RT}{\left[((197 - A_0)(A_C / 197) \right]} \right\} \qquad (3.1)$$

The same equation was used for Beta 9, Beta 3H, and Beta 3 except for the reference area. The reference area was chosen by using the smallest area that allowed the surface pressure to remain at zero upon the addition of the peptide to the interface. The reference area was 197 $Å^2$/molecule for Beta 3H and Beta 9H. For Beta 3 and Beta 9 the reference area was 489 $Å^2$/molecule.

By fitting the data from the Langmuir isotherms in figure 3.2 to equation 1, one is able to obtain the parameters A_0 and A_C. A_C is the critical aggregation area, which is analogous to the inverse of the three dimensional critical micelle concentration. This implies that above A_C no aggregates are present, but below A_C large aggregates are present[103]. The term A_0 is described as the limiting molecular area or the area actually occupied by the molecule in the monolayer.

Table 3.1 Values of A_0, A_C, and λ/μ^2 for all four peptide molecules and the parameters obtained from the image analysis to find λ/μ^2 .

	Beta 9	Beta 3	Beta 9H	Beta 3H
A_0 (Å^2/molecule)	250.24	158.53	74.46	54.93
A_C (Å^2/molecule)	617.61	1121.46	402.14	398.22
w (μm)	0.978	1.129	1.001	0.900
Φ_v	0.133	0.172	0.092	0.078
δ(Å)	2.615	2.143	1.289	0.554
λ/μ^2	6.504	6.826	7.258	7.987

Table 3.1 has both values for each molecule. Comparing the A_0 values obtained, the histidine containing peptides are smaller than the glutamic acid containing peptides. Additionally, in both the glutamic acid containing peptides and the histidine containing peptides, the Beta 3 versions are smaller than Beta 9 versions. We also show that the A_C values for the glutamic acid containing peptides are much larger than that of the histidine containing peptides. This result is non-intuitive, indicating that cohesive forces between the glutamic acid containing peptides are greater than the cohesive forces for the histidine containing peptides. However, the cohesive forces in the form of hydrogen bond formation should be similar for each molecule. We believe that the reason the glutamic acid containing molecules aggregate at lower surface concentrations is that the long-range electrostatic repulsion between the molecules forces the molecules to distribute more regularly throughout the interface. On compression, this leads to the local formation of a greater number of smaller aggregates. Experiments conducted with

various salt concentrations in the subphase support the hypothesis and are discussed in subsequent paragraphs.

The value of A_C for Beta 3H and Beta 9H are equivalent, indicating that aggregation occurs at the same area for both molecules. However, in the glutamic acid containing peptides, there is a more pronounced difference between the A_C of Beta 3 and Beta 9. Beta 9 has a lower A_C value than Beta 3. This again seems counterintuitive. At first glance one would expect that since Beta 9 possesses an A_0 value that is higher than the A_0 of Beta 3, then Beta 9 would subsequently aggregate at a larger area. However, A_C is a measure of cohesive intermolecular forces and not electrostatic repulsion. Therefore, Beta 3 with its centrally localized charge allows for hydrogen bonding with other peptide molecules at the uncharged end of the molecule. This staggered arrangement of peptides could lead to self-assembly at lower interfacial concentrations. In contrast, Beta 9 displays its negative charge across the entire molecule and thus hydrogen bonding between these molecules would only occur after the electrostatic repulsion of the entire molecule is overcome. It is interesting to note that the histidine molecules do not show this A_C trend. We believe that the weaker charge in these molecules makes this effect negligible.

Langmuir trough experiments were also carried out on subphases that have different concentrations of monovalent salts. Figure 3.4 shows that by increasing NaCl concentration in the subphase of the Beta 3 isotherms, the curves shift to the left. This is indicative of the negative charges on the glutamic acid residues being screened and thus behaving more like their less charged counterpart Beta 3H. This is in agreement with Guoy-Chapman theory[119, 120], which states that an increase in electrolyte in the subphase

should increase charge screening. Similar behavior can be seen with the Beta 9 molecule (data not shown). Another way to tune the electrostatic behavior of these molecules is by varying the pH of the subphase. Additional experiments were performed on Beta 3H in which the deionized water was replaced by a pH 2 solution. The data is shown in figure 3.5.

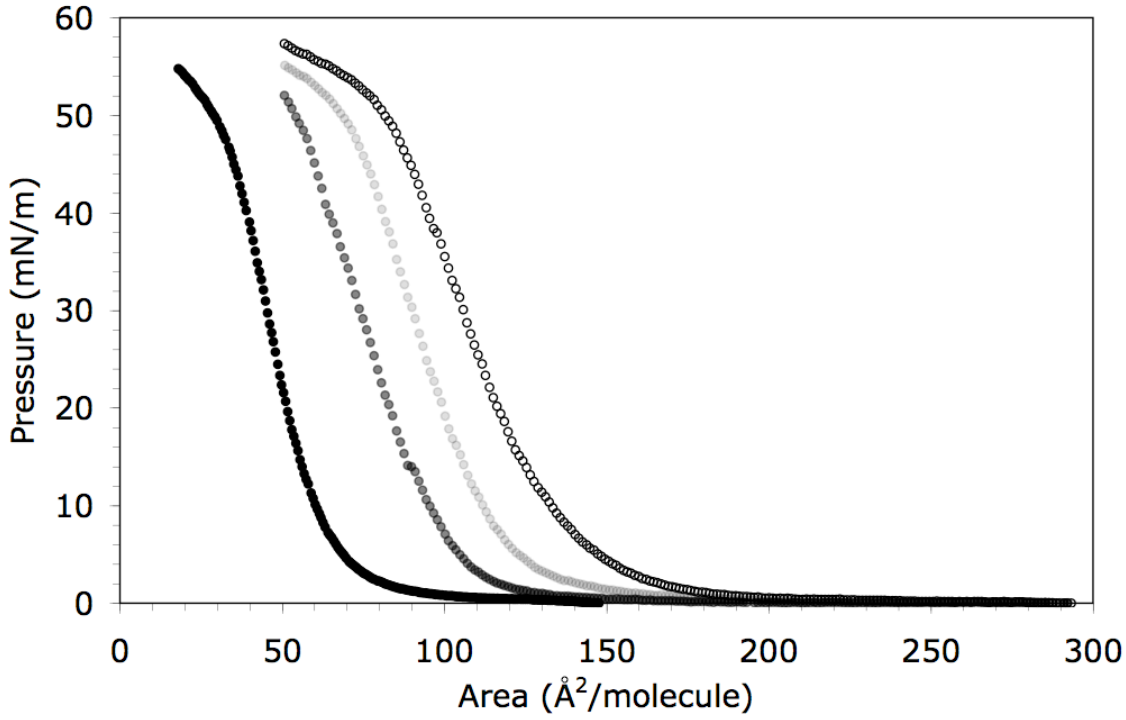

Figure 3.4: Pressure/Area Isotherms of Beta 3 and Beta 3H with Monovalent Salt. The isotherms were collected at 25°C on a deionized water subphase (pH~ 5.5) for Beta 3 (open circles) and Beta 3H (black circles). Isotherms were also collected for Beta 3 with a subphase of 50 mM NaCl (light gray circles) and 500 mM NaCl (dark gray circles).

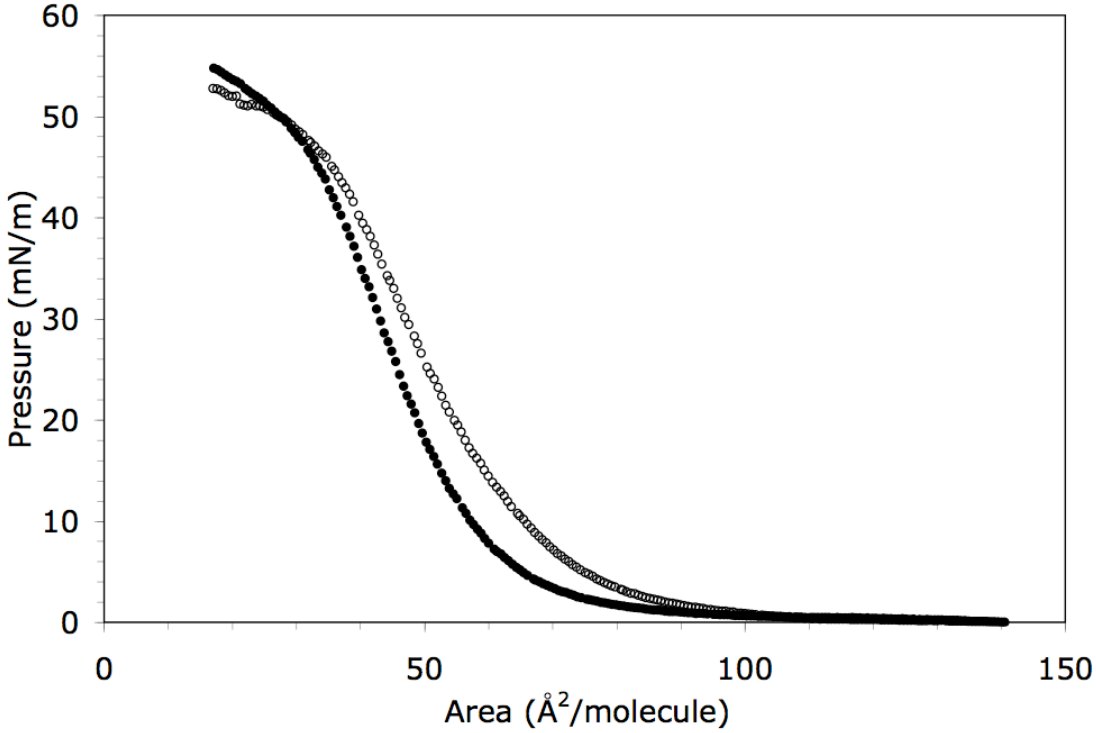

Figure 3.5: Pressure/Area Isotherms of the Beta 3H. The isotherms were collected at 25°C on a deionized water subphase (pH~ 5.5) and a hydrochloric acid subphase (pH~2.0). The water isotherm is the filled circles and the hydrochloric acid subphase is the open circles.

Table 3.2 Values of A_0 and A_C for Beta 3 and Beta 3H on a deionized water subphase and Beta 3 on a subphase of 50 mM NaCl and 500 mM NaCl.

	Beta 3	Beta 3	Beta 3	Beta 3H
Subphase	Water	50 mM NaCl	500 mM NaCl	Water
A_0 (Å^2/molecule)	158.53	110.56	92.95	54.93
A_C (Å^2/molecule)	1121.46	653.35	636.39	398.22

In Table 3.2, one can see the A_0 and A_C values obtained when fitting the experiments shown in figure 3.4 to the model used by Colfer and Powers.[103] This allows

us to quantify the effect that a decreasing Debye length has on these molecules. As expected, the A_0 value for the Beta 3 molecule decreases with increasing salt concentration. This indicates that the effective size of the molecule decreases as its charges are screened. The same decreasing trend follows for A_C. It is interesting to compare the A_C values for Beta 3 on a subphase of deionized water with Beta 3 on a subphase of 50mM NaCl. The value indicates a sharp decrease in the area per molecule needed for the molecules to aggregate. This phenomenon can be explained by similar reasoning to the overall difference between the glutamic acid peptides and the histidine peptides. The A_C value for Beta 3 in a 50 mM NaCl subphase and a 500 mM subphase is similar, indicating the double layer formed, that screens the negatively charged glutamic acid residues, is close to complete at the lower concentration of NaCl.

3.3.2 Secondary Structure

Using ATR-FTIR and circular dichroism, the secondary structure for the peptide molecules is evaluated. Both techniques indicated that the peptides are in a β-sheet confirmation at high pressures. The ATR-FTIR spectra are shown in figure 3.6. On increasing the surface pressure of the film from 5mN/m to 25mN/m, a more pronounced intermolecular weak sheet peak at 1701 cm^{-1} is observed[121]. On increasing the surface pressure to 50 mN/m, the weak sheet peak is diminished, and a peak indicative of a strong sheet is observed at 1630 cm^{-1} [121]. In addition to the β-sheet peaks, there is a peak present at 1655 cm^{-1} at all three pressures that is normally assigned to a random coil[121]. At 5mN/m, this peak is barely observed and it becomes more pronounced at 25mN/m. We believe that the small peak at low pressures is due to a heterogeneous layer being

present when transferring the peptide at low pressures. At 50 mN/m this random coil peak is slightly smaller than at 25mN/m. We believe that this diminished peak is due to a greater β-sheet content in the more compressed state. The data obtained using circular dichroism followed the same trend and can be seen in figure 3.7. At low concentrations a peak minimum indicative of a β-sheet confirmation is not evident. However, at high pressure or greater peptide concentration, it is evident that there is a minimum around 217 nm. This is in agreement with reported values for a beta sheet structures[122]. The spectra obtained for Beta 9, Beta 9H and Beta 3 show a similar trend. (data not shown)

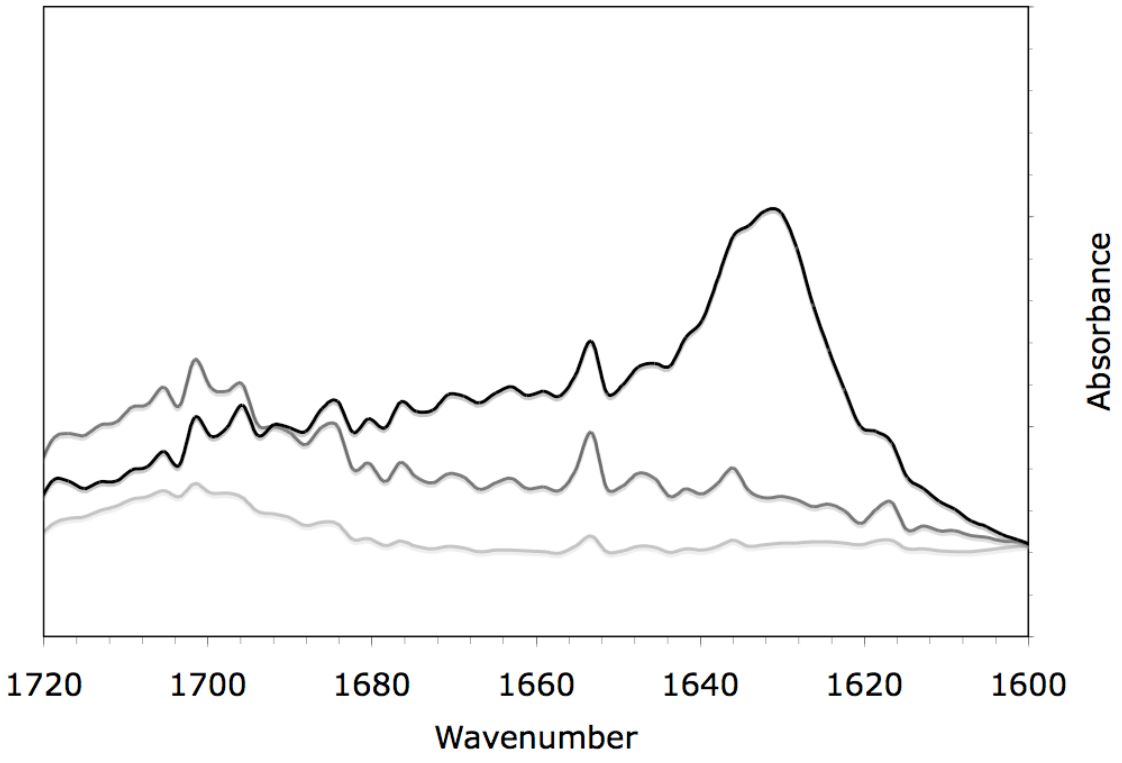

Figure 3.6: ATR-FTIR Spectra Confirming the Presence of a β-Sheet Secondary Structure. ATR FTIR Spectra of the Beta 3H molecule was collected at varying surface pressures. The black line is 50mN/m, grey line is 25mN/m, and light grey line is 5mN/m.

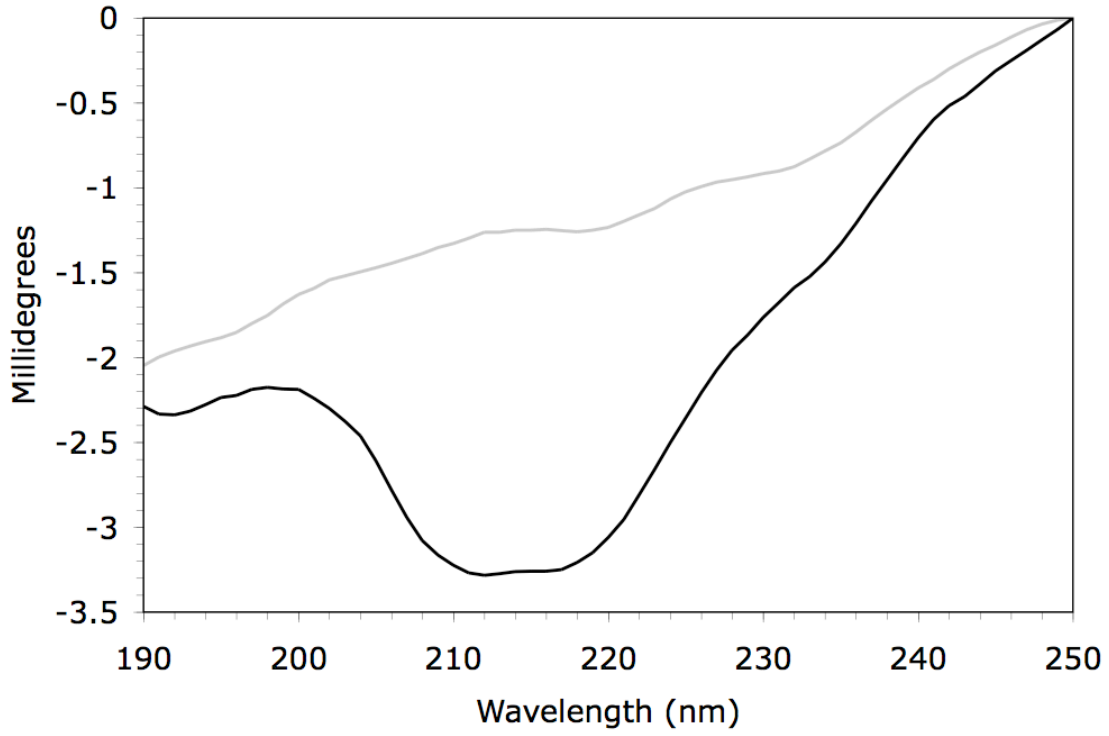

Figure 3.7: Circular Dichroism Spectra Confirming the Presence of a β-Sheet Secondary Structure. Circular Dichroism Spectra of the Beta 3H molecule at a surface pressure of 5mN/m (gray line) and 50mN/m (black line).

3.3.3 Phase Behavior

Brewster Angle microscopy allows us to visualize the phase behavior of the peptide monolayers with the added benefit of not having to use external probes which are needed in other techniques such as fluorescence microscopy[123]. For all four peptides, one observes the emergence of circular domains between the surface pressures of 10-30 mN/m. The circular domains appear small in the image, and they tend to form a cloudy phase that occupies the entire field of view.

As the surface pressure continues to increase, there is a transition from circular domains to fibrous domains. This transition occurs between 30-50mN/m with fibers being fully formed usually at 50mN/m. Images of the fibers for each of the molecules can be seen in figure 3.8. The fibers emerge at the same surface pressure for all four molecules, which corresponds to different molecular areas as seen in figure 3.2. The fibers appear at the largest areas for Beta 9 and the smallest for Beta 3H. We also observed that the emergence of holes within the fibers occurs only in the histidine containing molecules Beta 3H and Beta 9H, an example of which is shown in figure 3.8 d.

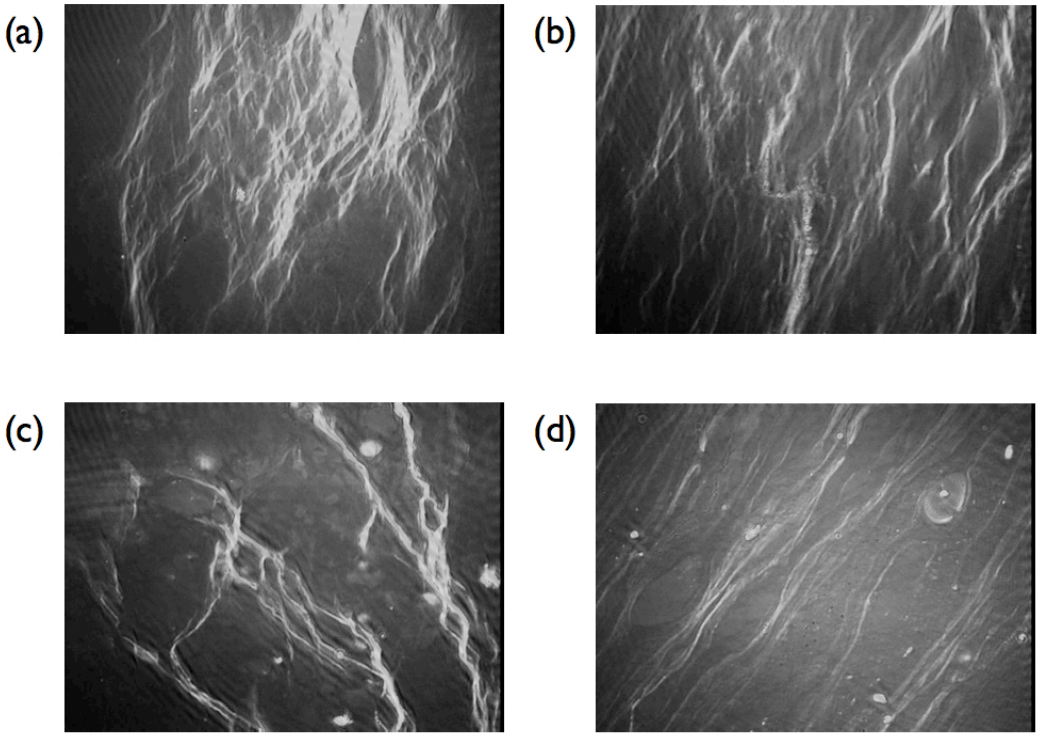

Figure 3.8: Brewster Angle Microscopy Images of the Peptide Molecules Assembled into Fibers. The images were all taken at a surface pressure of 50mN/m and have a width of 220 microns. Beta 9 (a), Beta 3 (b), Beta 9H (c), and Beta 3H (d).

Additionally, for glutamic acid containing peptides, there is no phase coexistence region between the circular and fibrous transition, but coexistence has been observed for the histidine containing peptides. We attribute this phenomenon to the difference in electrostatics between the molecules since fiber formation should occur when the electrostatic contribution to the free energy overcomes the line tension contribution[124]. To evaluate the Brewster Angle Microscopy images, we use McConnell and coworkers' theory for stripe phases occurring in monolayers[125-127]. Their model balances the free energy contributions of line tension between domains and electrostatic interactions of the domains. They begin with the following equations:

$$F = \lambda p + F_{el} \tag{3.2}$$

$$F_{el} = const - \frac{\mu^2}{2} \oint\oint \frac{1}{r} d\vec{l} d\vec{l}' \tag{3.3}$$

In these equations, F is the free energy, λ is line tension, F_{ell} is the electrostatic free energy, and μ is the difference in dipole density between the fluid and the solid phase. Using equation 3.2 one can explain why circular domains are observed during the compression of the molecules. At the lower pressures line tension dominates the free energy of the system yielding circular domains. At higher pressures there is a transition to a stripe phase for all four molecules, indicating that the electrostatic interactions are dominating the free energy. This same type of analysis explains why holes are observed in only the histidine containing molecules since areas with little or no molecules present would occur to reduce the line tension between domains[128, 129]. By performing the integration in equation 3.3, one arrives at the following equation defining the formation of the stripe phase:

$$\overline{F_s} = 2\mu^2\left(\frac{\phi_v}{w}\right)\left\{\frac{\lambda}{\mu^2} - \ln\left[\frac{w}{2\delta}\right]\cdot\frac{\sin(\pi\phi_v)}{\pi\phi_v}\right\} \tag{3.4}$$

ϕ_v is the solid area fraction, w is the width of the stripes, and δ is the interdipole distance. If one minimizes this equation with respect to w, one obtains:

$$w = \frac{2\delta\pi e}{\sin(\pi\phi_v)}e^{\frac{\lambda}{\mu^2}} \tag{3.5}$$

From our Brewster angle microscopy images, we can obtain values for w and ϕ_v. These values are obtained by using image analysis software to determine the exact location of the fibers and calculate both the width of the fibers and the fractional area occupied. The value for δ is obtained by using the molecular area obtained from the Langmuir trough experiments at a pressure of 50 mN/m and then dividing this value by the theoretical length of these molecules, 5.0 nm. Therefore the δ value would be largest for Beta 9 and smallest for Beta 3H, since Beta 3H packs more tightly than the other molecules.

Rearranging equation 3.5, one obtains equation 3.6:

$$\frac{\lambda}{\mu^2} = \ln\left(\frac{w\sin(\pi\phi_v)}{2\delta\pi\phi_v e}\right) \tag{3.6}$$

which gives the ratio of the line tension over the dipole density. The qualitative behavior for all four peptides is similar, showing that the binary sequence periodicity dominates interfacial self-assembly, but this dimensionless parameter gives us the ability to quantitatively discern the influence of electrostatics on aggregate formation sequences in terms of the forces that are dominating the free energy. Higher values of this number would indicate that line tension between boundaries is higher than electrostatic contributions to the free energy. The values for our four peptides appear in table 3.1.

When we compare the values obtained, it is evident that the results are in agreement with the Langmuir trough data. The molecules with the greatest electrostatics or smallest λ/μ^2, are the Beta 9 molecules, followed by Beta 3, Beta 9H, and then Beta 3H. When we compare the values of the histidine set to the glutamic acid set, we see that the numbers are larger for the histidine set. Comparing Beta 3 and Beta 9 in both sets of molecules also gives us greater λ/μ^2 numbers for Beta 3 as compared to Beta 9, which again supports the notion that the more localized charge in the Beta 3 molecules allows the peptides to pack more efficiently and would therefore appear to have weaker electrostatics.

3.4 Summary

Natural systems show an unparalleled ability to assemble composite materials across hierarchical length scales. At the heart of this materials processing phenomenon is the ability to control self-assembly pathways. Our peptides are particularly suited to serve as an organic template capable of rearrangement into particular patterns that define mesoscale structures. We have characterized four simple rationally designed peptide molecules using tools that allow us to quantify the phase behavior and intermolecular interactions. In addition, we have applied a thermodynamic analysis for periodically sequenced peptides, resulting in a more lucid understanding of self-assembly under confinement. These tools confirm that all four variations of our peptide are surface active, form beta sheets at the air-water interface, and form fibrillar domains at high surface concentrations when hydrogen bonding between the molecules dominates the free energy. Interestingly, we observe that charge leads to the formation of distributed aggregates at lower surface concentrations as spatially localized charge influences the

packing of peptides at the interface. This analysis allows us to now explore the non-equilibrium cooperative relationship between self-assembly and composite biomaterials processing.

Chapter 4

The Relation Between Network Formation and Irreversibility in Two-Dimensional Systems

In this chapter the relationship between network formation and irreversibility is discussed. The self-assembly of sheet-like structures is responsible for the unique physical properties in several natural systems and biologically inspired synthetic materials. The work described here investigates the irreversibility of the same molecules discussed in the previous chapter. Using Brewster angle microscopy and Langmuir trough experiments, we show that the irreversible behavior of our designed peptide system is analogous to the assemblies of amyloid, spidroin, and silk fibroin. The irreversibility of these systems is attributed to the formation of a β-sheet network of fibrous aggregates. By analyzing the development of hysteresis in the compression and expansion isotherms using a Langmuir trough, we are able to show that differences in electrostatic interactions affect the extent of network formation. Additionally, we connect the formation of macroscopic order and the thermodynamics of irreversibility in addressable confined networks.

4.1 Irreversibility in Natural Systems

Natural materials such as silk from spiders and silkworms have exceptional material properties that are derived from the formation of microscopic β-sheets[130, 131]. For example, spiders produce silk using soluble proteins that transform into insoluble silk fibers that possess a modulus of up to 15 GPa[132]. The dynamics of the structural transition of the protein spidroin, involved in the production of spider silk, is also of medical interest as the formation of insoluble sheet-like structures has been found to have both sequence and structural similarities to the amyloid family of proteins. Specifically, the amyloid β-peptide is believed to produce senile plaques made up of extracellular fibers. The link between these three different fiber-forming proteins is the high content of β-sheet secondary structure. For this reason, rationally designed peptides are attractive molecules to investigate material properties and self-assembly because they can be designed to have a particular secondary structure (α-helices[99], parallel[133] or antiparallel[101] β-sheets, and β-hairpins[103]) that can be tuned by stimuli. Moreover, monolayers of peptide molecules at the air-water interface can be used as model systems, where the orientation and intermolecular interactions of a two dimensionally confined system can be precisely observed. This work investigates the nature of fibrous aggregates by making iterative changes in the peptide sequence that favor or disfavor the self-assembly and reversibility of the self-assembly of confined amphiphilic peptides.

The work described in this chapter uses the same molecules as a model system as chapter 3: Beta 3, Beta 3H, Beta 9 and Beta 9H. In the previous chapter, we described the behavior of these peptide molecules in detail by highlighting the effect of

electrostatics on self-assembly.[134] Here we focus on the irreversibility of these assemblies in terms of the hysteresis observed during compression/expansion Langmuir isotherms.

The characterization of the peptides is achieved using Langmuir monolayer experiments and Brewster Angle Microscopy. The Langmuir trough confirms the surface activity of the molecules and shows their phase behavior by forcing them from a gaseous to a solid state. Using Brewster Angle Microscopy in parallel with the Langmuir trough enables us to visualize phase behavior as a function of surface pressure. These two techniques allow us to show that the formation of a β-sheet network at the air/water interface is causing the irreversibility on compression and expansion. Moreover, we observe that the formation of the aggregate structure can be tuned by manipulating the electrostatic interactions of the molecules, where a decrease in electrostatic repulsion leads to a greater extent of β-sheet network formation and, therefore, a greater degree of irreversibility.

4.2 Results and Discussion

In the previous chapter, we analyzed the behavior of the four peptide molecule single compression isotherms using thermodynamic models to obtain quantifiable parameters to compare the sequences. We find that molecules that have a more localized charge distribution are able to pack tighter in their aggregated state[134]. Here we discuss compression and expansion experiments performed using the LB trough. In figure 4.1, one can see the compression and expansion isocycles pertaining to the Beta 3 molecule. The experiment is performed by placing an amount of peptide on the surface and in the first cycle compressing to a given area and then expanding back to the full area of the trough. In the second cycle, the peptide is compressed to a pressure of 46 mN/m to a

smaller area and then fully expanded. In the third cycle, the peptide is compressed to a pressure of 58 mN/m and then fully expanded. Even when the peptide is compressed to the largest area, hysteresis is observed between the compression and expansion cycles.

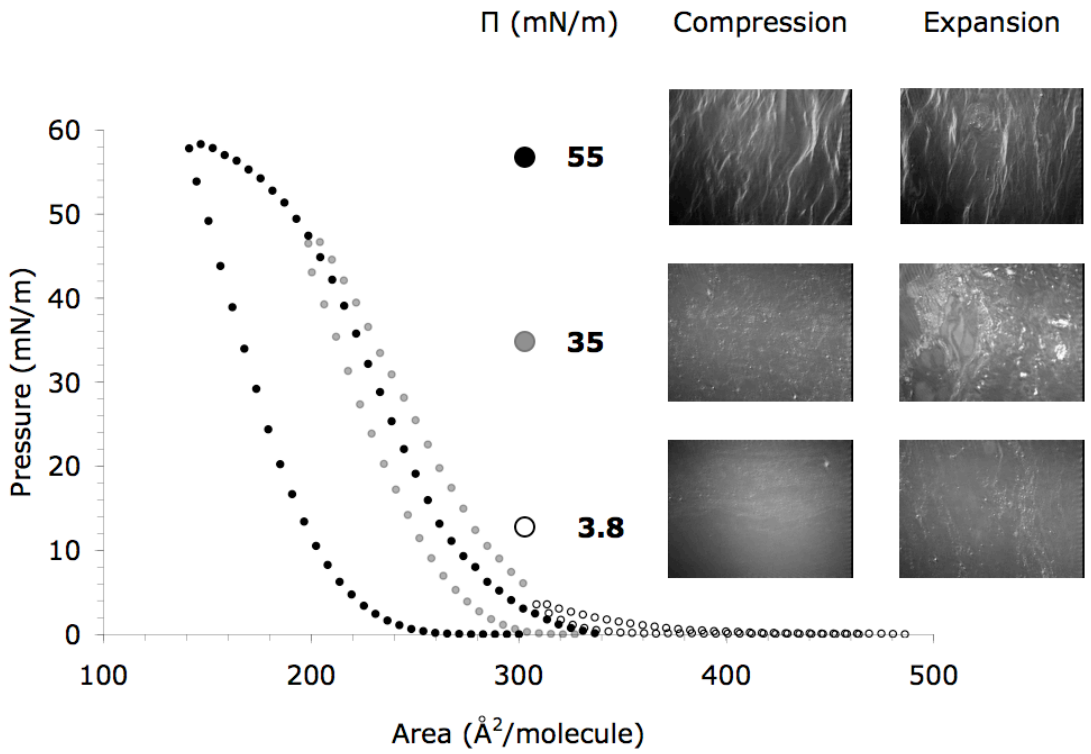

Figure 4.1: Compression and expansion isocycles of the Beta 3 molecule at 25º C. The open circles are for the isotherm compressed to 311 $Å^2$/molecule. The gray circles are for the isotherm compressed to 199 $Å^2$/molecule. The black circles are for the isotherm compressed to 143 $Å^2$/molecule. Brewster angle microscopy images taken during compression and expansion are shown on the right at their corresponding surface pressure. The width of each image is 220 μm.

Hysteresis in LB isotherms has been attributed to several phenomena. First, hysteresis has been attributed to molecules being forced into the subphase because of the lateral forces being exerted on the monolayer[135]. Second, hysteresis has been attributed to a relaxation phenomenon in which the time for the monolayer to relax after

compression is longer than the length of the experiment. This has also been observed in the mechanics of the coil stretch transition of flexible polymers[136]. To show that relaxation is not the cause of the hysteresis in our experiments, we have also performed the same compression expansion experiment at a much slower speed of compression and expansion, which is shown in figure 4.2. We find that the hysteresis between compression and expansion is still significant. Thus, in our case, we believe that the hysteresis is not due to relaxation phenomena.

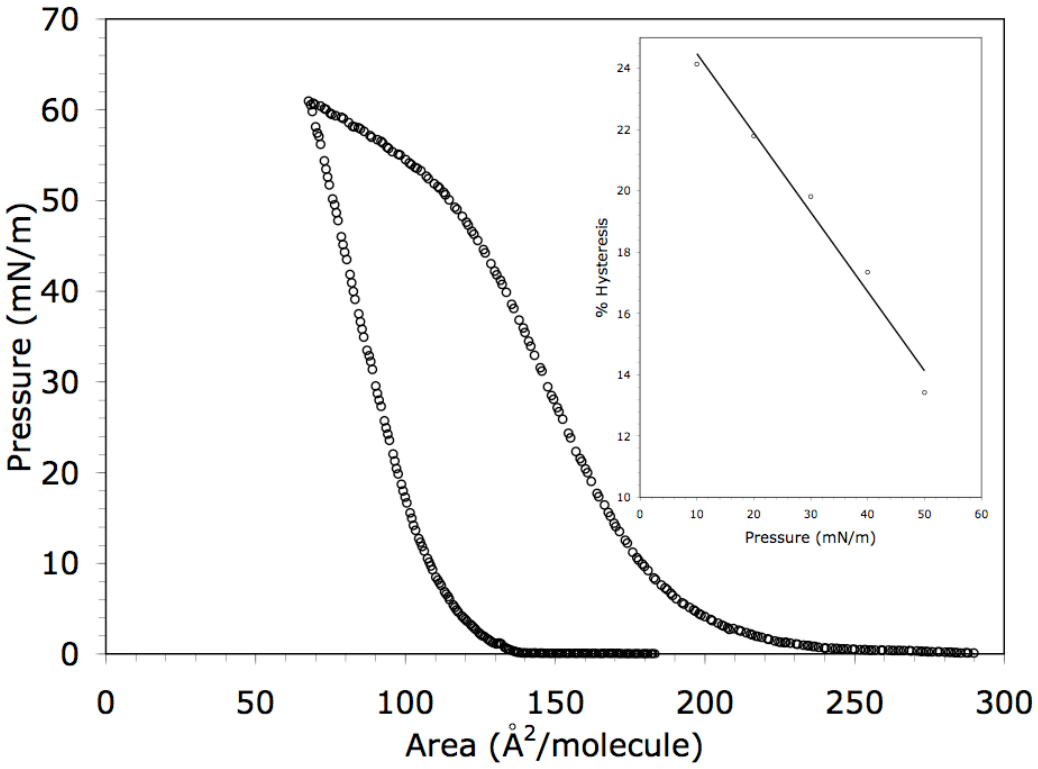

Figure 4.2: Beta 3 compression and expansion cycle performed using a barrier speed of 0.1mm/min at 25° C. The inset is the % hysteresis as a function of surface pressure.

A third possibility is hysteresis due to the formation of supramolecular structures at the interface. Similar hysteresis has been previously observed in other molecules that

have hydrogen bonding capabilities[113, 137]. In earlier work with these molecules, we determined that upon compression a β-sheet is formed at the air/water interface[134]. Thus, we believe that the hysteresis observed in our experiments bares a resemblance to that observed in other hydrogen-bonded networks. Du *et al.* make it a point to note that the hysteresis increases as the monolayer is compressed to higher pressures indicating that the molecules in the condensed phase aggregate tightly. The hysteresis also increases with compression to higher pressures with our molecules as can be seen in figure 4.1.

Figure 4.1 also contains Brewster angle microscopy images obtained during the isocycling experiment. As can be seen in the figure, supramolecular structures are being formed at the air/water interface. In previous work, we discuss how the molecules first form circular domain that subsequently transition to stripe (or fibrous) phases at higher surface concentrations[134]. During the first compression, images are obtained at 3.8 mN/m and show small circular structures during compression and an increased number of structures during expansion. The increase in the number of structures could be attributed to the fact that the isocycle went to about 5mN/m (311 $Å^2$/molecule) before it expanded. Therefore, if the molecular aggregates were tightly bound, then they would not disassemble immediately. Subsequently, a rapid decrease in surface pressure occurs upon expansion resulting in the observation of more molecular aggregates during expansion than compression at the same surface pressure. A similar effect is seen in the images obtained during the second isocycle at 35 mN/m. During the third isocycle images are taken at 55mN/m and show fibrous aggregates in both compression and expansion.

We have also performed cycles of compressions and expansions where each cycle is compressed to the same area. Figure 4.3 shows that each subsequent compression curve shifts to the left. As the cycles progress, less hysteresis is observed. However, the hysteresis persists after repeated cycling. After cycle 5, the hysteresis between compression and expansion still exists but the curves have stopped shifting to the left (data not shown). We are certain that the main cause of hysteresis is not due to loss of material to the subphase from performing Brewster angle microscopy experiments. The data confirming this is shown in figure 4.4 through histograms of images taken during the first four cycles. The overall intensity remains fairly constant with a slight shift towards higher pixel values upon each cycle. Since Brewster angle microscopy measures differences in indices of refraction, this slight shift in intensity indicates more peptide material at the interface or an increased number of aggregates upon each cycle, which would not explain the hysteresis behavior.

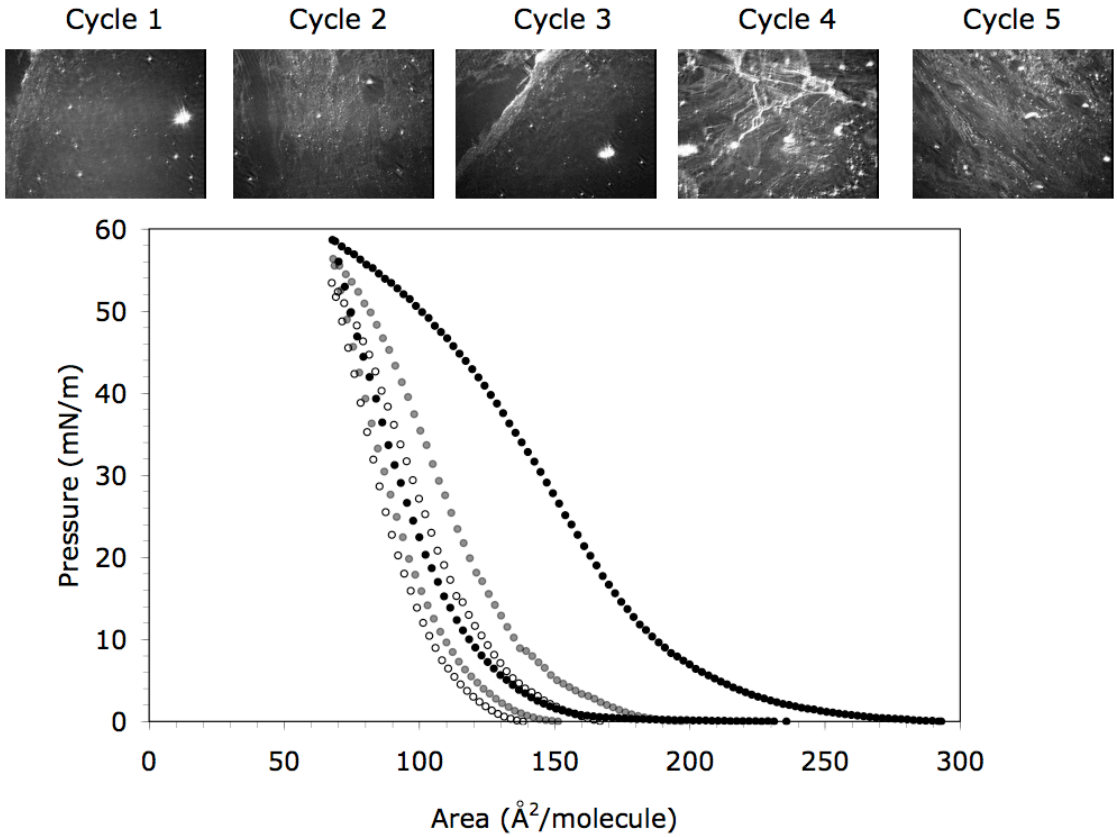

Figure 4.3: Compression and Expansion cycles of the Beta 3 molecule at 25ºC. The black filled circles are the 1st Cycle, the gray circles are the 3rd cycle, and the light gray circles are the 5th cycle. The Brewster angle microscope images above the isotherm are all taken at 45 mN/m for the first five cycles. The width of the each image is 220 μm.

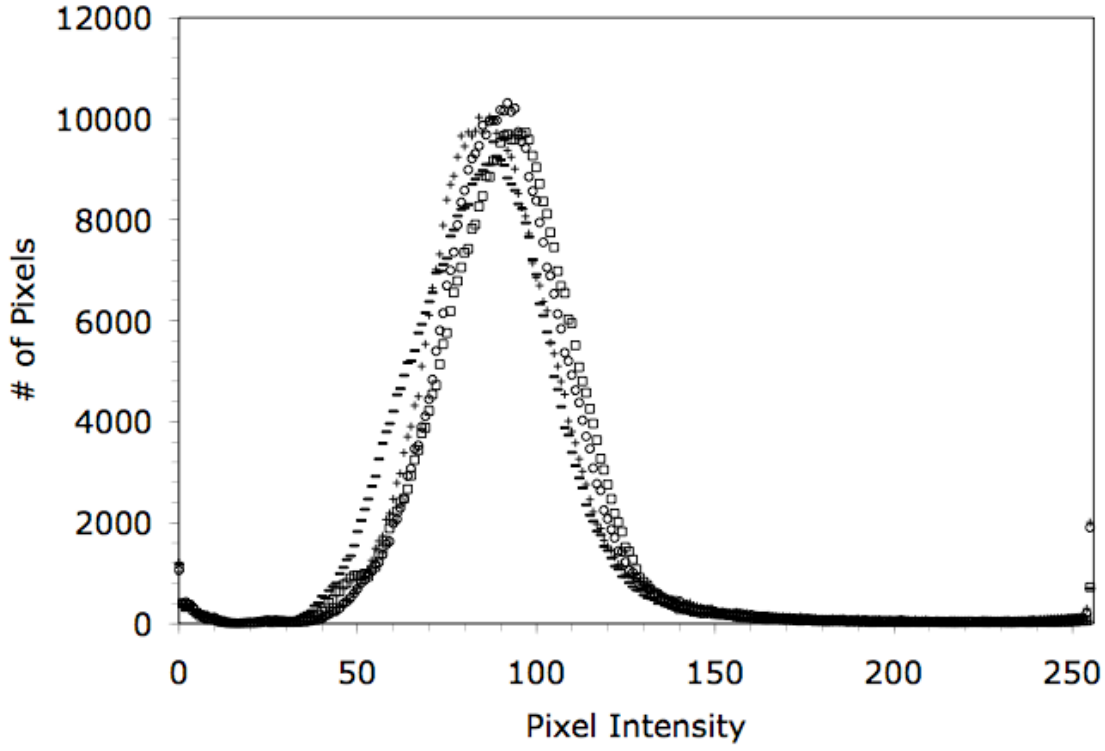

Figure 4.4: Histogram for images taken at 20mN/m for the first 4 cycles of compression/expansion experiments performed in Figure 4.3. Cycle 1: dash, Cycle 2: plus sign, Cycle 3: Open circle, Cycle 4: open square. The data shows that material is not being lost to the interface since the overall intensity of the images shifts slightly toward higher pixel values upon each cycle indicating greater amount of peptide at the interface or the increased presence of aggregates.

Instead we believe that the strong aggregation of the peptide molecules caused by the hydrogen bonded β-sheet network is the cause of the hysteresis. Studies by Sjorgen on peptide helices have also observed large amounts of hysteresis between the compression and expansion of their molecules. Their peptides are composed of strictly poly-L-leucine and self-assemble into domains at the air/water interface driven by hydrophobic interactions or when at neutral pH and the molecule is zwitterionic through electrostatic interactions between the oppositely charged end groups[138]. By studying the effects of pH, they concluded that when the molecules were zwitterionic, domain

formation was promoted and the equilibrium concentration of free strands was suppressed. Conversely at basic pH, when the molecule was anionic, aggregation was suppressed and there was a high surface concentration of free strands. Although not shown, they visualized the domains using Brewster Angle microscopy and found that large domains (larger than the field of view) were present even at low surface pressures in both neutral and alkaline conditions leading them to conclude that at low pressures the molecules in domains were in equilibrium with free peptides[138]. The formation of such large domains in their experiments is most likely due to the large size of the polypeptide and the high hydrophobic character of poly-L-leucine. In addition, they attributed hysteresis in compression and expansion isotherms to their peptide system being far from equilibrium.[138] The data in figure 4.3 with its large amount of hysteresis between compression and expansion would fit that hypothesis for our peptide molecules even though the aggregation mechanism for our molecules is hydrogen bonding instead of electrostatic and hydrophobic interactions in the case of the poly-L-leucine helices.

Figure 4.3 also contains Brewster Angle microscopy images taken at 45mN/m during compression for the first 5 cycles. In the first image only small spherical aggregates are present, which seemingly increase in concentration until fibrous aggregates can be seen in the images for cycle 4 and 5. The increase in the number of spherical aggregates and the appearance of fully formed fibrous aggregates at lower surface pressures in cycle 4 and 5 (they are normally fully formed at 50 mN/m) indicate that upon each subsequent cycle more molecules are being forced into a tightly bound state that has not disassembled during the course of the experiment. This would also

explain why the first cycle reaches the highest surface pressure at the most compressed state compared to cycle 3 and cycle 5 as can also be seen in figure 4.3.

Lack of hysteresis in Langmuir films has often been attributed to reversibility[139-141]. These findings are in stark contrast to our own. Not only is hysteresis observed in both the cycling and isocycling experiments but also when our system is observed using Brewster angle microscopy, we can visualize both domain formation and separation. Images obtained using the Brewster angle microscope in parallel with the Langmuir trough can be seen in figure 4.5. In previous work, we discuss how the molecules first form circular domain that subsequently transition to stripe (or fibrous) phases at higher surface concentrations[134]. This transition can be seen in figure 4.5 a-c. During the decompression one can see that the fibrous domains are still visible at surface pressures where they are not present during the compression, again indicating hysteresis as seen in figure 4.5 d. After multiple compression/expansion cycles, we are able to return to a domainless interface as seen in figure 4.5 e or we can observe a fibrous domain, as seen in figure 4.5 f. Thus the correlation between persistence of self-assembled domains and irreversibility of this peptide system can be observed.

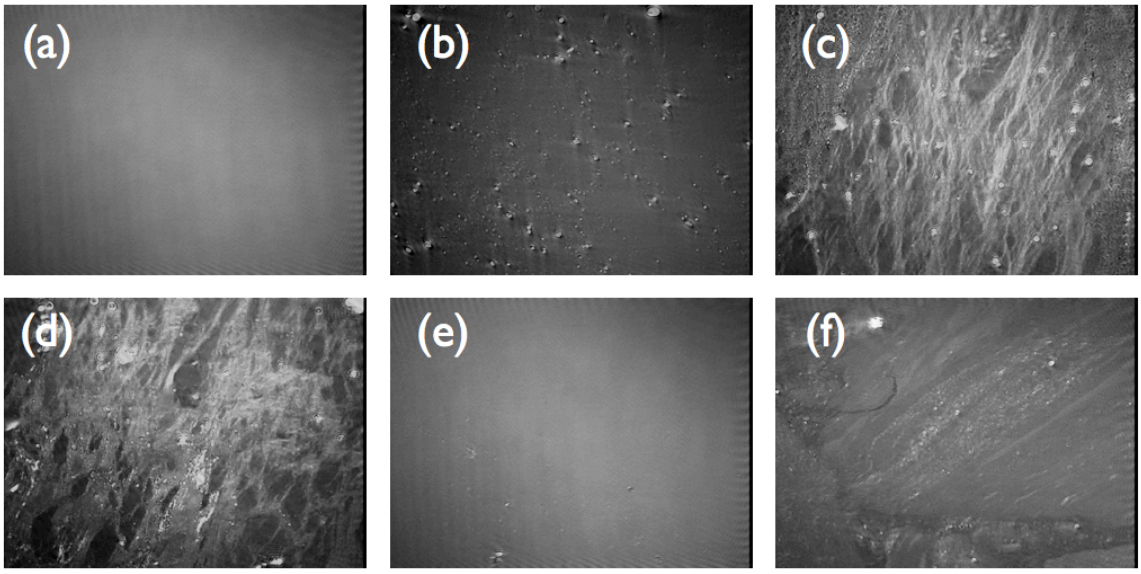

Figure 4.5: Brewster Angle Microscopy Images of Compression/Expansion Cycles. (a) During compression at surface pressure of 0.15 mN/m (b) During compression at 10 mN/m (c) During compression at 55 mN/m (d) During expansion at 42 mN/m (e) After 5 compression/expansion cycles at 0mN/m (f) After 5 compression/expansion cycles at 0.32 mN/m

To further examine the critical intermolecular interactions that govern the observed hysteresis, experiments were also performed using Beta 3H. Beta 3H has much weaker electrostatic interactions at the pH of deionized water (approximately~5.5) because of the replacement of the glutamic acid residues with histidine residues. Since electrostatic repulsion does not favor the self-assembly of these molecules, the ability of Beta 3 molecules to remain in a tightly aggregated state would be much lower than that of Beta 3H causing the Beta 3H compression/expansion data to have a greater extent of hysteresis compared to Beta 3. The data for the compression/expansion experiments of all four molecules is shown in figure 4.6. The ability of the molecule to pack tightly is not only dependent on the strength of the charge but also on the distribution of the charges. For this reason we also performed compression/expansion experiments on Beta 9, whose two negatively charged glutamic acid residues are separated by 9 residues or 4.5

nm compared to only 3 residues or 1.4 nm in Beta 3. The localized charges on Beta 3 allow the other end of the molecule to engage in hydrogen bonding with other Beta 3 molecules. In the case of Beta 9, the delocalized charge distribution would not promote hydrogen bonding on only one end of the molecule therefore when compared to Beta 3 the hysteresis observed would be less. As can be seen in the inset of figure 4.6, Beta 9 has the lowest percent hysteresis followed by Beta 3, then Beta 9H and finally Beta 3H. This data confirms that the molecules with the greatest electrostatic interactions have less ability to form tightly bound aggregates and can engage in more reversible behavior.

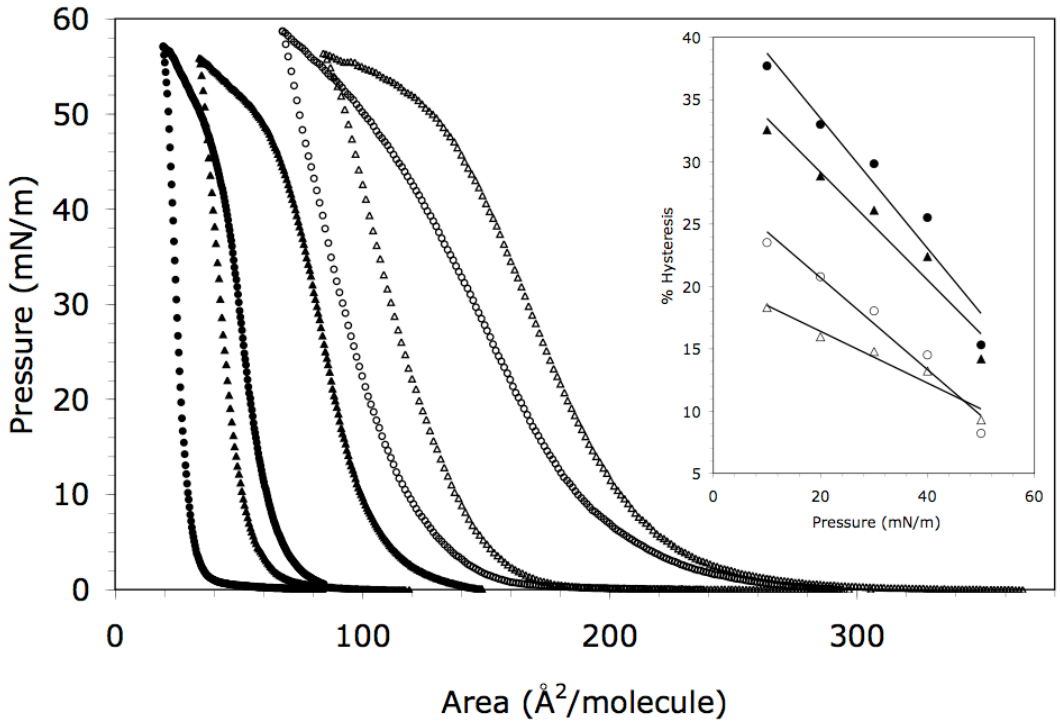

Figure 4.6: Compression/Expansion Isotherms at 25°C for Beta 3 (open circle), Beta 3H (filled circle), Beta 9 (open triangle), and Beta 9H (filled triangle). The inset shows the percent change between compression and expansion (% Hysteresis) as a function of surface pressure.

Irreversibility is a common property observed in assembled structures that are comprised predominately of β-sheets, including amyloidal aggregates, silk worm and spider silk systems. In fact a peptide fragment of the amyloid β-peptide (Aβ) attached to an aliphatic chain has been shown to demonstrate hysteresis during compression/expansion cycles similar to the hysteresis observed with our model peptides[114]. In the case of silk worm, irreversibility has been shown to be attributed to β-sheet formation by analyzing the gelation of the silk fibroin[142]. Spider silk has also been shown to be an irreversible assembly attributed to β-sheet content[130]. Both these natural materials and our model peptides have been shown to form a β-sheet network. In addition, the fibers observed during the spider silk assembly by Kenney *et al.* had visual complementarities to amyloid fibers. We believe that the fibers we observe, albeit in two dimensions in our case, also have structural similarities to those observed in amyloid and silk systems not to mention the irreversible nature and β-sheet content of the assembly. Additionally, in studying the formation of silk fibers, Jin and Kaplan observed the formation of micellar structures before the formation of the actual fiber[143]. Other studies have shown that the assembly process of the silk fibroin can be replicated using microfluidic devices and still visualize the spherical to fibrous transition[144]. These micellar structures formed in silk fibroin aggregates seem analogous to the circular domains formed before fiber formation in our systems.

4.3 Summary

In conclusion, the hysteresis observed in the surface pressure/area isotherms of our designed peptide molecules is indicative of an irreversible β-sheet assembly formed

at the air/water interface. Additionally, the domains visualized by Brewster angle microscopy confirm that this irreversibility is due to network formation at the interface. The model peptides used here designed via binary patterning seem to aggregate irreversibly by first forming a circular domain and then transitioning to fibrous domains similar to those observed in the study of silk fibroin aggregation. They also bare similarities to amyloidal and spider silk protein systems, which both form fibrous aggregates and are also irreversible. It appears that the formation of tightly bound aggregates in all these materials is attributable to β-sheet formation which is also observed in the assembly of our designed peptides. By slightly altering the design of our molecules, we show that the formation of interfacial structures can be increased by decreasing repulsive interactions that do not favor self-assembly. In addition, we show that analyzing hysteresis in the compression and expansion isotherms in combination with direct visualization using Brewster angle microscopy can capture differences in the extent of network formation elucidating the extent to which differences in electrostatic interactions influence self-assembly.

The manipulation in sequence of these rationally designed peptides has allowed us to examine how to connect macroscopic network formation with irreversible phase behavior. We believe that this interfacial phenomenon is general to natural systems where the formation of a cooperative hydrogen bonding network leads to long-ranged structural features that define the physical properties of aggregates.

Chapter 5

Interfacial templating of inorganic nanostructures using a growth directing and reducing peptide

In this chapter the interfacial templating of inorganic nanostructures is discussed. The rational design of interfacially confined peptides allows for the direct examination of biomimetic processes for materials synthesis, where non-equilibrium interfacial assembly engenders complexity in metallic nano-structures. Here we report our recent progress towards applying surface-active peptides to precisely control the spatial distribution of amino acids. In order to engineer multiple length scales in inorganic materials, our periodically sequenced peptide is trifunctional: (1) self-assembling at the air-water interface, (2) reducing gold in the subphase, and (3) directing growth of the inorganic phase under confinement. We use the Langmuir trough, Brewster angle microscopy, atomic force microscopy, transmission electron microscopy and electron diffraction to characterize control over inorganic structure as a function of the surface pressure of the organic material at the interface. Single crystalline triangular nanoplatelets of gold form at a surface pressure of 30mN/m or less. At higher surface pressures, when binding sites

are in closer proximity, a mosaic of more complex structures are formed. This work demonstrates that self-assembling surface confined peptides can be applied to define a bio-inspired tectonic process, leading to hierarchical structures at phase boundaries.

5.1 Biomimetic Approaches to Gold Nanoparticle Synthesis

Biological organisms organize inorganic materials into complex nanostructures by coupling self-assembly of the organic phase with the ability to direct growth of the inorganic phase[33, 43, 145, 146]. This mechanism has inspired engineers to develop hybrid materials at the nanometer scale, where the properties of metals and semiconductors show unique electronic, optic, and catalytic properties[24, 25]. Several methodologies have been developed to engineer functional nanoscale materials. Although, in order to precisely engineer materials with hierarchical length scales, top-down approaches are typically applied, which are limited by cost or availability of short wavelength lasers. An alternative is using bottom-up techniques to arrange atoms into nanostructures, which is limited by the complexity of structures accessible. Our work is inspired by biological composite materials where both nanoscale features and complexity are realized through non-equilibrium assembly processes[147].

Many bottom-up techniques form gold nanoparticles. Early methodologies apply citrate reductants to form simple spherical gold nanoparticles[148], but anisotropic nanoparticles such as nanorods[149, 150], nanocubes[151], triangular platelets[152], and nanostars[153] have also been observed using seed mediated approaches that use strong

reductants to produce the initial seed, increasing issues with toxicity and expense, therefore the use of biomimetic systems circumventing these issues may be an efficient pathway[7, 38]. In contrast, biomimetic templating agents have guided the assembly of particles into more complex structures such as nanochains[154] and double helices[79].

Several peptide-based approaches exist to template inorganic materials[46, 54, 155, 156]. In the case of gold, histidine-rich peptides have been applied to decorate the shell of nanotubes[66], templating a shell of isotropic gold nanoparticles along the perimeter. Also, reports exist of β-sheet forming peptides that self-assemble into fibers producing laterally spaced linear nanoparticle arrays based on the location of charged residues within the fibril[73, 74]. However, in each case inorganic nanoparticles are formed using reducing agents prior to exposure to the organic template. Recently, tryptophan has been used as a non-toxic method to synthesize spherical nanoparticles at room temperatures and anisotropic particles at higher temperatures[157]. Also, Slocik *et al.* report a one pot synthesis of spherical particles using a peptide with biomolecular recognition properties[158]. Similarly, gold nanoparticles of multiple sizes and shapes have been synthesized *in situ* using peptide amphiphile hydrogels[55] and lemongrass extract has been used to generate triangular platelets[159].

In this chapter we discuss a peptide molecule that self-assembles at the air-water interface and is capable of reducing gold ions and coordinating them to form triangular nanoplatelets and related structures. We show that we are able to control both morphology and crystallinity as a function of surface pressure. Other two-dimensional techniques that template gold at different surface pressures involve polymers[160], lipids[161], and diacetylene[162] molecules, each requiring the formation of the nanoparticles prior to

the self-assembly of the respective molecules. Therefore, our system explores a template that is capable of reducing and coordinating gold-ions from the subphase to explore the template behaviour out of equilibrium, yielding varying shapes and crystallinity by simply controlling surface pressure without using high temperatures, reducing agents, or previously formed templates.

5.2 Experimental Details

5.2.1 Crystallization Experiments

Monolayers of the peptide molecules are compressed to a given surface pressure and then 80 μL of the 0.04 M hydrogen tetrachloroaurate(III) stock solution is added to the 50mL deionized water subphase using the injection port below the air/water interface. The ions are allowed to incubate for 10 hours before samples are taken using a Langmuir-Schaefer deposition technique using carbon coated 200 mesh copper grids from Electron Microscopy Sciences (Hatfield, PA).

5.2.2 Transmission Electron Microscopy and Electron Diffraction

Samples are prepared by taking from the air-water interface using a Langmuir-Schaefer technique onto carbon-coated copper Transmission Electron Microscopy (TEM) grids. Excess solutions are removed by filter papers. These samples are then studied by TEM and electron diffraction (JOEL JEM-2100 Transmission Electron Microscope) at an acceleration voltage of 200 kV.

5.2.3 Atomic Force Microscopy

Samples for the atomic force microscope are obtained by transferring the peptide/gold monolayer using a Langmuir-Schaefer deposition technique using a silicon substrate that was previously coated with octadecyltrichlorosilane. The hydrophobic modification of the silicon substrate is achieved by using a procedure outlined previously by Kumar et al[163]. The presence of a hydrophobic layer is confirmed by measuring the contact angle, which is greater than 90°. Atomic force microscopy images are obtained using a Nanscope III instrument (Digital Instruments, Santa Barbara, CA) in tapping mode using Nanoprobe SPM (Santa Barbara, CA) tips with a resonance frequency range of 307-374 kHz and a length of 125 μm.

5.3 Results and Discussion

The two-dimensional characterization of the four peptide molecules has been discussed in chapter 3 and chapter 4. In addition to using an alternating hydrophobic and hydrophilic sequence of amino acids to achieve the periodicity associated with a β-sheet secondary structure, two other amino acids tryptophan and histidine are incorporated in this sequence. Tryptophan is included to reduce gold ions through the transfer of electrons from the amine group of tryptophan to the Au^{3+} ion[157]. Histidine is included in the sequence because of its ability to form complexes with metal ions using the imidazole and amine group of sequenced peptides[66, 164, 165]. To verify the role that histidine plays in the process of forming gold nanoparticles, we also use Beta 3 that does not contain histidine, but still contains the tryptophan residue.

In order to investigate the ability of Beta 9H to form gold nanoparticles, the peptide is deposited on the air-water interface and compressed to different surface pressures after which solutions of $HAuCl_4$ are injected into the subphase using an injection port below the interface. During the experiment, the interface is visualized using a Brewster angle microscope. The Au^{3+} ions are left to incubate in the Langmuir trough for a period of 10 hours. Brewster Angle microscopy images of the interface with the peptide at a surface pressure of 30mN/m before and after the 10-hour incubation period are shown in figure 5.1. The images show that the Beta 9H peptide forms discrete domains before the addition of gold and that the interface considerably brightens as interfacial gold structures form during the 10-hour incubation period.

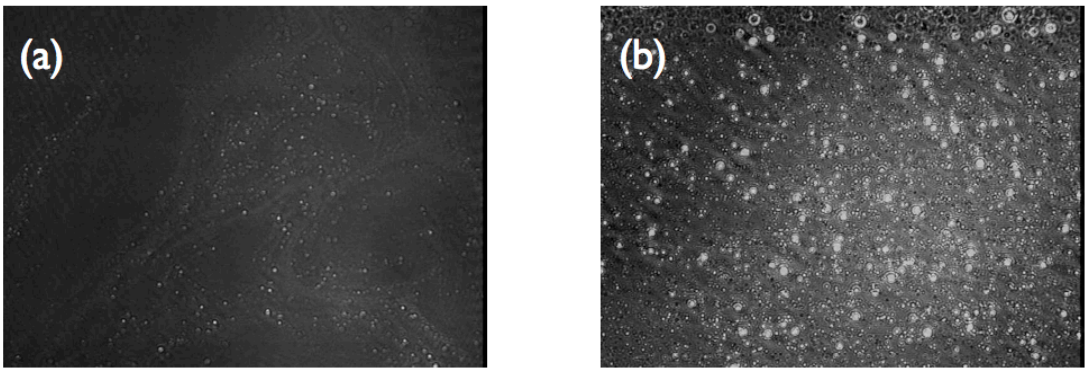

Figure 5.1: Brewster angle microscopy images taken at a surface pressure of 30mN/m (a) before incubation with Au^{3+} ions (b) after incubation with Au^{3+} ions. The width of the images is 220 μm.

Brewster angle microscopy is a measure of changes of indices of refraction at the air-water interface, and the increased brightness indicates that a material of higher refractive index has formed on the interface[123]. In order to probe the nature of these structures found on the interface after the incubation period, samples are taken from the air-water interface using a Langmuir-Schaefer technique onto carbon-coated copper

Transmission Electron Microscopy (TEM) grids. The TEM images obtained are shown in figure 5.2 with their corresponding electron diffraction patterns. The images and diffraction patterns in figure 5.2 show samples collected at 30mN/m, 40mN/m, and 50mN/m.

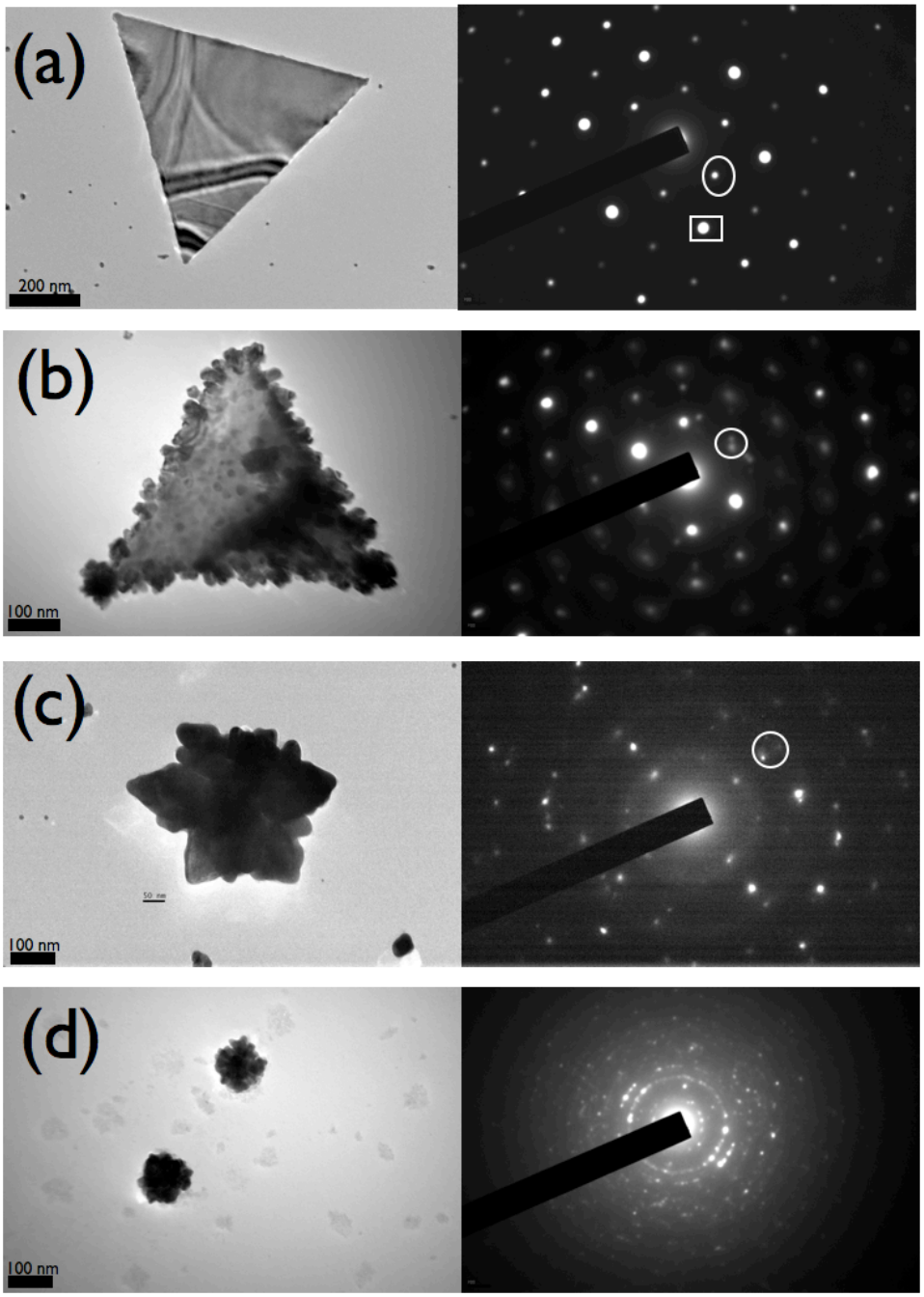

Figure 5.2: The TEM images and corresponding electron diffraction patterns at varying surface pressures: (a) Beta 9H collected at a surface pressure of 30mN/m, circled diffraction spot corresponds to 1/3 {422}; square: {220} (b) Beta 9H collected at a surface pressure of 40mN/m, circle indicates out of phase diffraction spots (c) Beta 9H collected at surface pressure of 50mN/m, circle indicates multiple out of phase diffraction spots (d) Beta 3 collected at a surface pressure of 30mN/m

The image collected at 30mN/m shows an equilateral triangle with sides of approximately 800 nm. The corresponding electron diffraction pattern indicates that the triangle is a single crystal of hexagonal symmetry and can be indexed using the fcc structure of gold. The hexagonal pattern arising in the diffraction indicates that {111} facets bound the crystal[166, 167]. The strongest peaks obtained are for the peaks pertaining to the {220} reflections as seen in figure 5.2 a.

At 40mN/m, figure 5.2 b indicates that the triangular crystal formed is rougher and smaller with sides of approximately 510 nm. The diffraction pattern still has hexagonal symmetry similar to that of the triangle formed at 30mN/m. However, the electron diffraction pattern has small differences to that shown for 30mN/m. There are often coupled diffraction peaks in the place of a single diffraction spot, suggesting that the rougher triangle is made up of multiple single crystals that are formed out of phase.

At 50mN/m, we observe through the TEM image that the structure formed is no longer a triangle, but instead a "star-like" figure that has a diameter from point to point of approximately 460 nm. Qualitatively, at these higher pressures, these "star-like" structures appear to be formed from several overlapping triangles. The electron diffraction pattern of this structure upon close examination still has the hexagonal symmetry found in the other two gold structures. However, the multiple spots effect is more pronounced indicating that the structure is more polycrystalline in nature than the rough triangle.

We have also conducted experiments at surface pressures below 30mN/m, ranging from 5mN/m to 20mN/m. In these experiments, we also observe the formation of triangular structures similar to those formed at 30mN/m in figure 5.2 a, but, at surface

pressures below 30mN/m, the yield of triangles is lower. The average number of triangles and related structures found in sample areas of the TEM grids (approximately 750 μm^2) at various surface pressures are shown in the table in figure 5.3. From the data in this table, we see a significant drop in yield when the surface pressure is below 30mN/m. We attribute the decrease in yield to be due to the lower number of peptide aggregates present between the pressures of 5-20 mN/m. Since the amount of peptide at the interface is the same at all surface pressures, we hypothesize that an aggregate of a critical size is necessary for the formation of the single crystal triangle. This phenomena also explains why at higher surface pressures, as is the case for 40mN/m and 50mN/m, the electron diffraction and TEM images indicate the presence of multiple single crystals since the peptide aggregates are much closer together at these higher surface pressures.

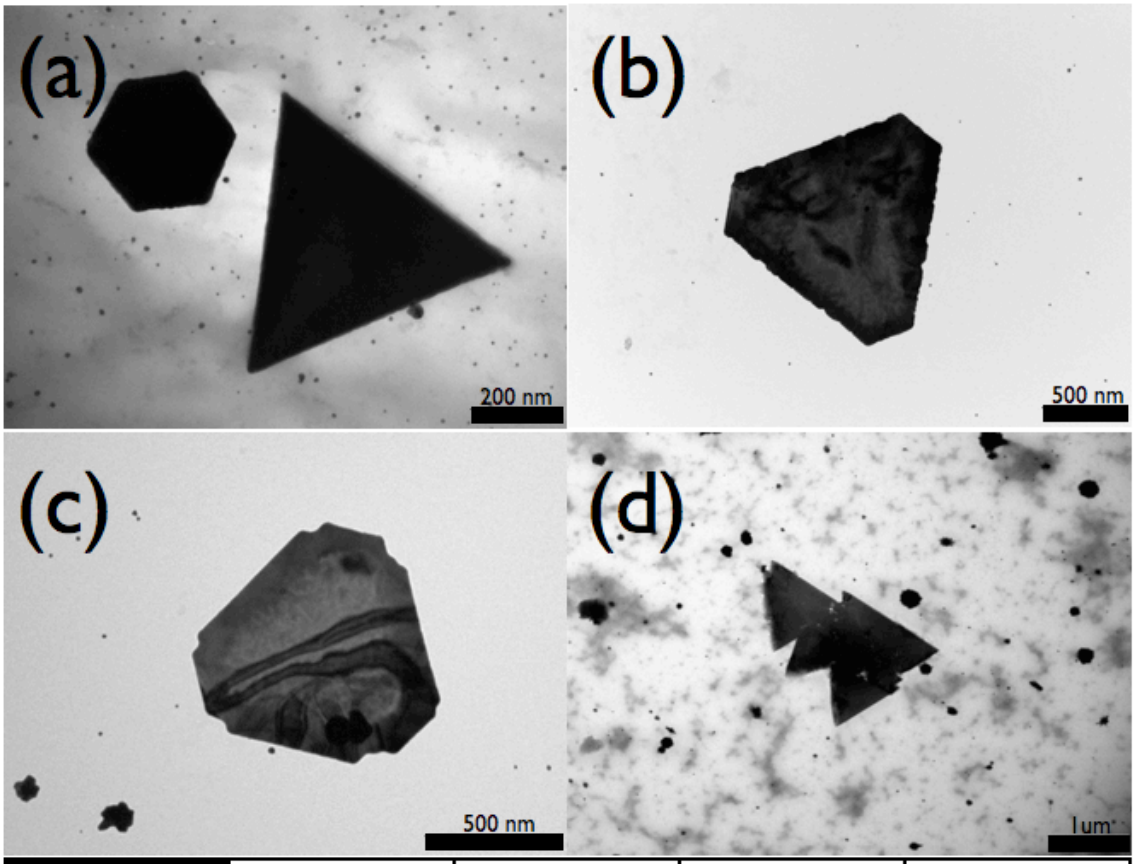

Table	5mN/m	10mN/m	20mN/m	30mN/m
Quantity (triangles or related structures in 742 μm^2 Area)	4.36±3.17	2.50±1.97	6.34±4.58	37.06±21.10
Average Area (μm^2)	0.41±0.37	0.63±0.56	0.34±0.33	0.23±0.04

Figure 5.3: TEM images of triangular nanoplatelets and related structures: (a) triangle and hexagon (b) truncated triangle (c) truncated triangle exhibiting further growth (d) saw tooth structure. Table analyzing the average size and number of triangles and related structures at surface pressures between 5-30 mN/m in sample areas of 742 μ^2

The proximity of the peptides changes between 80 $Å^2$/molecule (Π=30 mN/m) and 65 $Å^2$/molecule (Π=50 mN/m) as can be seen in figure 3.2. As the peptide film is compressed the peptides no longer have space to arrange themselves in their preferred orientation at the interface causing them to rearrange. A similar phenomenon has been observed upon compression of calcium carbonate templating molecules in which an increase in surface pressure caused the molecules to tilt[168] in one case exposing a different functional group to the interface[54]. We believe that this change in proximity of neighboring peptides causes imidazole groups in the histidine residues of the peptides to no longer always be parallel to the air/water interface leading to multiple single crystals being formed out of phase at the higher surface pressures. Numerous samples obtained from these experiments also show structures related to triangles such as hexagons, truncated triangles, and saw tooth structures. Images of these structures can be seen in figure 5.3. The hexagons and truncated triangles are found in samples obtained from surface pressures of 30mN/m and lower. The size of these structures indicates that the hexagon forms first and, subsequently, growth on three sides of the hexagon is suppressed to form a truncated triangle, and, finally, an equilateral triangle. At pressures greater than 30 mN/m, the saw tooth structure forms and appears to be a series of triangles connected along their vertices. We again hypothesize that this is a result of the proximity of peptide aggregates at higher pressures.

In order to try to understand the formation of these triangular and related structures, two additional experiments are conducted. First, Atomic Force Microscopy (AFM) is applied to determine the thickness of these structures. The AFM measurements

are shown in figure 5.4. They indicate that the truncated triangle has a thickness of approximately 20 nm. Therefore, the structures we have been observing are confirmed to be platelet structures and not pyramidal. The thinness of these structures is also confirmed using electron diffraction with tilting. In figure 5.2 a, the diffraction pattern corresponding to the triangle formed at 30mN/m shows the forbidden 1/3 {422} reflection. This reflection is only seen in platelet structures in which the surface of the gold is flat[159, 167, 169, 170]

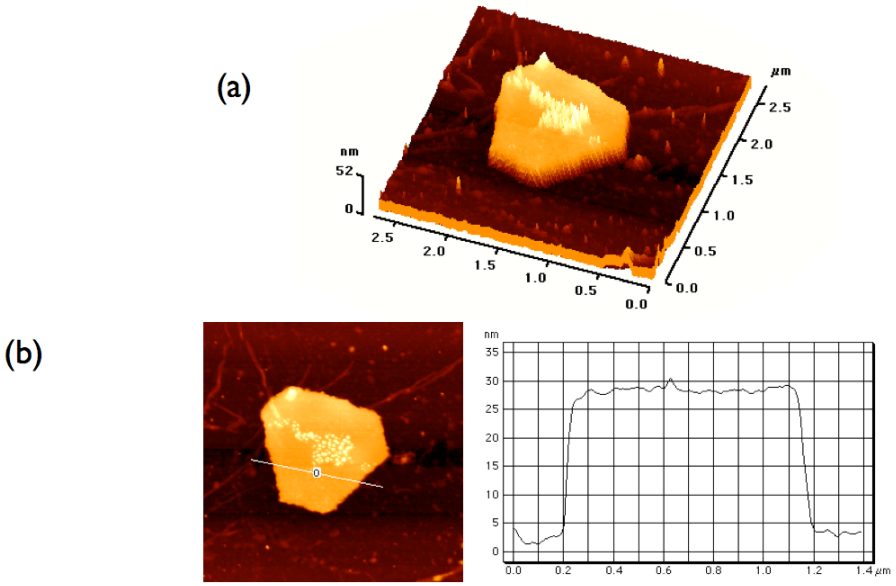

Figure 5.4: AFM images obtained for a truncated triangle at a surface pressure of 30mN/m (a) Three dimensional image (b) cross section and corresponding thickness profile

Second, a control experiment is conducted at 30mN/m using the Beta 3 peptide that contains no histidine. The TEM images and diffraction patterns for these experiments are shown in figure 5.2 d. Clearly, gold was reduced at the interface. However, the formation of triangular platelets and related structures did not occur.

Instead, we observe circular particles with diameters of approximately 100 nm and no preferential growth of any particular plane of gold. This control experiment clearly indicates that the reduction of gold in our system is attributed to the tryptophan residue in both sequences, but that the histidine residue is responsible for providing a directionality of growth and the formation of triangular platelets with the {111} face parallel to the air/water interface. Many metals have surfaces dominated by the {111} facet, indicating a low energy plane[44]. We suggest that the mechanism of growth of these triangular particles relies on the imidazole side chain binding to the {111} face of gold and thus inhibiting the growth of that particular plane or, in other words, acting as a capping agent. These fast growing facets will eventually disappear during growth, resulting in a crystal dominated by the slow growing facets[171]. This phenomena of imidazole capping the {111} facet has been observed previously in other imidazole containing molecules such as ionic liquids[169] and C18-imidazole surfactants[172]. In the case of the ionic liquid study, higher concentrations produce plate-like particles similar to those observed at our interfaces, while low concentrations produce polyhedron like particles. This indicated that at lower concentrations, the amount of imidazole containing molecules is not sufficient to inhibit growth of other crystal planes[169].

5.4 Summary

We have demonstrated that the rationally designed peptide Beta 9H can form atomically smooth single crystal triangular gold nanoplatelets optimally at a surface pressure of 30mN/m without the use of extra reducing agents or high temperatures. The rational design has incorporated a tryptophan residue that is responsible for the reduction

of Au^{3+} to Au^{0} and histidine residues that inhibit the growth of the {111} facet of gold. In addition, we have shown that by increasing the surface pressure of the Beta 9H peptide film, we promote more complex structures as a function of surface pressure, resulting in a mosaic of structures such as rough triangular platelets, saw tooth structures, and "star-like" structures that, in contrast to low surface pressure structures, are polycrystalline.

The characterization of crystallization using rationally designed peptides confined to interfaces has allowed us to access biomimetic pathways that lead to complexity in metallic nanostructure. These biologically inspired materials synthesis processes illustrate the relationship between a dynamic supramolecular template and the final crystalline product. The formation of single crystalline triangular platelets at low surface pressures and polycrystalline multi-faceted structures at higher pressures suggests a mechanism for growth of the crystalline phase that is more complex than direct epitaxy. Each surface pressure results in a unique set of growth conditions for the final inorganic structure, indicating that the phase behavior of the peptide and the dynamics of self-assembly play a critical role in determining the final structure of the composite material.

Chapter 6

Conclusions and Future Work

In this thesis, we have evaluated the self-assembly and templating ability of four rationally designed peptide molecules. These peptides have served as a model system to explore fundamental concepts of self-assembly and templating of inorganic material because peptide design allows one to make iterative changes in sequence to probe molecular interactions. This was discussed largely in chapter 3, where the iterative changes made to the peptide sequences allowed us to explore not only differences in the overall charge of the molecules, but also the effect of charge distribution, concluding that molecules that have more localized charges can pack more efficiently. We also showed that the phase behavior that the molecules exhibited under confinement transitioned from circular domains with short-range order to fibrous aggregates with long-range order and would therefore provide an ideal interface to probe different nucleation conditions during composite materials processing. This chapter also focused on the combination of interfacial techniques (surface film balances, Brewster angle microscopy, ATR-FTIR, and Circular Dichroism) with thermodynamic models to be able to quantify the influence of electrostatics on self-assembly. This allowed us to quantify the strength of

electrostatic interactions between the sequences as well as understand the transition to fibrous aggregates when hydrogen bonding dominated the free energy of the system. This combination of these techniques and analyses could be applied to other two-dimensional systems in order to understand what is driving the self-assembly or contributing to the phase behavior.

This model system also allowed us to investigate the irreversibility associated with the formation of β-sheet networks. This was discussed in chapter 4 where the persistence of structure over several compression and expansion isotherms could be visualized with Brewster angle microscopy, allowing us to correlate the extent of hysteresis with the extent of network formation. Using these model peptides has allowed us to examine how to connect macroscopic network formation with irreversible phase behavior. In addition, the similarities between the irreversible nature of our molecules and some natural systems leads us to believe that the formation of a hydrogen bonding network leads to long-ranged structural features that define the physical properties of the aggregate.

We have also shown that the rational design of peptide molecules enables the incorporation of several features into one surface active molecule. Our amphiphilic peptides are modified to include both reducing capabilities and crystal directing sequences. This was discussed in chapter 5, where we determined that the tryptophan residue was responsible for the gold reduction, and the histidine was responsible for the growth direction. The surface activity of the molecule was evaluated in chapter 3. In addition, we investigated the effect that the different phase behaviors of the peptide would have on the templating of gold. We showed that at moderate surface pressure,

when the peptide is forming circular aggregates, the addition of gold precursor to the system forms atomically smooth single crystal triangular gold nanoplatelets. We also showed that at higher pressures, the interface templates more complex polycrystalline structures. The fact that different nanostructures were templated as a function of surface pressure allowed us to draw the conclusion that the mechanism directing the formation of this composite material was more complex than direct epitaxy and depended on both the phase behavior of the peptide and the dynamics of self-assembly.

In summary, the use of rationally designed peptide molecules has allowed us to investigate fundamental concepts of both self-assembly and templating due to the modular nature of peptide molecules. The results presented here already illustrate the relationship between a dynamic supramolecular template and the resultant crystalline material. However, there are many future directions that this type of research can take that will be discussed in the following paragraphs.

One logical future direction would be to extend the characterization of the self-assembly of sheet forming peptides by manipulating hydrophobic interactions and hydrogen bonding interactions. This could be performed by designing molecules of various lengths to determine how the incorporation of more hydrophobic residues would influence the self-assembly systematically using the analysis described in chapter 3. In addition, proline residues could systematically be added to the sequences since they impede the formation of hydrogen bonds, in order to probe and quantify the influence of hydrogen bonding on self-assembly.

Another future direction could be to more carefully characterize the templating of gold by examining the reduction capabilities of the peptide. This could be performed by

using protein film voltammetry, a technique in which a protein film is attached to an electrode and the current, voltage, and frequency responses can be measured[173]. This would allow a quantification of the reduction potential of the peptide, which could in turn be manipulated and affect the templating behavior of the molecule. For example, the relationship between faster reduction and templating could be explored to verify if the molecules could still form triangular platelets. The rates of the process could be explored by increasing the rate of reduction and evaluating the consequences on the shape and connectivity of the resulting structures.

Another avenue that could be explored is the interaction of the peptides with the {111} face of gold using scanning probe microscopy techniques like those discussed in section 2.5.2. This would allow the determination of what specifically is causing the peptide to direct the growth of the gold at the molecular level: altering the kink or step density, changing the kinetic barriers associated with moving ions between the solution and the solid, pinning or blocking step motion, or chelating solution ions by reducing supersaturation. A potential pitfall in these proposed experiments is that all of the scanning probe microscopy experiments that measure the kinetics of the growth of particular steps have been performed using molecules that can be placed in solution and are not confined to interfaces. Therefore, the peptide sequence would need to be modified to include more hydrophilic residues (that are also inert to the gold surface) so that the interface between the active part of the molecule and {111} face of gold could be probed.

Another interesting direction that could be taken is to investigate the potential of the peptides to not only create discrete hybrid objects but also assemble the objects into higher order complexes. This could be achieved in several ways. One way could be to

perform the crystallization experiments at higher pH values in which the histidine residues would have a greater positive charge. This could allow the circular domains templating the gold nanocrystals to organize more periodically to minimize the charge repulsion and perhaps create regularly spaced arrays of the triangular nanoplatelets. Another approach to forming assemblies instead of discrete hybrid objects could be to manipulate the circular to fibrous transition exhibited by the peptides. Performing the crystallization experiment at the cusp of the circular to fibrous transition could induce the transition creating arrays of triangles connected by the peptide fibers. The logic behind this approach is that the interaction of the gold with the peptide molecules could lower the free energy barrier associated with the transition to the fibrous state and therefore cause the shift. There has been one instance in which we have witnessed gold triangles assembled in lines that could have been caused by this phenomenon. An image of this is shown in figure 6.1.

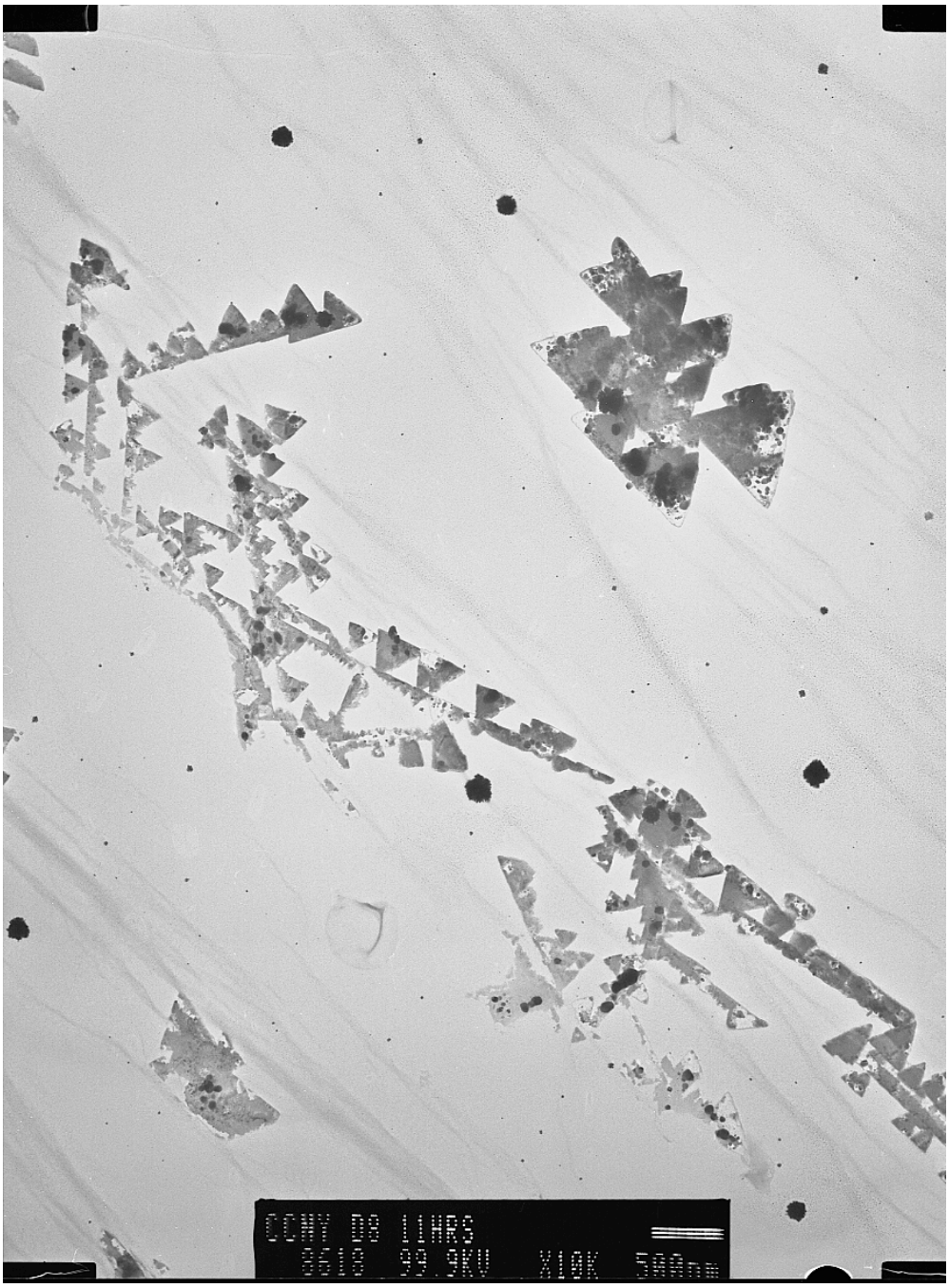

Figure 6.1: Triangular platelets that appear to be interconnected by fibers.

One obvious direction that this research could take would be to explore the templating of different materials. A good preliminary starting point would be to investigate the ability of the peptides to template silver because both glutamic acid and

histidine residues are involved in the templating of silver nanoparticles[174]. In addition, other metallic materials could be explored because of the coordination activity of histidine that was previously discussed. Moreover, to investigate the templating of other materials, the designs of the peptides could be modified to include natural or non-natural amino acids more prone to interaction with the inorganic phase.

Bibliography

1. Gao, X.; Matsui, H., Peptide-based nanotubes and their applications in bionanotechnology. *Advanced Materials* **2005,** *17* (17), 2037-2050.

2. Balazs, A.; Emrick, T.; Russell, T., Nanoparticle polymer composites: where two small worlds meet. *Science* **2006,** *314* (5802), 1107-1110.

3. Nam, K.; Kim, D.; Yoo, P.; Chiang, C.; Meethong, N.; Hammond, P.; Chiang, Y.; Belcher, A., Virus-enabled synthesis and assembly of nanowires for lithium ion battery electrodes. *Science* **2006,** *312* (5775), 885-888.

4. Murphy, C.; Gole, A.; Stone, J.; Sisco, P.; Alkilany, A.; Goldsmith, E.; Baxter, S., Gold nanoparticles in biology: beyond toxicity to cellular imaging. *Accounts of chemical research* **2008,** *41* (12), 1721-1730.

5. Jamieson, T.; Bakhshi, R.; Petrova, D.; Pocock, R.; Imani, M.; Seifalian, A., Biological applications of quantum dots. *Biomaterials* **2007,** *28* (31), 4717-4732.

6. Jain, P.; El-Sayed, I.; El-Sayed, M., Au nanoparticles target cancer. *Nano Today* **2007,** *2* (1), 18-29.

7. Rosi, N.; Mirkin, C., Nanostructures in biodiagnostics. *Chem. Rev* **2005,** *105* (4), 1547-1562.

8. Alivisatos, P., The use of nanocrystals in biological detection. *Nat Biotechnol* **2003,** *22* (1), 47-52.

9. Woodbury, R.; Wendin, C.; Clendenning, J.; Melendez, J.; Elkind, J.; Bartholomew, D.; Brown, S.; Furlong, C., Construction of biosensors using a gold-

binding polypeptide and a miniature integrated surface plasmon resonance sensor. *Biosensors and Bioelectronics* **1998,** *13* (10), 1117-1126.

10. Luckarift, H.; Greenwald, R.; Bergin, M.; Spain, J.; Johnson, G., Biosensor system for continuous monitoring of organophosphate aerosols. *Biosensors and Bioelectronics* **2007,** *23* (3), 400-406.

11. Riboh, J.; Haes, A.; McFarland, A.; Yonzon, C.; Van Duyne, R., A nanoscale optical biosensor: real-time immunoassay in physiological buffer enabled by improved nanoparticle adhesion. *J. Phys. Chem. B* **2003,** *107* (8), 1772-1780.

12. Haes, A.; Van Duyne, R., A nanoscale optical biosensor: sensitivity and selectivity of an approach based on the localized surface plasmon resonance spectroscopy of triangular silver nanoparticles. *J. Am. Chem. Soc* **2002,** *124* (35), 10596-10604.

13. Willets, K.; Van Duyne, R., Localized surface plasmon resonance spectroscopy and sensing. *Physical Chemistry* **2007,** *58* (1), 267-297.

14. Yemini, M.; Reches, M.; Rishpon, J.; Gazit, E., Novel electrochemical biosensing platform using self-assembled peptide nanotubes. *Nano Lett* **2005,** *5* (1), 183-186.

15. Wong, M.; Cha, J.; Choi, K.; Deming, T.; Stucky, G., Assembly of nanoparticles into hollow spheres using block copolypeptides. *Nano Letters* **2002,** *2* (6), 583-587.

16. Shiomi, T.; Tsunoda, T.; Kawai, A.; Mizukami, F.; Sakaguchi, K., Biomimetic Synthesis of Lysozyme− Silica Hybrid Hollow Particles Using Sonochemical Treatment: Influence of pH and Lysozyme Concentration on Morphology. *Chem. Mater* **2007,** *19* (18), 4486-4493.

17. Euliss, L.; Grancharov, S.; O'Brien, S.; Deming, T.; Stucky, G.; Murray, C.; Held, G., Cooperative assembly of magnetic nanoparticles and block copolypeptides in aqueous media. *Nano Letters* **2003,** *3* (11), 1489-1493.

18. Djalali, R.; Samson, J.; Matsui, H., Doughnut-shaped peptide nano-assemblies and their applications as nanoreactors. *J. Am. Chem. Soc* **2004,** *126* (25), 7935-7939.

19. McMillan, R.; Howard, J.; Zaluzec, N.; Kagawa, H.; Mogul, R.; Li, Y.; Paavola, C.; Trent, J., A self-assembling protein template for constrained synthesis and patterning of nanoparticle arrays. *J. Am. Chem. Soc* **2005,** *127* (9), 2800-2801.

20. Hoinville, J.; Bewick, A.; Gleeson, D.; Jones, R.; Kasyutich, O.; Mayes, E.; Nartowski, A.; Warne, B.; Wiggins, J.; Wong, K., High density magnetic recording on protein-derived nanoparticles. *Journal of Applied Physics* **2003,** *93* (10), 7187-7189.

21. Hyeon, T., Chemical synthesis of magnetic nanoparticles. *Chemical communications* **2002,** (8), 927-934.

22. Luckarift, H.; Spain, J.; Naik, R.; Stone, M., Enzyme immobilization in a biomimetic silica support. *Nat Biotechnol* **2004,** *22* (2), 211-213.

23. Luckarift, H.; Balasubramanian, S.; Paliwal, S.; Johnson, G.; Simonian, A., Enzyme-encapsulated silica monolayers for rapid functionalization of a gold surface. *Colloids and Surfaces B: Biointerfaces* **2007,** *58* (1), 28-33.

24. Eustis, S.; El-Sayed, M., Why gold nanoparticles are more precious than pretty gold: Noble metal surface plasmon resonance and its enhancement of the radiative and nonradiative properties of nanocrystals of different shapes. *Chem. Soc. Rev.* **2006,** *35* (3), 209-217.

25. Katz, E.; Willner, I., Integrated nanoparticle-biomolecule hybrid systems: synthesis, properties, and applications. *Angew. Chem. Int. Ed.* **2004,** *43* (45), 6042-6108.

26. Chen, C.; Rosi, N., Peptide-Based Methods for the Preparation of Nanostructured Inorganic Materials. *Angew. Chem. Int. Ed.* **2010,** *49* (11), 1924-1942.

27. Yu, L.; Banerjee, I.; Shima, M.; Rajan, K.; Matsui, H., Size-Controlled Ni Nanocrystal Growth on Peptide Nanotubes and Their Magnetic Properties. *Advanced Materials* **2004,** *16* (8), 709-712.

28. Ma, P., Biomimetic materials for tissue engineering. *Advanced Drug Delivery Reviews* **2008,** *60* (2), 184-198.

29. Toksöz, S.; Guler, M., Self-assembled peptidic nanostructures. *Nano Today* **2009,** *4* (6), 458-469.

30. Langer, R.; Tirrell, D., Designing materials for biology and medicine. *Nature* **2004,** *428* (6982), 487-492.

31. Tu, R., Bottom-up design of biomimetic assemblies. *Advanced Drug Delivery Reviews* **2004,** *56* (11), 1537-1563.

32. Mann, S., Self-assembly and transformation of hybrid nano-objects and nanostructures under equilibrium and non-equilibrium conditions. *Nature Materials* **2009,** *8* (10), 781-792.

33. Bäuerlein, E., Biomineralization of unicellular organisms: an unusual membrane biochemistry for the production of inorganic nano-and microstructures. *Angew. Chem. Int. Ed.* **2003,** *42* (6), 614-641.

34. Faivre, D.; Schüler, D., Magnetotactic bacteria and magnetosomes. *Chemical Reviews* **2008,** *108* (11), 4875-4898.

35. Carney, C.; Harry, S.; Sewell, S.; Wright, D., Detoxification biominerals. *Top Curr Chem* **2007,** *270*, 155-185.

36. Mukherjee, P.; Ahmad, A.; Mandal, D.; Senapati, S.; Sainkar, S.; Khan, M.; Ramani, R.; Parischa, R.; Ajayakumar, P.; Alam, M., Bioreduction of AuCl4− ions by the fungus, Verticillium sp. and surface trapping of the gold nanoparticles formed. *Angew. Chem. Int. Ed.* **2001,** *40* (19), 3585-3588.

37. Young, J.; Davis, S.; Bown, P.; Mann, S., Coccolith Ultrastructure and Biomineralisation. *Journal of Structural Biology* **1999,** *126* (3), 195-215.

38. Dickerson, M.; Sandhage, K.; Naik, R., Protein-and peptide-directed syntheses of inorganic materials. *Chemical Reviews* **2008,** *108* (11), 4935-4978.

39. Sumper, M.; Kröger, N., Silica formation in diatoms: the function of long-chain polyamines and silaffins. *J. Mater. Chem.* **2004,** *14* (14), 2059-2065.

40. Kröger, N.; Deutzmann, R.; Sumper, M., Polycationic peptides from diatom biosilica that direct silica nanosphere formation. *Science* **1999,** *286* (5442), 1129.

41. Murugan, R.; Ramakrishna, S., Development of nanocomposites for bone grafting. *Composites Science and Technology* **2005,** *65* (15-16), 2385-2406.

42. Fratzl, P.; Weinkamer, R., Nature's hierarchical materials. *Progress in Materials Science* **2007,** *52* (8), 1263-1334.

43. Weiner, S.; Wagner, H., The Material Bone: Structure-Mechanical Function Relations. *Annual Reviews in Materials Science* **1998,** *28* (1), 271-298.

44. Kramer, R.; Li, C.; Carter, D.; Stone, M.; Naik, R., Engineered protein cages for nanomaterial synthesis. *J. Am. Chem. Soc* **2004,** *126* (41), 13282-13286.

45. Butts, C.; Swift, J.; Kang, S.; Di Costanzo, L.; Christianson, D.; Saven, J.; Dmochowski, I., Directing Noble Metal Ion Chemistry within a Designed Ferritin Protein†,‡. *Biochemistry* **2008,** *47* (48), 12729-12739.

46. Tomczak, M.; Glawe, D.; Drummy, L.; Lawrence, C.; Stone, M.; Perry, C.; Pochan, D.; Deming, T.; Naik, R., Polypeptide-templated synthesis of hexagonal silica platelets. *J. Am. Chem. Soc* **2005,** *127* (36), 12577-12582.

47. Wong Po Foo, C.; Patwardhan, S.; Belton, D.; Kitchel, B.; Anastasiades, D.; Huang, J.; Naik, R.; Perry, C.; Kaplan, D., Novel nanocomposites from spider silk–silica fusion (chimeric) proteins. *Proceedings of the National Academy of Sciences* **2006,** *103* (25), 9428.

48. Huang, J.; Wong, C.; George, A.; Kaplan, D., The effect of genetically engineered spider silk-dentin matrix protein 1 chimeric protein on hydroxyapatite nucleation. *Biomaterials* **2007,** *28* (14), 2358-2367.

49. Yuwono, V.; Hartgerink, J., Peptide amphiphile nanofibers template and catalyze silica nanotube formation. *Langmuir* **2007,** *23* (9), 5033-5038.

50. Meegan, J.; Aggeli, A.; Boden, N.; Brydson, R.; Brown, A.; Carrick, L.; Brough, A.; Hussain, A.; Ansell, R., Designed Self−Assembled β−Sheet Peptide Fibrils as Templates for Silica Nanotubes. *Advanced Functional Materials* **2004,** *14* (1), 31-37.

51. Altunbas, A.; Sharma, N.; Lamm, M. S.; Yan, C.; Nagarkar, R. P.; Schneider, J. P.; Pochan, D. J., Peptide− Silica Hybrid Networks: Biomimetic Control of Network Mechanical Behavior. *ACS nano* **2009,** *4* (1), 181-188.

52. Holmström, S.; King, P.; Ryadnov, M.; Butler, M.; Mann, S.; Woolfson, D., Templating Silica Nanostructures on Rationally Designed Self-Assembled Peptide Fibers. *Langmuir* **2008,** *24* (20), 11778-11783.

53. Hartgerink, J.; Beniash, E.; Stupp, S., Self-Assembly and Mineralization of Peptide-Amphiphile Nanofibers. *Science* **2001,** *294* (5547), 1684-1688.

54. Cavalli, S.; Popescu, D. C.; Tellers, E. E.; Vos, M. R. J.; Pichon, B. P.; Overhand, M.; Rapaport, H.; Sommerdijk, N. A. J. M.; Kros, A., Self-Organizing β-Sheet Lipopeptide Monolayers as Template for the Mineralization of CaCO3. *Angew. Chem. Int. Ed.* **2006,** *45* (5), 739-744.

55. Mitra, R.; Das, P., In situ preparation of gold nanoparticles of varying shape in molecular hydrogel of peptide amphiphiles. *The Journal of Physical Chemistry C* **2008,** *112* (22), 8159-8166.

56. DeOliveira, D. B.; Laursen, R. A., Control of calcite crystal morphology by a peptide designed to bind to a specific surface. *Journal of the American Chemical Society* **1997,** *119* (44), 10627-10631.

57. Ajikumar, P.; Vivekanandan, S.; Lakshminarayanan, R.; Jois, S.; Kini, R.; Valiyaveettil, S., Mimicking the Function of Eggshell Matrix Proteins: The Role of Multiplets of Charged Amino Acid Residues and Self-Assembly of Peptides in Biomineralization. *Angew. Chem. Int. Ed.* **2005,** *44* (34), 5476-5479.

58. Dickerson, M. B.; Jones, S. E.; Cai, Y.; Ahmad, G.; Naik, R. R.; Kröger, N.; Sandhage, K. H., Identification and design of peptides for the rapid, high-yield formation of nanoparticulate TiO2 from aqueous solutions at room temperature. *Chemistry of Materials* **2008,** *20* (4), 1578-1584.

59. Umetsu, M.; Mizuta, M.; Tsumoto, K.; Ohara, S.; Takami, S.; Watanabe, H.; Kumagai, I.; Adschiri, T., Bioassisted Room-Temperature Immobilization and Mineralization of Zinc Oxide—The Structural Ordering of ZnO Nanoparticles into a Flower-Type Morphology. *Advanced Materials* **2005,** *17* (21), 2571-2575.

60. Euliss, L.; Bartl, M.; Stucky, G., Control of calcium carbonate crystallization utilizing amphiphilic block copolypeptides. *Journal of Crystal Growth* **2006,** *286* (2), 424-430.

61. Jan, J.; Lee, S.; Carr, C.; Shantz, D., Biomimetic synthesis of inorganic nanospheres. *Chem. Mater* **2005,** *17* (17), 4310-4317.

62. Slocik, J.; Naik, R., Biologically programmed synthesis of bimetallic nanostructures. *Advanced Materials* **2006,** *18* (15), 1988-1992.

63. Sano, K.; Sasaki, H.; Shiba, K., Utilization of the pleiotropy of a peptidic aptamer to fabricate heterogeneous nanodot-containing multilayer nanostructures. *J. Am. Chem. Soc* **2006,** *128* (5), 1717-1722.

64. Dai, H.; Choe, W.; Thai, C.; Sarikaya, M.; Traxler, B.; Baneyx, F.; Schwartz, D., Nonequilibrium Synthesis and Assembly of Hybrid Inorganic− Protein Nanostructures Using an Engineered DNA Binding Protein. *J. Am. Chem. Soc* **2005,** *127* (44), 15637-15643.

65. Li, L.; Stupp, S., One-Dimensional Assembly of Lipophilic Inorganic Nanoparticles Templated by Peptide-Based Nanofibers with Binding Functionalities. *Angewandte Chemie* **2005,** *117* (12), 1867-1870.

66. Djalali, R.; Chen, Y.; Matsui, H., Au nanocrystal growth on nanotubes controlled by conformations and charges of sequenced peptide templates. *J. Am. Chem. Soc* **2003,** *125* (19), 5873-5879.

67. Banerjee, I.; Yu, L.; Matsui, H., Room-temperature wurtzite ZnS nanocrystal growth on Zn finger-like peptide nanotubes by controlling their unfolding peptide structures. *J. Am. Chem. Soc* **2005,** *127* (46), 16002-16003.

68. Yu, L.; Banerjee, I.; Matsui, H., Incorporation of sequenced peptides on nanotubes for Pt coating: smart control of nucleation and morphology via activation of metal binding sites on amino acids. *J. Mater. Chem.* **2004,** *14* (4), 739-743.

69. Banerjee, I.; Yu, L.; Matsui, H., Cu nanocrystal growth on peptide nanotubes by biomineralization: size control of Cu nanocrystals by tuning peptide conformation. *Proceedings of the National Academy of Sciences of the United States of America* **2003,** *100* (25), 14678.

70. Shenton, W.; Douglas, T.; Young, M.; Stubbs, G.; Mann, S., Inorganic-organic nanotube composites from template mineralization of tobacco mosaic virus. *Advanced Materials* **1999,** *11* (3), 253-256.

71. Dujardin, E.; Peet, C.; Stubbs, G.; Culver, J.; Mann, S., Organization of metallic nanoparticles using tobacco mosaic virus templates. *Nano Letters* **2003,** *3* (3), 413-417.

72. Slocik, J.; Naik, R.; Stone, M.; Wright, D., Viral templates for gold nanoparticle synthesis. *J. Mater. Chem.* **2005,** *15* (7), 749-753.

73. Lamm, M.; Sharma, N.; Rajagopal, K.; Beyer, F.; Schneider, J.; Pochan, D., Laterally Spaced Linear Nanoparticle Arrays Templated by Laminated β-Sheet Fibrils. *Advanced Materials* **2008,** *20* (3), 447-451.

74. Sharma, N.; Top, A.; Kiick, K.; Pochan, D., One-dimensional gold nanoparticle arrays by electrostatically directed organization using polypeptide self-assembly. *Angew. Chem. Int. Ed.* **2009,** *48* (38), 7078-7082.

75. Carter, J.; LaBean, T., Organization of Inorganic Nanomaterials via Programmable DNA Self-Assembly and Peptide Molecular Recognition. *ACS nano* **2011,** *5* (3), 2200-2205.

76. Slocik, J.; Tam, F.; Halas, N.; Naik, R., Peptide-assembled optically responsive nanoparticle complexes. *Nano Lett* **2007,** *7* (4), 1054-1058.

77. Pouget, E.; Dujardin, E.; Cavalier, A.; Moreac, A.; Valéry, C.; Marchi-Artzner, V.; Weiss, T.; Renault, A.; Paternostre, M.; Artzner, F., Hierarchical architectures by synergy between dynamical template self-assembly and biomineralization. *Nature Materials* **2007,** *6* (6), 434-439.

78. Lee, S.; Yun, D.; Belcher, A., Cobalt Ion Mediated Self-Assembly of Genetically Engineered Bacteriophage for Biomimetic Co− Pt Hybrid Material. *Biomacromolecules* **2006,** *7* (1), 14-17.

79. Chen, C.; Zhang, P.; Rosi, N., A New Peptide-Based Method for the Design and Synthesis of Nanoparticle Superstructures: Construction of Highly Ordered Gold Nanoparticle Double Helices. *J. Am. Chem. Soc* **2008,** *130* (41), 13555-13557.

80. Callister Jr, W., *Materials Science and Engineering*. 2006.

81. Wang, L.; Nancollas, G., Dynamics of Biomineralization and Biodemineralization. *Metal ions in life sciences* **2010,** *4*, 413-456.

82. Tang, R.; Darragh, M.; Orme, C.; Guan, X.; Hoyer, J.; Nancollas, G., Control of Biomineralization Dynamics by Interfacial Energies. *Angew. Chem. Int. Ed.* **2005,** *44* (24), 3698-3702.

83. Burton, W.; Cabrera, N.; Frank, F., The growth of crystals and the equilibrium structure of their surfaces. *Philosophical Transactions of the Royal Society of London. Series A, Mathematical and Physical Sciences* **1951,** *243* (866), 299-358.

84. Qiu, S.; Orme, C., Dynamics of biomineral formation at the near-molecular level. *Chemical Reviews* **2008,** *108* (11), 4784-4822.

85. Elhadj, S.; De Yoreo, J.; Hoyer, J.; Dove, P., Role of molecular charge and hydrophilicity in regulating the kinetics of crystal growth. *Proceedings of the National Academy of Sciences* **2006,** *103* (51), 19237-19242.

86. Orme, C.; Noy, A.; Wierzbicki, A.; McBride, M.; Grantham, M.; Teng, H.; Dove, P.; DeYoreo, J., Formation of chiral morphologies through selective binding of amino acids to calcite surface steps. *Nature* **2001,** *411* (6839), 775-779.

87. Weiner, S.; Traub, W., X-Ray Diffraction Study of the Insoluble Organic Matrix of Mollusk Shells. *FEBS Letters* **1980,** *111* (2), 311-316.

88. Fu, G.; Qiu, S. R.; Orme, C. A.; Morse, D. E.; De Yoreo, J. J., Acceleration of calcite kinetics by abalone nacre proteins. *Advanced Materials* **2005,** *17* (22), 2678-2683.

89. Cabrera, N.; Vermilyea, D., *The Growth of Crystal From Solution*. Chapman & Hall: London, 1958.

90. Weaver, M. L.; Qiu, S. R.; Hoyer, J. R.; Casey, W. H.; Nancollas, G. H.; De Yoreo, J. J., Improved Model for Inhibition of Pathological Mineralization Based on

Citrate–Calcium Oxalate Monohydrate Interaction. *ChemPhysChem* **2006,** *7* (10), 2081-2084.

91. Peytcheva, A.; Antonietti, M., "Carving on the Nanoscale": Polymers for the Site−Specific Dissolution of Calcium Phosphate. *Angew. Chem. Int. Ed.* **2001,** *40* (18), 3380-3383.

92. Davis, K. J.; Dove, P. M.; De Yoreo, J. J., The role of Mg2+ as an impurity in calcite growth. *Science* **2000,** *290* (5494), 1134-1137.

93. Gazit, E., Self-assembled peptide nanostructures: the design of molecular building blocks and their technological utilization. *Chem. Soc. Rev.* **2007,** *36* (8), 1263-1269.

94. Rajagopal, K.; Schneider, J., Self-assembling peptides and proteins for nanotechnological applications. *Current Opinion in Structural Biology* **2004,** *14* (4), 480-486.

95. Sarikaya, M.; Tamerler, C.; Schwartz, D.; Baneyx, F., Materials assembly and formation using engineered polypeptides. *Annual Review of Materials Research* **2004,** *34*, 373-408.

96. Zhang, S., Emerging biological materials through molecular self-assembly. *Biotechnology advances* **2002,** *20* (5-6), 321-339.

97. Bianconi, P. A.; Lin, J.; Strzelecki, A. R., Crystallization of an inorganic phase controlled by a polymer matrix. *Nature Letters* **1991,** *349*, 315-317.

98. Loste, E.; Diaz-Marti, E.; Zarbakhsh, A.; Meldrum, F., Study of calcium carbonate precipitation under a series of fatty acid Langmuir monolayers using Brewster angle microscopy. *Langmuir* **2003,** *19* (7), 2830-2837.

99. Jain, V.; Tu, R. S., Dynamic Surface Activity by Folding and Unfolding an Amphiphillic [alpha]-Helix. *Langmuir* **2008,** *24* (18), 9923-9928.

100. Weygand, M.; Kjaer, K.; Tirrell, D. A.; Rapaport, H., Parallel β-sheet assemblies at interfaces. *ChemPhysChem* **2004,** *5*, 747-750.

101. Rapaport, H.; Kjaer, K.; Jensen, T.; Leiserowitz, L.; Tirrell, D., Two-dimensional order in-sheet peptide monolayers. *J. Am. Chem. Soc* **2000,** *122* (50), 12523-12529.

102. Cavalli, S.; Handgraaf, J.; Tellers, E.; Popescu, D.; Overhand, M.; Kjaer, K.; Vaiser, V.; Sommerdijk, N.; Rapaport, H.; Kros, A., Two-Dimensional Ordered β-Sheet Lipopeptide Monolayers. *J Am Chem Soc* **2006,** *128* (42), 13959-13966.

103. Colfer, S.; Kelly, J.; Powers, E., Factors Governing the Self-Assembly of a [beta]-Hairpin Peptide at the Air− Water Interface. *Langmuir* **2003,** *19* (4), 1312-1318.

104. DeGrado, W. F.; Lear, J. D., Induction of peptide conformation at apolar/water interfaces. 1. A study with model peptides of definded hydrophobic periodicity. *Journal of the American Chemical Society* **1985,** *107* (25), 7684-7689.

105. Lopez de la Paz, M.; Goldie, K.; Zurdo, J., De novo designed peptide-based amyloid fibrils. *Proc Natl Acad Sci USA* **2002,** *99* (25), 16052-16057.

106. Jun, S., Self-Assembly of the Ionic Peptide EAK16: The Effect of Charge Distributions on Self-Assembly. *Biophysical Journal* **2004,** *87* (2), 1249-1259.

107. Mann, S.; Heywood, B.; Rajam, S.; Birchall, J., Controlled crystallization of CaCO 3 under stearic acid monolayers. *Nature* **1988,** *334* (6184), 692-695.

108. Chou, P.; Fasman, G., Prediction of protein conformation. *Biochemistry* **1974,** *13* (2), 222-245.

109. Xiong, H., Periodicity of Polar and Nonpolar Amino Acids is the Major Determinant of Secondary Structure in Self-Assembling Oligomeric Peptides. *Proceedings of the National Academy of Sciences* **1995,** *92* (14), 6349-6353.

110. Fields, G.; Noble, R., Solid phase peptide synthesis utilizing 9-fluorenylmethoxycarbonyl amino acids. *International Journal of Peptide and Protein Research* **1990,** *35* (3), 161-214.

111. Xu, A.-W.; Ma, Y.; CoLfen, H., Biomimetic mineralization. *J. Mater. Chem.* **2007,** *17* (5), 415-449.

112. Kumar, V.; Krishnan, S.; Steiner, C.; Maldarelli, C.; Couzis, A., Measurement of infrared molar absorptivity of a surfactant adsorbed onto a solid substrate over a wide range of surface concentrations using octadecyltrichlorosilane Langmuir–Blodgett transferred films. *J. Phys. Chem. B* **1998,** *102* (17), 3152–3159.

113. Reda, T.; Hermel, H.; Hoeltje, H., Compression/Expansion Hysteresis of Poly (L-glutamic acid) Monolayers Spread at the Air/Water Interface. *Langmuir* **1996,** *12* (26), 6452-6458.

114. Triulzi, R.; Li, C.; Naistat, D.; Orbulescu, J.; Leblanc, R., A Two-Dimensional Approach to Study Amyloid [beta]-Peptide Fragment (25− 35). *J. Phys. Chem. C* **2007,** *111* (12), 4661-4666.

115. Parazak, D.; Uang, J.; Turner, B.; Stine, K., Fluorescence microscopy study of chiral discrimination in Langmuir monolayers of N-acylvaline and N-acylalanine amphiphiles. *Langmuir* **1994,** *10* (10), 3787-3793.

116. Fainerman, V.; Vollhardt, D.; Melzer, V., Equation of state for insoluble monolayers of aggregating amphiphilic molecules. *J. Phys. Chem* **1996,** *100* (38), 15478-15482.

117. Fainerman, V.; Vollhardt, D., Equations of state for langmuir monolayers with two-dimensional phase transitions. *J. Phys. Chem. B* **1999,** *103* (1), 145-150.

118. Vollhardt, D.; Fainerman, V. B.; Siegel, S., Thermodynamic and textural characterization of DPPG phospholipid monolayers. *J. Phys. Chem. B* **2000,** *104* (17), 4115-4121.

119. R. Aveyard, D. A. H., *An Introduction to the Principles of Surface Chemistry*. Cambridge University Press: 1973.

120. Israelachvii, J., *Intermolecular and Surface Forces*. 2nd ed.; Academic Press Limited: 1991.

121. Hu, X.; Kaplan, D.; Cebe, P., Determining beta-sheet crystallinity in fibrous proteins by thermal analysis and infrared spectroscopy. *Macromolecules* **2006,** *39* (18), 6161-6170.

122. Johnson Jr, W., Secondary Structure of Proteins Through Circular Dichroism Spectroscopy. *Annual Reviews in Biophysics and Biophysical Chemistry* **1988,** *17* (1), 145-166.

123. Lheveder, C.; Hénon, S.; Mercier, R.; Tissot, G.; Fournet, P.; Meunier, J., A new Brewster angle microscope. *Review of Scientific Instruments* **1998,** *69* (3), 1446-1450.

124. Seul, M.; Andelman, D., Domain shapes and patterns: The phenomenology of modulated phases. *Science* **1995,** *267* (5197), 476-483.

125. McConnell, H. M., Theory of Hexagonal and Stripe Phases in Monolayers. *Proceedings of the National Academy of Sciences* **1989,** *86*, 3452-3455.

126. McConnell, H. M., Structures and Transitions in Lipid Monolayers at the Air-Water Interface. *Annual Reviews in Physical Chemistry* **1991,** *42*, 171-195.

127. McConnell, H. M.; Moy, V. T., Shapes of finite two-dimensional lipid domains. *The Journal of Physical Chemistry* **1988,** *92*, 4520-4525.

128. Kohlstedt, K.; Vernizzi, G.; Cruz, M., Surface patterning of low-dimensional systems: the chirality of charged fibres. *Journal of Physics: Condensed Matter* **2009,** *21*, 424114.

129. Lee, K.; Lipp, M.; Zasadzinski, J.; Waring, A., Effects of lung surfactant specific protein SP-B and model SP-B peptide on lipid monolayers at the air-water interface. *Colloids and Surfaces A: Physicochemical and Engineering Aspects* **1997,** *128* (1-3), 225-242.

130. Kenney, J.; Knight, D.; Wise, M., Amyloidogenic nature of spider silk. *European Journal of Biochemistry* **2002,** *269* (16), 4159-4163.

131. Willcox, P.; Gido, S.; Muller, W.; Kaplan, D., Evidence of a cholesteric liquid crystalline phase in natural silk spinning processes. *Macromolecules* **1996,** *29* (15), 5106-5110.

132. Porter, D.; Vollrath, F.; Shao, Z., Predicting the mechanical properties of spider silk as a model nanostructured polymer. *The European Physical Journal E: Soft Matter and Biological Physics* **2005,** *16* (2), 199-206.

133. Sneer, R.; Weygand, M.; Kjaer, K.; Tirrell, D. A.; Rapaport, H., Parallel β-sheet assemblies at interfaces. *ChemPhysChem* **2004,** *5* (5), 747-750.

134. Leon, L.; Logrippo, P.; Tu, R., Self-Assembly of Rationally Designed Peptides under Two-Dimensional Confinement. *Biophysical Journal* **2010,** *99* (9), 2888-2895.

135. Sharma, S.; Radhakrishnan, T. P., Phospholipid–fatty acid composite monolayers: analysis of the pressure–area isotherms. *Thin Solid Films* **2001,** (38), 246-256.

136. De Gennes, P., Coil-stretch transition of dilute flexible polymers under ultrahigh velocity gradients. *The Journal of Chemical Physics* **1974,** *60* (12), 5030-5041.

137. Du, X.; Shi, B.; Liang, Y., N-octadecanoyl-L-alanine amphiphile monolayer at the air/water interface and LB film studied by FTIR spectroscopy. *Langmuir* **1998,** *14* (13), 3631-3636.

138. Sjogren, H.; Ulvenlund, S., Effects of pH, Ionic Strength, Calcium, and Molecular Mass on the Arrangement of Hydrophobic Peptide Helices at the Air− Water Interface. *J. Phys. Chem. B* **2004,** *108* (52), 20219-20227.

139. McConlogue, C.; Vanderlick, T., A close look at domain formation in DPPC monolayers. *Langmuir* **1997,** *13* (26), 7158-7164.

140. Joncheray, T. J.; Bernard, S. A.; Matmour, R.; Lepoittevin, B., Polystyrene-b-Poly (tert-butyl acrylate) and Polystyrene-b-Poly (acrylic acid) Dendrimer-Like Copolymers: Two-Dimensional Self-Assembly at the Air− Water Interface. *Langmuir* **2007,** *23* (5), 2531-2538.

141. Cardullo, F.; Diederich, F.; Echegoyen, L.; Habicher, T.; Jayaraman, N.; Leblanc, R.; Stoddart, J.; Wang, S., Stable Langmuir and Langmuir− Blodgett Films of Fullerene− Glycodendron Conjugates. *Langmuir* **1998,** *14* (8), 1955-1959.

142. Matsumoto, A.; Chen, J.; Collette, A.; Kim, U.; Altman, G.; Cebe, P.; Kaplan, D., Mechanisms of Silk Fibroin Sol− Gel Transitions. *J. Phys. Chem. B* **2006,** *110* (43), 21630-21638.

143. Jin, H.; Kaplan, D., Mechanism of silk processing in insects and spiders. *Nature* **2003,** *424* (6952), 1057-1061.

144. Rammensee, S.; Slotta, U.; Scheibel, T.; Bausch, A. R., Assembly mechanism of recombinant spider silk proteins. *Proc Natl Acad Sci USA* **2008,** *105* (18), 6590-6595.

145. Mann, S., Molecular tectonics in biomineralization and biomimetic materials chemistry. *Nature* **1993,** *365* (6446), 499-505.

146. Zaremba, C.; Belcher, A.; Fritz, M.; Li, Y.; Mann, S.; Hansma, P.; Morse, D.; Speck, J.; Stucky, G., Critical transitions in the biofabrication of abalone shells and flat pearls. *Chem. Mater* **1996,** *8* (3), 679-690.

147. Meldrum, F.; Cölfen, H., Controlling mineral morphologies and structures in biological and synthetic systems. *Chemical Reviews* **2008,** *108* (11), 4332-4432.

148. Daniel, M.; Astruc, D., Gold nanoparticles: assembly, supramolecular chemistry, quantum-size-related properties, and applications toward biology, catalysis, and nanotechnology. *Chem. Rev* **2004,** *104* (1), 293-346.

149. Johnson, C.; Dujardin, E.; Davis, S.; Murphy, C.; Mann, S., Growth and form of gold nanorods prepared by seed-mediated, surfactant-directed synthesis. *J. Mater. Chem.* **2002,** *12* (6), 1765-1770.

150. Grzelczak, M.; Pérez-Juste, J.; Mulvaney, P.; Liz-Marzan, L., Shape control in gold nanoparticle synthesis. *Chemical Society Reviews* **2008,** *37* (9), 1783-1791.

151. Sun, Y.; Xia, Y., Shape-controlled synthesis of gold and silver nanoparticles. *Science* **2002,** *298* (5601), 2176-2179.

152. Wang, L.; Chen, X.; Zhan, J.; Chai, Y.; Yang, C.; Xu, L.; Zhuang, W.; Jing, B., Synthesis of gold nano-and microplates in hexagonal liquid crystals. *J. Phys. Chem. B* **2005,** *109* (8), 3189-3194.

153. Nehl, C.; Liao, H.; Hafner, J., Optical properties of star-shaped gold nanoparticles. *Nano Lett* **2006,** *6* (4), 683-688.

154. Polavarapu, L.; Xu, Q., A single-step synthesis of gold nanochains using an amino acid as a capping agent and characterization of their optical properties. *Nanotechnology* **2008,** *19*, 075601.

155. Yao, Y.; Dong, W.; Zhu, S.; Yu, X.; Yan, D., Novel Morphology of Calcium Carbonate Controlled by Poly(l-lysine). *Langmuir* **2009,** *25* (22), 13238-13243.

156. Reches, M.; Gazit, E., Casting metal nanowires within discrete self-assembled peptide nanotubes. *Science* **2003,** *300* (5619), 625-627.

157. Iosin, M.; Baldeck, P.; Astilean, S., Study of tryptophan assisted synthesis of gold nanoparticles by combining UV–Vis, fluorescence, and SERS spectroscopy. *Journal of Nanoparticle Research* **2010,** *12* (8), 2843-2849.

158. Slocik, J. M.; Stone, M. O.; Naik, R. R., Synthesis of gold nanoparticles using multifunctional peptides. *Small* **2005,** *1* (11), 1048-1052.

159. Shankar, S.; Rai, A.; Ankamwar, B.; Singh, A.; Ahmad, A.; Sastry, M., Biological synthesis of triangular gold nanoprisms. *Nature Materials* **2004,** *3* (7), 482-488.

160. Hansen, C.; Westerlund, F.; Moth-Poulsen, K.; Ravindranath, R.; Valiyaveettil, S.; Bjornholm, T., Polymer-templated self-assembly of a 2-dimensional gold nanoparticle network. *Langmuir* **2008,** *24* (8), 3905-3910.

161. Nørgaard, K.; Bjørnholm, T., Supramolecular chemistry on water–towards self-assembling molecular electronic circuitry. *Chemical communications* **2005,** *2005* (14), 1812-1823.

162. Markovich, N.; Volinsky, R.; Jelinek, R., Gold Nanostructures in Diacetylene Monolayer Templates. *J. Am. Chem. Soc.* **2009,** *131* (7), 2430-2431.

163. Kumar, N.; Maldarelli, C.; Steiner, C.; Couzis, A., Formation of nanometer domains of one chemical functionality in a continuous matrix of a second chemical functionality by sequential adsorption of silane self-assembled monolayers. *Langmuir* **2001,** *17* (25), 7789-7797.

164. Glisic, B.; Rajkovic, S.; Zivkovic, M.; Djuran, M., A comparative study of complex formation in the reactions of gold (III) with Gly-Gly, Gly-l-Ala and Gly-l-His dipeptides. *Bioorganic Chemistry* **2010,** *38* (4), 144-148.

165. Cuadrado, J.; Zhang, W.; Hang, W.; Majidi, V., Speciation of gold (III)–L-histidine complex: a multi-instrumental approach. *Journal of Environmental Monitoring* **2000,** *2* (4), 355-359.

166. Shao, Y.; Jin, Y.; Dong, S., Synthesis of gold nanoplates by aspartate reduction of gold chloride. *Chemical communications* **2004,** *2004* (9), 1104-1105.

167. Sun, Y.; Mayers, B.; Xia, Y., Transformation of silver nanospheres into nanobelts and triangular nanoplates through a thermal process. *Nano Letters* **2003,** *3* (5), 675-679.

168. DiMasi, E.; Kwak, S. Y.; Pichon, B. P.; Sommerdijk, N. A. J. M., Structural adaptability in an organic template for CaCO 3 mineralization. *CrystEngComm* **2007,** *9* (12), 1192-1204.

169. Zhu, J.; Shen, Y.; Xie, A.; Qiu, L.; Zhang, Q.; Zhang, S., Photoinduced synthesis of anisotropic gold nanoparticles in room-temperature ionic liquid. *J Phys Chem C* **2007,** *111*, 7629-7633.

170. Germain, V.; Li, J.; Ingert, D.; Wang, Z.; Pileni, M., Stacking faults in formation of silver nanodisks. *J. Phys. Chem. B* **2003,** *107* (34), 8717-8720.

171. Yin, Y.; Alivisatos, A., Colloidal nanocrystal synthesis and the organic–inorganic interface. *Nature* **2004,** *437* (7059), 664-670.

172. Hsu, S.; Hsu, K.; Leong, M.; Lin, I., Au (i)-benzimidazole/imidazole complexes. Liquid crystals and nanomaterials. *Dalton Transactions* **2008,** *2008* (14), 1924-1931.

173. Leger, C.; Elliott, S.; Hoke, K.; Jeuken, L.; Jones, A.; Armstrong, F., Enzyme Electrokinetics: Using Protein Film Voltammetry To Investigate Redox Enzymes and Their Mechanisms†. *Biochemistry* **2003,** *42* (29), 8653-8662.

174. Xie, J.; Lee, J.; Wang, D.; Ting, Y., Silver nanoplates: from biological to biomimetic synthesis. *ACS nano* **2007,** *1* (5), 429-439.